Posted on 15 Mar 2024 — The copyright holder is the author/funder. All rights reserved. No reuse without permission. — https://doi.org/10.22541/au.171052571.16863871/v1 — This is a preprint and has not been peer-reviewed. Data may be preliminary.

Spatiotemporal Evolution of Slow Slip Events at the Offshore Hikurangi Subduction Zone in 2019 using GNSS, InSAR, and seafloor geodetic data

Katherine Woods[1], Laura Wallace[2], Charles A. Williams[3], Ian James Hamling[3], Spahr C Webb[4], Yoshihiro Ito[5], Neville Palmer[3], Ryota Hino[6], Syuichi Suzuki[6], Martha Kane Savage[1], Emily Warren-Smith[3], and Kimihiro Mochizuki[7]

[1]Victoria University of Wellington
[2]GEOMAR & Kiel University
[3]GNS Science
[4]Lamont Doherty Earth Observatory
[5]Kyoto University
[6]Tohoku University
[7]University of Tokyo

March 15, 2024

Abstract

Detecting crustal deformation during transient deformation events at offshore subduction zones remains challenging. The spatiotemporal evolution of slow slip events (SSEs) on the offshore Hikurangi subduction zone, New Zealand, during February–July 2019, is revealed through a time-dependent inversion of onshore and offshore geodetic data that also account for spatially varying elastic crustal properties. Our model is constrained by seafloor pressure time series (as a proxy for vertical seafloor deformation), onshore continuous Global Navigation Satellite System (GNSS) data, and Interferometric Synthetic Aperture Radar (InSAR) displacements. Large GNSS displacements onshore and uplift of the seafloor (10-33 mm) require peak slip during the event of 150 to >200 mm at 6-12 km depth offshore Hawkes Bay and Gisborne, comparable to maximum slip observed during previous seafloor pressure deployments at north Hikurangi. The onshore and offshore data reveal a complex evolution of the SSE, over a period of months. Seafloor pressure data indicates the slow slip may have persisted longer near the trench than suggested by onshore GNSS stations in both the Gisborne and Hawkes Bay regions. Seafloor pressure data also reveal up-dip migration of SSE slip beneath Hawke Bay occurred over a period of a few weeks. The SSE source region appears to coincide with locations of the March 1947 Mw 7.0–7.1 tsunami earthquake offshore Gisborne and estimated Great earthquake rupture sources from paleoseismic investigations offshore Hawkes Bay, suggesting that the shallow megathrust at north and central Hikurangi is capable of both seismic and aseismic rupture.

Hosted file

`woods_modeling_paper_jgr.docx` available at https://authorea.com/users/754300/articles/724218-spatiotemporal-evolution-of-slow-slip-events-at-the-offshore-hikurangi-subduction-zone-in-2019-using-gnss-insar-and-seafloor-geodetic-data

Spatiotemporal Evolution of Slow Slip Events at the Offshore Hikurangi Subduction Zone in 2019 using GNSS, InSAR, and seafloor geodetic data

K. Woods[1], L. M. Wallace[2,3,4], C. A. Williams[5], I. J. Hamling[5], S. C. Webb[6], Y. Ito[7], N. Palmer[5], R. Hino[8], S. Suzuki[8], M. K. Savage[1], E. Warren-Smith[5] and K. Mochizuki[9]

[1]School of Geography, Environment and Earth Sciences, Victoria University of Wellington, Wellington, New Zealand.

[2] GEOMAR Helmholtz Centre for Ocean Research, Kiel, Germany.

[3] Institute of Geosciences, Christian-Albrechts-Universität zu Kiel, Kiel, Germany

[4]Institute for Geophysics, University of Texas, Austin, Texas, USA.

[5]GNS Science, Lower Hutt, New Zealand

[6]Lamont-Doherty Earth Observatory, Columbia University, Palisades, New York, USA.

[7]Disaster Prevention Research Institute, Kyoto University, Kyoto, Japan.

[8]Graduate School of Science, Tohoku University, Sendai, Japan.

[9]Earthquake Research Institute, University of Tokyo

Corresponding author: Laura Wallace (lwallace@utexas.edu)

Key Points:

- Central Hikurangi slow slip events propagate up-dip over a period of weeks to months
- Seafloor geodetic data reveal that shallow slow slip events may last longer than onshore GNSS data suggest
- The same portions of a shallow megathrust can host both large seismic and aseismic rupture

Abstract

Detecting crustal deformation during transient deformation events at offshore subduction zones remains challenging. The spatiotemporal evolution of slow slip events (SSEs) on the offshore Hikurangi subduction zone, New Zealand, during February–July 2019, is revealed through a time-dependent inversion of onshore and offshore geodetic data that also account for spatially varying elastic crustal properties. Our model is constrained by seafloor pressure time series (as a proxy for vertical seafloor deformation), onshore continuous Global Navigation Satellite System (GNSS) data, and Interferometric Synthetic Aperture Radar (InSAR) displacements. Large GNSS displacements onshore and uplift of the seafloor (10-33 mm) require peak slip during the event of 150 to >200 mm at 6-12 km depth offshore Hawkes Bay and Gisborne, comparable to maximum slip observed during previous seafloor pressure deployments at north Hikurangi. The onshore and offshore data reveal a complex evolution of the SSE, over a period of months. Seafloor pressure data indicates the slow slip may have persisted longer near the trench than suggested by onshore GNSS stations in both the Gisborne and Hawkes Bay regions. Seafloor pressure data also reveal up-dip migration of SSE slip beneath Hawke Bay occurred over a period of a few weeks. The SSE source region appears to coincide with locations of the March 1947 M_w 7.0–7.1 tsunami earthquake offshore Gisborne and estimated Great earthquake rupture sources from paleoseismic investigations offshore Hawkes Bay, suggesting that the shallow megathrust at north and central Hikurangi is capable of both seismic and aseismic rupture.

Plain Language Summary

Subduction zones, where one tectonic plate dives beneath another are where the planet's largest earthquakes are generated. They also host an important mode of fault slip called "slow slip events", which are essentially earthquakes in slow motion. The Hikurangi subduction zone, where the Pacific Plate subducts beneath New Zealand hosts large and frequent slow slip events near the trench, where the plate boundary emerges at the seabed, requiring seafloor instrumentation to investigate them. Seafloor pressure measurements can track centimeter-level up or down movement of the seafloor during slow slip, and reveal offshore displacement during a large 2019 slow slip event at the offshore Hikurangi subduction zone. The 2019 event involved substantial migration from ~15 km depth to the trench over a period of several weeks. We also show that the same areas which have ruptured in previous seismic earthquakes (that involved faster slip) can also rupture slowly, in slow slip events. This raises the possibility that regions that we currently observe to produce slow slip events could also produce seismic events. This result also demands that more work must be done to understand the physical processes that enable the same part of a fault to rupture both fast and slow.

1 Introduction

Continuous Global Navigation Satellite System (GNSS) stations are typically used to monitor slow slip events (SSEs) located near or beneath onshore networks. For many subduction zones, this is typically restricted to the deeper portions of megathrusts (>30 km depth) that underlie land. This creates a major blind-spot for transient deformation events occurring on offshore subduction zones, which are not amenable to detection and detailed characterization with conventional land-based monitoring techniques. This greatly limits our ability to resolve how tectonic strain is accumulated and released near the trench at subduction zones, in regions where the world's largest and deadliest tsunamis are also generated. Several techniques have been developed over the last 10-20 years to fill this major observational gap, including GNSS-Acoustic arrays (for horizontal displacement rates relative to a known, terrestrial reference frame), Absolute Pressure Gauges (APGs; to detect transient vertical deformation), Direct-path Acoustic Ranging (for horizontal deformation over short distances), and offshore borehole observations of pore pressure changes (as a proxy for volumetric strain) (Gagnon et al., 2005; Bürgmann and Chadwell, 2014; Davis et al., 2015; Wallace et al., 2016; Araki et al., 2017; Urlaub et al., 2018; Yokota and Ishikawa, 2020). Without such instrumentation, understanding of shallow, near-trench slow slip and interseismic couping, and the processes that produce these behaviors is limited.

At the Hikurangi subduction zone offshore New Zealand, the Pacific plate subducts westward beneath the North Island at rates of 20–60 mm/yr (Wallace et al., 2004). The subduction plate boundary is located at 12-15 km depth beneath the east coast of the North Island (Williams et al., 2013) and the trench is located 80-100 km offshore, providing a situation where both shallow (~10-15 km) and deep (>25 km) SSEs can be observed using the land-based continuous GNSS (cGNSS) network operated by GeoNet (www.geonet.org.nz) (see Wallace, 2020, and references therein).

Frequent, shallow SSEs (<15 km) occur primarily offshore at the northern and central Hikurangi margin, recurring every 1–2 years, and lasting from one week to several months (Wallace and Beavan, 2010; Wallace et al., 2012b, 2013, 2016; Koulali et al., 2017). The largest shallow Hikurang SSEs (in 2004, 2010, 2014, and 2019) have produced up to 40 mm of horizontal surface displacements at coastal cGNSS stations. Most shallow Hikurangi SSEs occur on the portion of the plate boundary that appears to be mostly creeping over multiple SSE cycles (based on models of interseismic coupling), while the deep SSEs occur at the down-dip transition from deep locking to aseismic creep (Wallace et al., 2012a; Wallace, 2020). Although the onshore cGNSS network is capable of detecting offshore SSEs, they are located too far from the SSE source to provide detailed constraints on the spatio-temporal evolution of these events, and in particular, whether or not they rupture to the trench. To address this, the 2014 Hikurangi Ocean Bottom Investigation of Tremor and Slow Slip (HOBITSS) experiment was undertaken offshore the Gisborne region to detect seafloor pressure changes during a large SSE in September – October 2014. Using the seafloor pressure data from the array, Wallace et al. (2016) demonstrated the ability of such a network to detect centimetre-level vertical displacement of the seafloor during slow slip, and showed that the 2014 SSE may have reached the trench, with implications for the range of physical conditions that can host slow slip.

Since the 2014/2015 HOBITSS Experiment, we have undertaken rolling deployments of APGs and Ocean Bottom Seismometers (OBS) at the offshore Hikurangi margin to develop a longer-term understanding of shallow SSE behavior and related seismicity there. A deployment in 2018/2019 offshore Gisborne and Hawkes Bay (Barker et al., 2019) captured vertical seafloor displacement during a large SSE in April-June 2019 (Woods et al., 2022). The 2019 SSE is the largest SSE to occur since the large 2014 SSE captured by the HOBITSS experiment. The deployment also represents the first time that APGs have been deployed offshore the central Hikurangi margin, where the trench is furthest (~150 km) from land, and where offshore SSEs are the most difficult to resolve with land-based data. To reveal the spatiotemporal evolution of the 2019 SSE, we utilize the seafloor pressure timeseries (as a proxy for vertical deformation) acquired during the 2018/2019 experiment, as well as three-component continuous GNSS time series, and InSAR Line-of-Sight (LOS) displacements. This represents the first study to globally undertake a joint inversion of GNSS, InSAR, and seafloor geodetic measurements. The improved resolution of the offshore regions of the subduction zone provided by the APGs, reveals new information about slip behaviour on the shallowest portions of subduction zone (not detectable by the onshore GNSS network) including up-dip migration (towards the trench) of slow slip beneath Hawke Bay.

2 Geodetic observations of shallow Hikurangi subduction SSEs in 2019

New Zealand's onshore continuous GNSS network (operated by GeoNet; www.geonet.org.nz) detected a sequence of SSEs offshore the east coast of North Island between February and July 2019 (Woods et al., 2022), with SSE phases of varying onset times and durations along the margin (Figure 1). A small SSE was first detected just to the south of our study area, south of Hawke Bay, with <5 mm eastward motion over 2–3 days in the first week of March 2019 (see Pawanui (PAWA) GNSS station time series and green shading in Figure 1a). Approximately three weeks later, beginning in late March, SSE signals were detected at the Gisborne region, with up to 40 mm of eastward motion occurring over 4–5 weeks. The Gisborne SSE displayed a particularly rapid phase of slip for the first week of the motion, as shown by the Makorori (MAKO) GNSS time series (Figure 1a).

Longer duration SSE-related motion, involving <20 mm eastward displacement, was observed further south at cGNSS sites in the Hawkes Bay area from early April until mid June (see Cape Kidnappers (CKID) station and lavender shading in Figure 1a). Between the Gisborne and Hawkes Bay regions, the GNSS station at Māhia Peninsula (MAHI) detected two rapid SSE phases. 10 mm of eastward motion occurred in the first week of April, followed by more gradual 15–20 mm displacement (likely due to the ongoing SSEs near the Gisborne and Hawkes Bay areas). A further ~10 mm of eastward motion occurred during the first two weeks of May (see the light blue shading in the Figure 1a).

The onshore GNSS displacements are comparable in amplitude to some of the largest offshore Gisborne SSEs observed in 2010 (Wallace and Beavan, 2010) and 2014 (Wallace et al., 2016). Small differences in the displacement patterns exist, such as ~5 mm less subsidence and up to 10 mm more eastward motion at GNSS sites along the Gisborne coast in 2019 compared to 2014, indicating that the 2019 SSEs may have had a slightly different slip distribution compared to previous SSEs. Onshore GNSS site displacements in the Hawkes Bay area during the April/May period (see CKID and MAHI GNSS sites) are similar to amplitudes produced by previous large events in 2013, 2014/2015, and 2016 (Wallace and Eberhart-Philips, 2013; Wallace et al., 2017).

Instruments from the 2018/2019 seafloor geodetic and seismic experiment offshore Gisborne and Hawkes Bay (Barker et al., 2019) were recording during the 2019 SSE (Woods et al., 2022), in addition to two IODP observatories offshore Gisborne (Wallace et al., 2019). The temporary APGs from the seafloor experiment and the pressure sensors at the wellhead of the observatories form two clusters of five seafloor pressure sensors offshore (a) Gisborne and (b) beneath Hawke Bay (see purple circles in Supplementary Figure 1b). Three of the APGs beneath Hawke Bay contained the new A-0-A technology (e.g., Wilcock et al., 2021), to mitigate drift of the pressure sensor, which can be up to several cm/yr (Polster et al., 2009). Woods et al. (2022) processed the pressure timeseries including drift correction, and utilizing reference pressure sites outside of the SSE regions and Ocean Global Circulation Models (OGCMs) to correct for regional oceanographic variations. The processed data revealed that there was 10–33 mm of seafloor uplift offshore Gisborne associated with the 2019 SSE, and 11–27 mm uplift beneath Hawke Bay (Figures 1b, 1c).

The onshore GNSS timeseries (MAKO, near Gisborne) indicates that the SSE starts offshore Gisborne in early April/late March and lasts until the end of April, consistent with the timing of uplift observed in the APG data offshore Gisborne, although the APG data (particularly at near-trench sites KU18-2 and U1518) indicate the event likely persisted near the trench until mid-May. Hawkes Bay GNSS sites suggest the SSE at central Hikurangi lasted from early Aptil to early June, although the seafloor pressure changes at sites near the trench (see LBPR18-4 and POBS18-3) suggest that SSE may have persisted near the trench at central Hikurangi until mid-July (Figure 1; Woods et al., 2022). These delayed near-trench displacements could be due to trenchward migration of the SSE beneath Hawke Bay over the late-May-July period, which is not possible to detect with the shore-based GNSS network. To characterise shallow subduction interface slow slip during the 2019 SSEs, we invert continuous GNSS data, InSAR LOS displacements, and seafloor pressure time series (as a proxy for vertical displacement of the seafloor) for time-dependent slip on the subduction plate boundary.

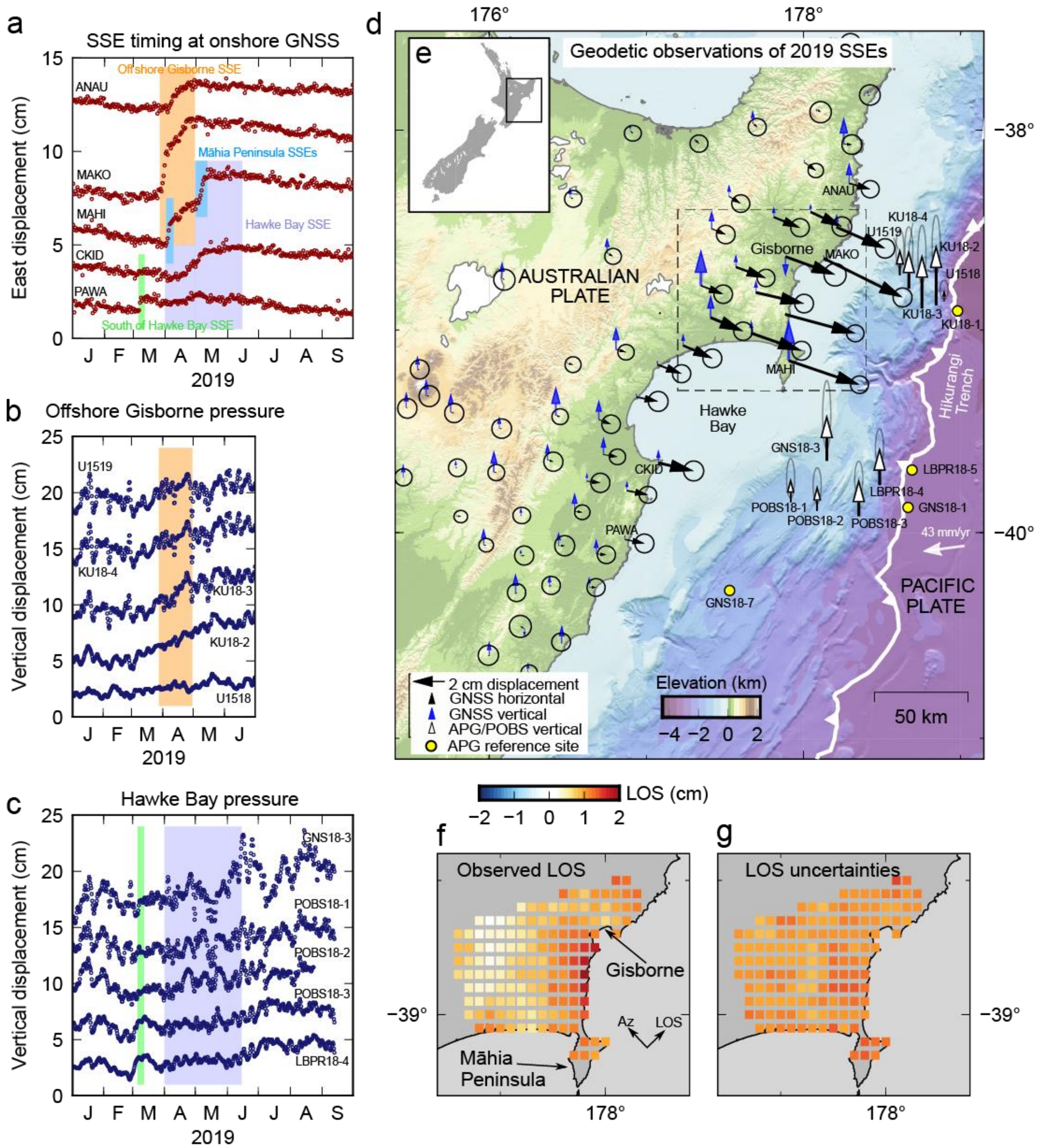

Figure 1: *Onshore and offshore geodetic observations of the 2019 SSE sequences at the shallow Hikurangi subduction zone. a) East component timeseries of GNSS sites (relative to ITRF2014, and offset in the vertical axis to make each signal clear) with the period of detected SSEs highlighted for each site; site locations shown on (d). b) The vertical timeseries data estimated at the Gisborne seafloor pressure array (Woods et al., 2022), with SSE timing from onshore GNSS in (a) indicated by orange shading. c) Vertical displacement timeseries data from the Hawke Bay seafloor pressure array (Woods et al., 2022), with SSE timing detected by onshore cGNSS stations indicated by lavender shading. d) Horizontal and vertical GNSS displacements (and site locations) over the 2019 SSE period. The motion of the Pacific*

plate relative to the Australian plate is denoted with a white arrow (Beavan et al., 2002). Reference APGs used in the processing of the seafloor pressure data are plotted as yellow circles. f) InSAR LOS displacements, following the convention that a positive displacement is motion away from the satellite. As the SSE motion is primarily eastward motion, it is detected as an LOS increase (motion away from the satellite). g) InSAR LOS displacement uncertainties.

3 Onshore and offshore geodetic data

3.1 GNSS Time Series

We include the daily, three-component GNSS time series (acquired and processed by GeoNet, and available at www.geonet.org.nz) of 64 stations along the east coast and central part of North Island (see red triangles in Figure S2 in the Supplementary material) from 1 January 2019 to 1 October 2019 (Figure 1a). The data span the SSE period and several months before and after the SSE to allow allow inter-SSE motion of the GNSS stations to be estimated during the inversion. The GNSS time series provide critical spatiotemporal information about the SSEs (for slip occurring within observable range of the onshore network), such as the onset and termination of slow slip, and periods and general locations hosting the most rapid slip. Prior to inverting the data, offsets due to equipment changes are corrected for in the GNSS time series.

3.2. InSAR LOS Displacements

InSAR LOS change data acquired before and after the SSE improves the onshore spatial resolution of deformation for the Gisborne region. We generate a small baseline network of interferograms spanning the Gisborne region from August 2014 to November 2020 (19 strip map acquisitions from an ascending track 99 of the ALOS-2 mission) using the GAMMA processing software (Werner et al., 2000), which are then input into StamPS (Hooper, 2008; Hooper et al., 2012) to generate small baseline interferograms. Topographic corrections are applied using the ALOS Global Digital Surface Model (30 m horizontal resolution; Tadono et al., 2014; Takaku et al., 2014, 2016; Tadono et al., 2016; Takaku and Tadono, 2017; Takaku et al., 2018, 2020).

The SSE deformation is expected to produce a long wavelength signal across the interferogram, which makes a correction of long wavelength atmospheric or orbital signals using a ramp more challenging as the ramp would also remove the deformation signal. Using predicted LOS displacements, generated by a preliminary SSE model constrained by GNSS sites only, we subtract the SSE deformation signal, fit and subtract a ramp representing remaining atmospheric/orbital gradients, and add the predicted deformation back into the interferogram (similar to the approach of Hamling et al., 2022).

We confirm that the LOS displacement time series is consistent with the onshore GNSS motion in the area, particularly over the February 2019 – July 2019 period we are investigating (Supplementary Figure S3). The resolved 2019 SSE displacement field from the InSAR (see Supplementary Figure S4) is then sub-sampled so the density of data points are reduced, and the locations align with the locations of Green's functions generated for the inversions (see Section 4.0). The resultant LOS displacements can be seen in Figure 1f, where positive changes represent motion away from the satellite — positive LOS changes are equivalent to eastward, northward, and downward (subsidence) motion. A maximum of ~20 mm LOS displacement is detected at the coast near Gisborne, decaying to <5 mm detected displacement ~50 km inland; we note that uncertainties in the LOS displacements generally range from 5-10 mm (Figure 1g).

3.3 Seafloor Pressure as a Proxy for Seafloor Vertical Displacement

The onshore GNSS data provide good temporal and spatial resolution for SSE slip near and below the coast; however, these data lose revolving power for the offshore (< 12 km depth) portions of the subduction zone (see Section 1.0 of the Supplementary Material). To constrain vertical displacement of the seafloor, we use continuous recordings of seafloor pressure (using Absolute Pressure Gauges, or APGs) deployed during the 2019 SSE to better constrain the offshore slip distribution (see processed timeseries from Woods et al., 2022, in Figures 1b and 1c).

The processing of the seafloor pressure data is outlined in detail in Woods et al. (2022), and we summarize the key components of this below. Our procedure first involved the removal of high frequency signals (such as diurnal and semidiurnal tides) using a 2-day corner lowpass filter, and then a correction for instrumental drift of the APGs equipped with ambient-zero-ambient (A-0-A) technology. After low-pass filtering, significant non-tidal oceanographic signals remain with amplitudes on the order of a few to ten cm, which will mask any pressure changes due to vertical tectonic deformation (which we expect to be on the order of a few cm). Similar to previous studies (Wallace et al., 2016; Frederickson et al., 2019; Inoue et al., 2021) which assume a large component of these non-tidal signal are common-mode across the footprint of the array, we mitigate this noise by subtracting the pressure record of an APG located outside the expected SSE deformation region. The Gisborne APG array reference site was located on the subducting plate (KU18-1) and a composite reference site (consisting of an APG located along-strike (GNS18-7) and the average of two subducting plate APGs (GNS18-1 and LBPR18-5)) was used for the Hawke Bay array (see Fig. 1d for reference site locations; Woods et al., 2022).

A further correction was then included to account for contributions from long-period ocean variability between the reference sites and main arrays. This involved subtracting the weighted average of 90-day window moving mean simulated pressure time series representing the oceanographic variations between each APG and reference site. The simulations were generated using the global Ocean General Circulation Models (OGCMs): ECCO2 (Estimating the Circulation and Climate of the Ocean project; Menemenlis et al., 2008), GLORYS (GLobal Ocean ReanalYsis and Simulation; Lellouche et al., 2021), and HYCOM (HYbrid Coordinate Ocean Model; Cummings, 2006; Cummings and Smedstad, 2013; Helber et al., 2013), with the weighting of each OGCM determined by the cross-correlation of the observed and simulated pressure data. Following the ocean noise corrections, the APGs not equipped with A-0-A self-calibration, were drift-corrected by fitting a linear function to data outside the period of slow slip (indicated by the onshore GNSS data in Figure 1a), which was subtracted from the APG time series.

The seafloor pressure data are processed using 1-hour sampling and then sub-sampled to a 4-hour average value for input to the time-dependent inversion. Vertical displacement time series at ten offshore locations are included, from 1 January to 1 October 2019 for Hawke Bay APGs, and from 1 January to 1 July 2019 in the Gisborne region (with post-July data excluded due to the presence of large amplitude, winter ocean noise — confirmed with the seafloor pressure simulations from the OGCMs).

4.0 Time-dependent inversion of the onshore and offshore geodetic data for slip on the megathrust

To resolve the spatial distribution and temporal evolution of the 2019 SSE sequence, we use the non-linear, time-dependent inversion software TDEFNODE (McCaffrey, 2009). The three-component GNSS time series, InSAR LOS displacements, and seafloor vertical displacement time series data (Table 1) are inverted for eight transient slip sources characterising the 2019 slow slip event sequence (see Tables S1 and S2 in the supplement for a summary of the source parameters and constraints on the source parameters).

The TDEFNODE inversion framework includes a set of tectonic blocks, each with a different Euler pole of rotation and boundaries represented by known active faults (Supplementary Figure S2; Wallace et al., 2004, 2012a). We define the Hikurangi subduction interface using a grid of 24 by 11 nodes extracted from the interface geometry of Williams et al. (2013), along which the SSE transients are assumed to occur. We use the poles of rotation of Wallace et al. (2012a) and the plate boundary geometry to fix the rake of slip to reduce the number of free parameters solved for in the inversion.

To relate surface displacement at the onshore and offshore geodetic sites to slip on subduction megathrust patches, we generate our own Green's Functions using the finite element code PyLith (Aagaard et al., 2013; 2017a; 2017b). This allows us to account for spatially variable elastic properties, following the method of Williams and Wallace (2015). Most crustal deformation models to fit geodetic data assume dislocations in a homogeneous elastic half-space, utilizing analytical equations that relate fault slip to surface displacement (Okada, 1985). By undertaking inversions of geodetic surface displacements for slip on the megathrust using realistic elastic properties (constrained by seismic velocities) at the Hikurangi subduction zone, Williams and Wallace (2015, 2018) demonstrate that the assumption of homogeneous elastic properties results in an under-estimation of slip for offshore Hikurangi SSEs (by up to 70%), and an overestimation of slip (by up to 20%) for deep Hikurangi SSEs. This has important implications when trying to understand the role of SSEs in accommodating the plate motion budget. To account for heterogeneity of elastic properties in the deformation models, we use Green's functions relating surface deformation response to slip on all patches with elastic properties constrained by the New Zealand-wide seismic velocity model (Eberhart-Phillips et al., 2010; Eberhart-Philips and Bannister, 2015; Eberhart-Phillips and Reyners, 2012; Reyners et al., 2014).

The time-dependent inversion code TDEFNODE (McCaffrey, 2009) has the advantage of reducing the number of free parameters by representing spatiotemporal slip evolution as more simplified basis functions, rather than inverting directly for slip (or slip rate) on discrete fault patches during individual time steps. This removes the need for extensive regularization and smoothing that must be implemented in some other time-dependent inversions (such as the

Network Inversion Filter; Miyazaki et al., 2006; Bartlow et al., 2011). Here, SSE transients are represented through basis functions in space and time. The slip distribution is characterised using a 2D Gaussian function:

$$S(x,w) \;=\; Ae^{-0.5\left(\frac{dw}{d1}\right)^2} e^{-0.5\left(\frac{dx}{d2}\right)^2}, \qquad (1)$$

where S(x,w) represents the spatial slip distribution (x is the along-strike position and w is the along-dip position) as a function of the amplitude (A), Gaussian down-dip and along-strike width of the source ellipse (d1 and d2), and the down-dip and along-strike distance (dx and dw) from a node to the Gaussian mean (longitude and latitude of the centre of the slip source). The transient time history is characterised with a Gaussian temporal function:

$$S(t) \;=\; Ae^{\frac{\left(t-(T_O+3T_C)\right)^2}{T_C}}, \qquad (2)$$

where Tc is the transient time constant (a measure of duration) and To, the transient origin time. To = Tmax – 3Tc, where Tmax is the time of peak slip rate.

The number of transients resolved in the TDEFNODE inversion must be pre-defined. Eight transients (i.e., eight SSE transient sources, see Table S2 in the Supplement) were chosen by visually inspecting the GNSS and APG time series and identifying the number of phases of slow slip based on the onset, duration, and location of SSE signals along the margin (see Figures 1a, 1b, and 1c). An exception to this classification is the first period of rapid motion detected at Māhia Peninsula (see early April SSE signal at MAHI in Figure 1a), which we do not model as very few other sites recorded that phase of deformation, as it would be largely constrained by a single GNSS site on Māhia Peninsula. The SSE transient sources are stationary in space in the TDEFNODE inversion, and we effectively capture the SSE migration along the interface by superimposing multiple transient sources with different spatial and temporal characteristics.

In addition to the SSE transient source model parameters, we solve for 6-monthly and yearly seasonal trends in the vertical component of the GNSS time series as these are larger amplitude than the vertical tectonic signals (horizontal-component seasonal signals are less obvious in the time series). We also solve for the inter-SSE rates of the three components of most GNSS sites. The inversion struggles to estimate the inter-SSE velocity of the north component at a few of the

GNSS sites (orange triangles in Figure S2 in the Supplement), therefore this component of those sites is fixed to the rates calculated by Wallace et al. (2012b), estimated from a longer timeseries of data.

Multiple iterations of grid searches and downhill simplex minimisation are performed to find the set of model parameters that minimise the reduced χ_n^2 statistic plus any inversion penalties to keep parameters within physically plausible limits:

$$\chi_n^2 = \frac{\sum \frac{r^2}{(sF)^2}}{dof}, \qquad (3)$$

where r is the residual (observed data minus the best-fitting model), s is the data standard deviation, F is a scaling factor applied to each data file, and dof is the number of degrees of freedom (64,643: the total number of data points in Table 1 minus 64 free parameters). The seafloor displacement time series and InSAR data are weighted more heavily in the inversion (using the scaling factor, F, in Equation 3), compared to the GNSS time series (which artificially dominate the inversion due to the large number of data), as the InSar and Seafloor pressure datasets contain fewer data points. More information on the inversion procedure can be found in section 2.0 of the Supplementary materal).

Table 1: Summary of geodetic data inverted to resolve the 2019 SSEs. Information includes the type of geodetic data inverted, the source of the data processing, displacement information (e.g., east–E, north–N, up–U, Line-of-Sight–LOS), the number of sites and data points in the dataset, the time period covered, and the weighting factor used in the inversion.

Data type	Source of processing	Displacement information	Number of sites	Number of data points	Time period	Inversion weighting
Continuous GNSS	GeoNet	E N U	64	51,513	1 Jan 2019 – 1 Oct 2019	1
Seafloor pressure	Woods et al., 2002	U	10	13,050*	1 Jan 2019 – 1 Oct 2019	0.25
InSAR	This study	LOS	-	144	1 Jan 2019 – 1 Aug 2019	0.05

*8,700 simulated noise (horizontal component) and 4,350 real data points.

5.0 Results

The overall slip distribution resolved by our time-dependent inversion of onshore and offshore geodetic data is shown in Figure 2. Our best-fitting solution has a reduced χ_n^2 value of 1.21, and generally fits the onshore and offshore data to within uncertainty. The slip distribution includes two main loci of slip, one reaching 150–200 mm offshore Gisborne at 6–9 km depth, and the other reaching >200 mm slip at 9–12 km depth beneath Hawke Bay. These large slip patches appear to be separated by a region of low amplitude slip offshore Māhia Peninsula, although the lower inferred slip between the two primary slip patches may also be due to the lack of offshore observations between the two seafloor arrays, where the model is not well-resolved (see spatial resolution tests in Section 1.0 of the supplemental material). Substantial spatiotemporal evolution of the event is evident in the onshore and offshore geodetic timeseries (Figure 1), which we discuss in detail in sections 5.1 and 5.2.

The observed onshore and offshore displacements for the entire SSE period of February–July (including the short burst of slow slip offshore southern Hawkes Bay in February), are fit well by the slip model in Figure 2. Although most timeseries are fit very well for all sites (see Supplementary Section 4.0 for fits to all timeseries), the north component of the MAHI GNSS station on Māhia Peninsula is not as well-fit with our best-fitting model (Figure 3). The misfit may be a result of inaccuracies in the physical assumptions made in the inversion, such as prescribed direction of slip, the subduction interface geometry, and elastic properties. However, we expect that this misfit is more likely related to needing a more complex slip model than can be captured in the TDEFNODE inversions without addition of more free parameters. We will examine the Gisborne and Hawkes Bay regions separately to highlight features of the slip model for those two regions.

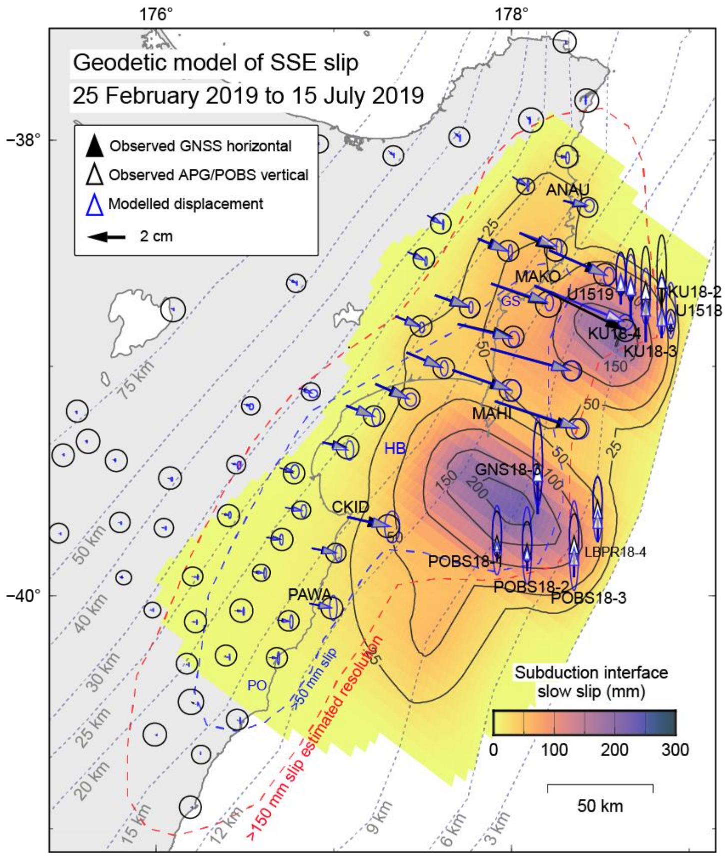

Figure 2: *The best-fitting subduction interface SSE slip distribution from 25 February 2019 to 15 July 2019 in millimetres (see color scale). Solid black vectors indicate observed onshore total horizontal displacement during the SSE period and black outlined vectors are the observed offshore vertical displacement (Woods et al., 2022). Blue outlined vectors show the displacement from the best-fitting slip distribution. Grey dashed contours denote the depth to the subduction interface (labeled in km) (Williams et al., 2013). The estimated model resolution, for >50 mm and >150 mm of slip, is indicated with blue and red dashes respectively (based on the spatial resolution tests in Supplemenary Material section 1.0). The locations of Gisborne (GS), Hawke Bay (HB), and Pōrangahau (PO) are also shown.*

5.1. Slow slip offshore Gisborne

Our model does a reasonable job capturing the rapid and more gradual phases of the Gisborne SSE motion evident in the onshore GNSS timeseries (see ANAU and MAKO east component time series in Figure 3, and fits for all other GNSS and APG sites in Section 4.0 of the Supplementary Material). The rapid early motion detected onshore from 25 March to 8 April (e.g., MAKO in Figures 2-3) is well-fit by SSE slip of ~65 mm over 11 days, on a ~55 km by ~80 km patch located along the interface located immediately seaward of the Gisborne coastline, northeast of Māhia Peninsula (also see Figure 4). It is during this rapid early phase that small to moderate earthquakes are the most abundant, particularly along the southern edge of the slipping patch, with locations close to the plate interface (Figure 4, see 1-8 April panel). As the APG data are noisier than the onshore GNSS timeseries, a similar rapid uplift signal during this rapid early phase is not obvious, but there was an overall uplift/pressure decrease signal at all APGs through the entire duration of the SSE, with 10–33 mm of estimated uplift (Figure 5; Woods et al., 2022). To fit both the APG data and GNSS timeseries, our models suggest a second, longer-lived (early April to mid May) phase of slip immediately following and updip of (at 6-9 km depth) the initial rapid 11-day pulse (Figure 4). This characterises the temporal signature of the APG vertical displacement time series well, and also fits the onshore GNSS timeseries during this period. This suggests that while there was more rapid slow slip detected onshore occurred close to the coast (between 25 March and 8 April), there was also a more gradual patch of larger slow slip centred further up-dip (between early April and mid to late May, as seen in Figure 4) detectable in the APG data.

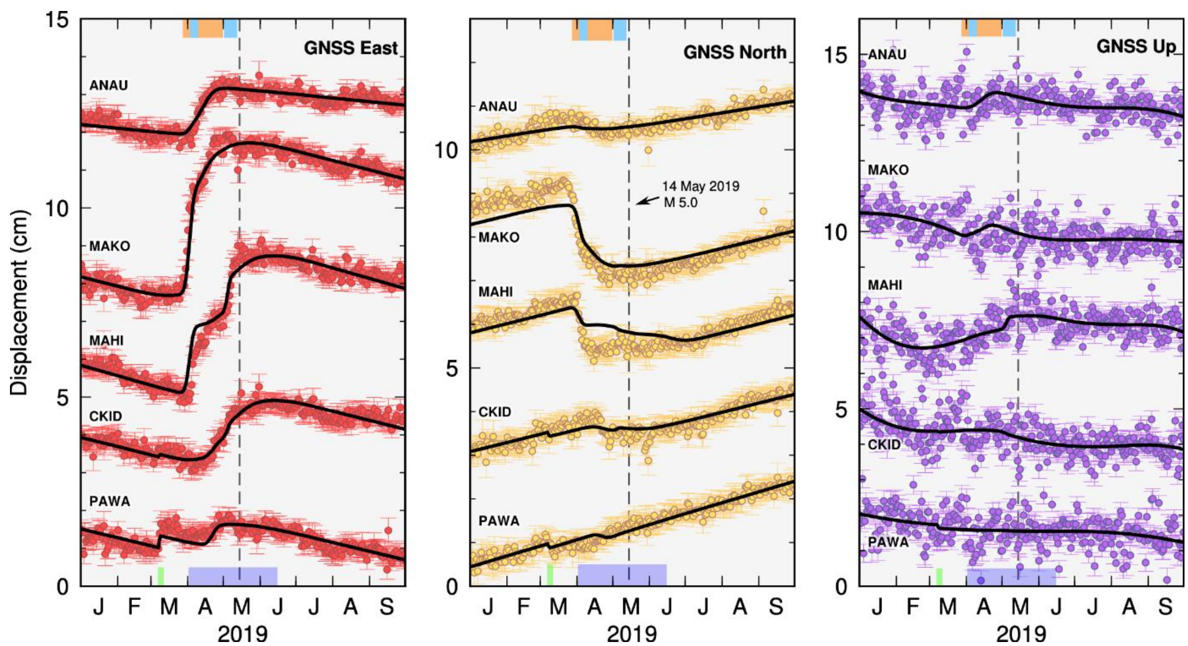

Figure 3: *The observed and predicted east, north, and up GNSS timesries for ANAU (Anaura Bay), MAKO (Makorori), MAHI (Māhia Peninsula), CKID (Cape Kidnappers), and PAWA (Pawanui; see Figure 1 for locations). The observed data are shown as red (east component), gold (north component), and purple (up component) data points, with the predicted displacement time series (from the best fitting model in Fig. 2) indicated with a solid black line. The GNSS time series shown are relative to ITRF2014 and are not detrended for inter-SSE motion. The timings (discussed in the text) of SSE signals detected at*

onshore GNSS stations are indicated (at the top of the panels) with orange shading for Gisborne (MAKO), light blue for Māhia Peninsula (MAHI), and green and lavender shading for Hawke Bay (PAWA and CKID respectively) at the bottom of the panels.

The slip model fits the InSAR LOS displacements well (Figure 6), with LOS change residuals less than 10 mm (within the LOS data uncertainties). To fit the observed, large (~40 mm) onshore horizontal displacements near Gisborne, high amplitude subduction interface slip beneath the offshore region is required. Due to the basis functions used in the inversion to reduce the number of free parameters, (such as modelling a slip phase as a stationary transient following a single temporal function), the slip model does not capture all of the detailed features of the SSEs visible in the GNSS timeseries, such as slight variations in the onset time of the rapid early SSE phase detected along the Gisborne coast, which may indicate some along-strike migration of the event (see GISB, PARI, and MAKO time series in Supplementary Material section 4.0). In addition to this, there is minor misfit to the north-component time series of ANAU and MAKO (Figure 3), with the southward motion of the onshore sites under-estimated, indicating that there is additional spatiotemporal complexity of the 2019 SSEs that cannot be captured by our model. All time series observations and comparisons to the best-fitting model can be seen in section 4.0 of the Supplementary Material.

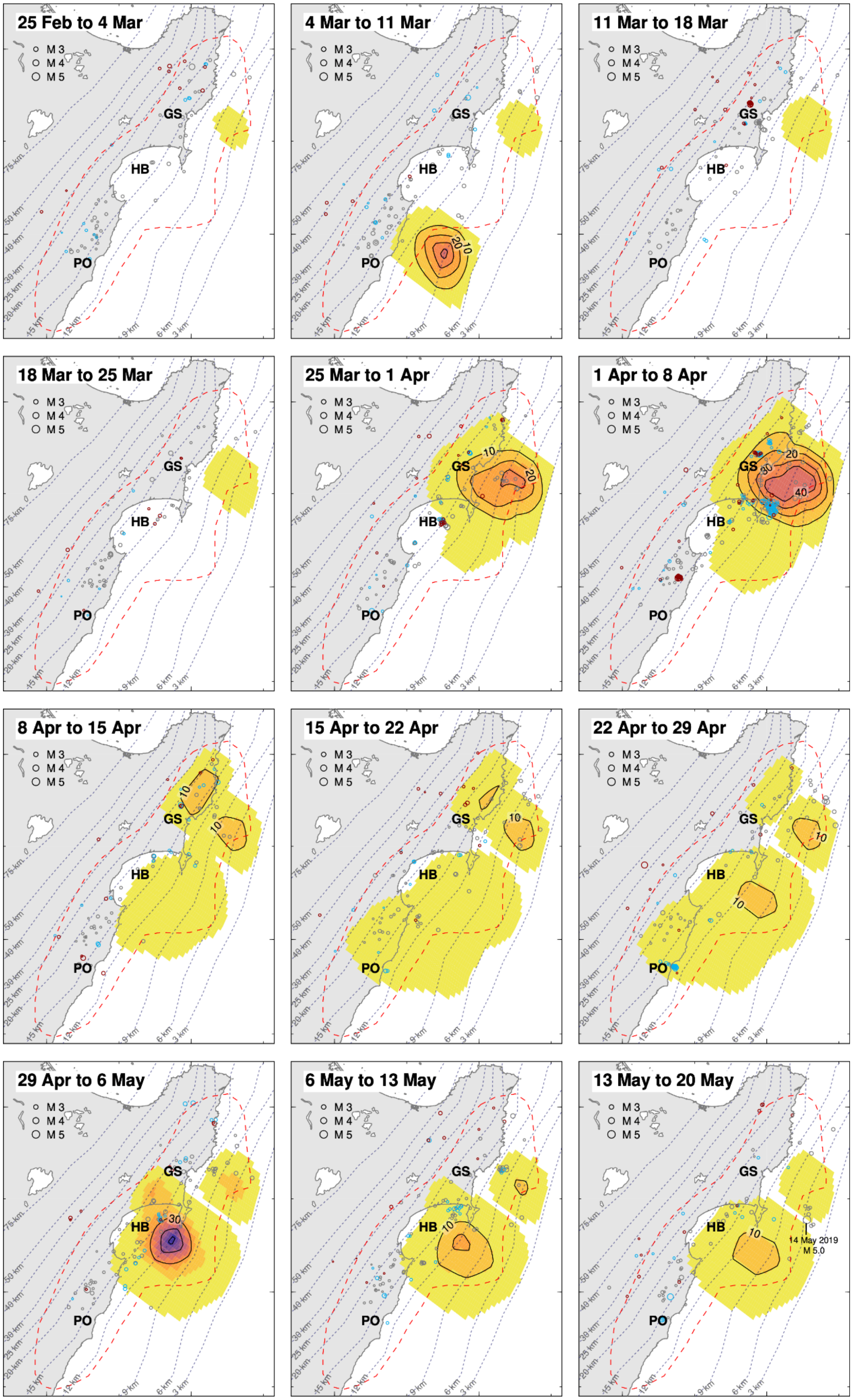
25 Feb to 4 Mar
4 Mar to 11 Mar
11 Mar to 18 Mar
18 Mar to 25 Mar
25 Mar to 1 Apr
1 Apr to 8 Apr
8 Apr to 15 Apr
15 Apr to 22 Apr
22 Apr to 29 Apr
29 Apr to 6 May
6 May to 13 May
13 May to 20 May
M 3
M 4
M 5
GS
HB
PO
75 km
50 km
40 km
30 km
25 km
20 km
15 km
12 km
9 km
6 km
3 km
10
20
30
40
14 May 2019
M 5.0

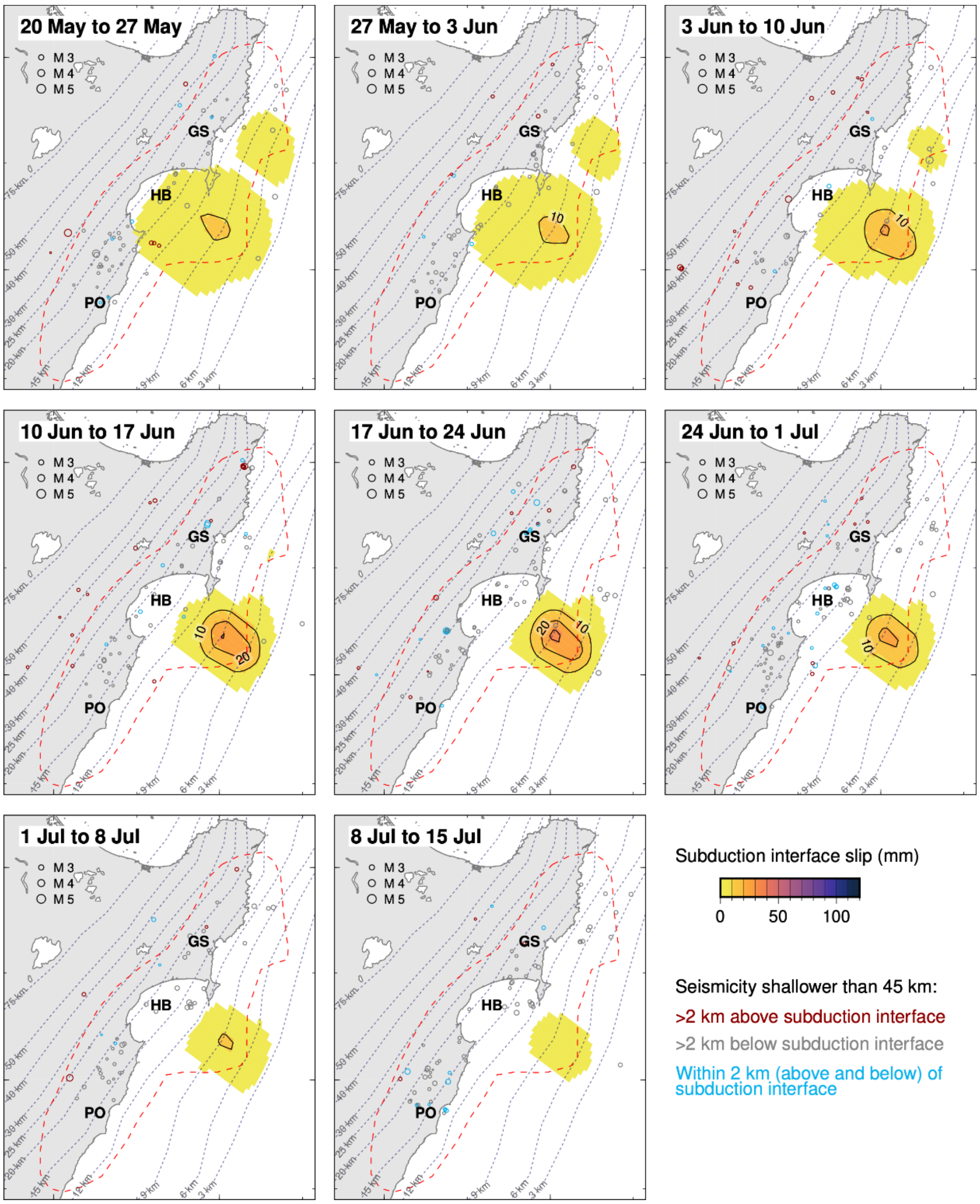

Figure 4: *Weekly time slices of the best-fitting subduction interface SSE slip distribution from 25 February 2019 to 15 July 2019 in millimetres. Seismicity detected by GeoNet (https://www.geonet.org.nz/data/types/eq catalogue) during the 2019 SSEs at depths shallower than 45 km is presented for: earthquakes located more than 2 km above the subduction interface (dark red circles), earthquakes located more than 2 km below the subduction interface (grey circles), and earthquakes located within 2 km (above and below) the interface (blue). The estimated model resolution, for >150 mm of slip, is indicated with red dashes (determined from the spatial resolution tests in the Supplementary Material section 1.0). The locations of Gisborne (GS), Hawke Bay (HB), and Pōrangahau (PO) are also shown.*

Overall, the offshore Gisborne SSE slip in 2019 appears to have ~100 mm lower peak slip than the 2014 event (Wallace et al., 2016), with the 2014 peak slip localised on the western side of the 2019 peak slip (see Figure 7). These differences can most likely be attributed to more comprehensive coverage of the seafloor APGs providing better constraints on the offshore slip distribution during the 2014 SSE, but could also be a result of variations between the 2014 and 2019 slip episodes. The largest seafloor vertical displacements (27–54 mm) estimated for the 2014 SSE are located close to the peak of the 2014 SSE slip. The 2019 APG network spans the northern edge of the 2014 SSE slip distribution (approximately 20 km north of the region of peak slip). For the sites from the 2014 HOBITSS experiment that are in similar locations to our 2019 Gisborne APGs, we see a 3–8 mm difference in vertical displacement estimates when comparing the 2014 and 2019 SSEs (Woods et al., 2022; Figure 7), which is a small difference and can likely be attributed to a combination of slightly varying slip distributions, seafloor instrument locations, and/or pressure data processing techniques. Due to the similarity in the 2014 and 2019 onshore and offshore displacement patterns, we infer that the 2019 SSE offshore Gisborne could have involved higher peak slip (possibly as large as the 2014 SSE); however, we don't have sufficient coverage overlying the regions of largest slip to resolve this.

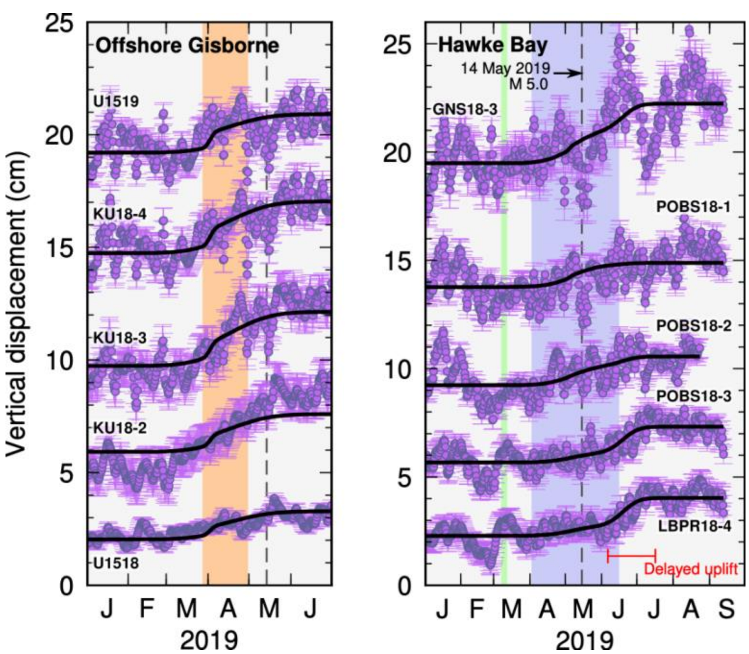

Figure 5: *The observed and predicted seafloor vertical displacement timeseries, of the Gisborne APGs (left) and Hawke Bay APGs (right). The observed data are shown in purple and the predicted displacement time series (based on our best-fitting model) are indicated with solid black lines. The timing of onshore GNSS- detected SSE signals discussed in the text are indicated with orange shading for*

Gisborne (MAKO), and green and lavender shading for Hawke Bay (PAWA and CKID respectively). The site locations can be seen in Figure 1.

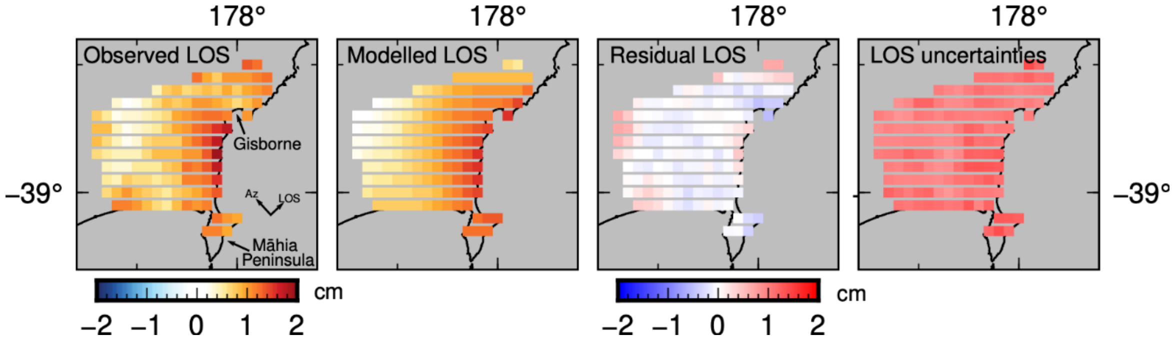

Figure 6: *Observed, modelled, residual (observed minus modelled), and uncertainty of InSAR LOS data in centimetres, with the convention that a positive displacement is motion away from the satellite. This means that subsidence and eastward and northward motion appears as a positive LOS displacement.*

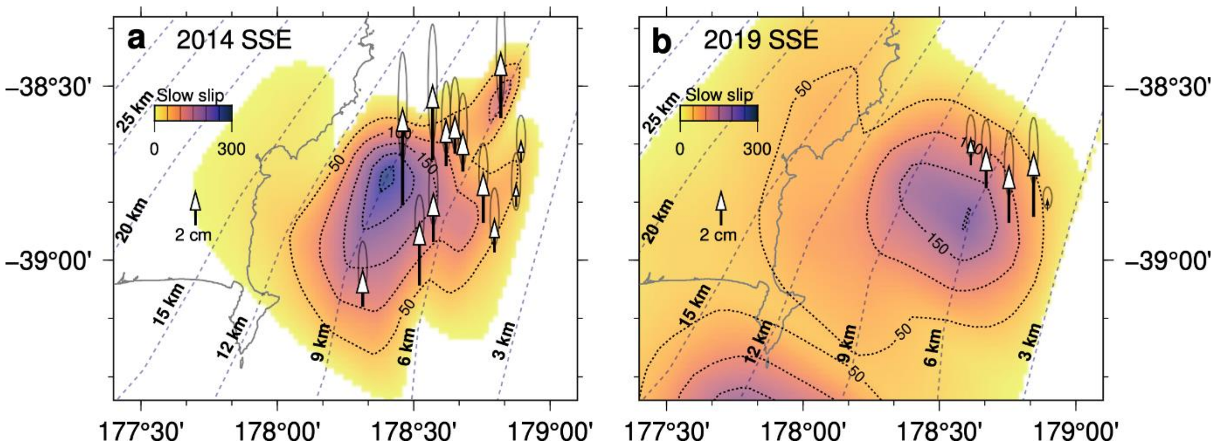

Figure 7: *Offshore vertical displacement and slip distribution comparison between the 2014 and 2019 Gisborne SSEs. a) the 2014 SSE slip distribution with contours in millimetres, and the offshore vertical displacement estimated by Wallace et a (2016). b) the 2019 SSE slip distribution with contours in millimetres, and offshore vertical displacement by Woods et al. (2022). Subduction interface depth contours are indicated in kilometres (Williams et al., 2013).*

5.2. Slow Slip offshore Hawke Bay

Slow slip appears to evolve substantially offshore the Hawkes Bay region over the March to July period. Our model indicates that the 2019 SSE sequence began with a small patch of ~30 mm of slow slip in the offshore region south of Hawke Bay between 4 March and 11 March (Figure 4), where a small eastward displacement (<5 mm) was detected at the PAWA GNSS station (Figure

3), which is fit as up to 20-30 mm of slip at 9 km depth. We note that our best-fitting model under-estimates the eastward motion at PAWA at the beginning of March and then attempts to compensate for this misfit to the time series by over-estimating the slip amplitude at the southern extent of the main Hawke Bay SSE slip in April/May 2019 (Figure 3). The spatial distribution of the resolved slip patch during this initial phase is poorly constrained due to the lack of offshore instrumentation here and the small number of onshore GNSS sites that detected the SSE (see spatial resolution tests in Supplementary Material section 1.0).

There is a rapid (~7 days) pressure decrease (possible uplift signal) observed at seafloor pressure sites LBPR18-4 and POBS18-3 during the week before the onshore signal observed at PAWA in March (Figure 5). It is challenging to determine whether the rapid pressure decrease observed at both sites is due to seafloor uplift (related to slip near the trench during this short-lived SSE detected >100 km away at PAWA) and/or ocean noise. Our inversion struggles to find a slip model that fits both onshore and offshore displacements using a single, stationary transient, and a more complex slip model (with a larger number of free parameters) would be needed to fit the APG data near the trench. Given the uncertainty as to whether the signals observed at the two APG sites in March is tectonic or oceanographic, we do not attempt to fit this signal, although we raise the possibility that the SSE observed at PAWA was preceded by a pulse of near-trench slip close to sites LBPR18-4 and POBS18-3.

Onset of SSE-related displacement beginning in early April at Hawkes Bay GeoNet GNSS sites (e.g., CKID in Figures 2 and 3) is well-fit by a ~100 km^2 patch of slip (up to 200 mm over ~2 months) centred on the offshore region due south of Māhia Peninsula. Our best-fitting model suggests a patch just up-dip of this region began slipping in late May, persisting until the middle of July (Figure 4). This later period of slip is constrained largely by the Hawke Bay APG data, where clear pressure decrease (uplift) signals of LBPR18-4 and POBS18-3 appear delayed by six weeks relative to the onset of SSE motion at the onshore GNSS stations (as shown in Figures 1c and 5). Our best fitting model suggests ~130 mm of slip occurring on the shallow (4–11 km depth) plate interface over a 40-day period. A small amount of eastward displacement is also visible on CKID throughout this period, indicating that the cGNSS are consistent with longer duration offshore slip.

Of the Hawke Bay APG sites, we observe the largest vertical displacements at GNS18-3 (27 mm; Figure 5); however, the large amplitude oceanographic fluctuations present in the GNS18-3 pressure data from May onward indicate that some component of this uplift signal could be influenced by oceanographic effects. If the total vertical displacement estimated at GNS18-3 is too large (as a result of oceanographic contributions) then the resolved subduction interface slip could be an over-estimation. An inversion of the 2019 SSEs constrained using only the onshore instrumentation suggests that 60–70 mm of subduction interface slip south of Māhia Peninsula explains the SSE motion detected onshore; however, the onshore GNSS data provide little to no resolution for the portions of the interface within 20-40 km of the trench, so this should be considered a minimum (Figure S1 in the Supplementary Material). Given the possibility that oceanographic fluctuations at GNS18-3 may lead to an overestimate of vertical displacement at that site, we expect that the true value of the subduction interface slip for the 4–11 km depth SSE region in late May–mid July 2019 period lies somewhere between 60 mm (using only GNSS data) and ~130 mm (including APG data).

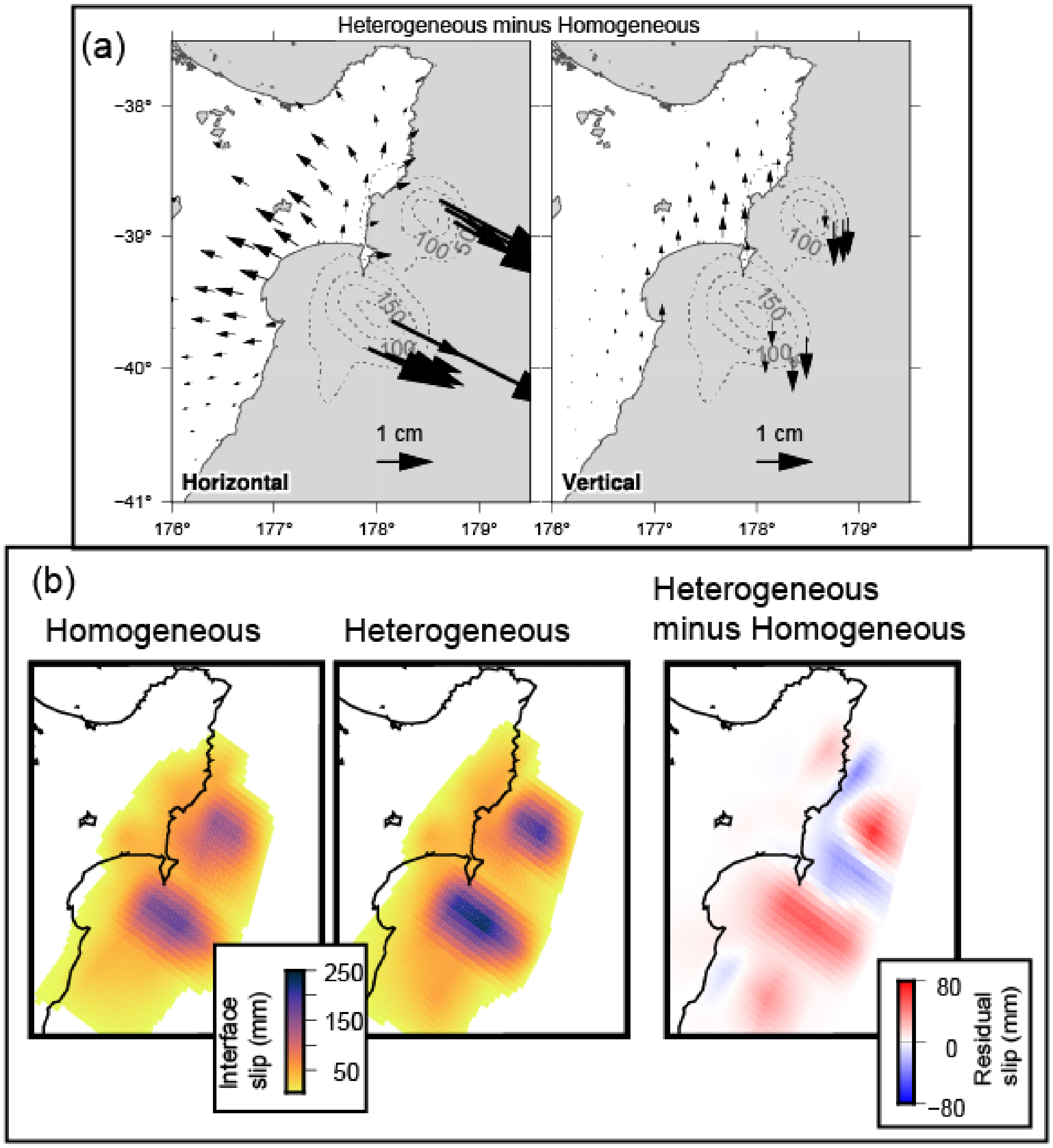

Figure 8: *Comparison of results using homogeneous elastic properties and realistic, heterogeneous elastic properties in our slip inversions. (a) Predicted displacement differences using the our best-fitting slip distribution (Fig. 2) using heterogeneous elastic properties versus a homogeneous elastic half-space. Displacement differences are the displacements at each site from the heterogeneous elastic model minus the displacements predicted by a homogeneous model. Left: Horizontal displacement differences for onshore GNSS and offshore APG sites; vectors pointing east indicate displacements in the heterogeneous model are higher, while vectors pointing west indicate smaller displacements in the heterogeneous model compared to the homogeneous model. Right: Vertical displacement differences for onshore GNSS and offshore APG sites, with vectors pointing up meaning higher displacement in the heterogeneous model compared to the homogeneous model, and vectors pointing down meaning lower displacement in the heterogeneous model. The slip model is indicated with dashed contours, in millimetres. (b) Slip*

distributions resolved when using a homogeneous elastic property model (Left) and a heterogeneous elastic property model (Center). Right panel shows the slip distribution from the Homogeneous model subtracted from the Heterogeneous model (e.g., positive values indicate higher slip amounts in the Heterogeneous slip model).

5.3 Impact of Elastic Properties on Slip Model

The large elastic property contrasts between the slab and forearc at subduction zones strongly influence the resulting crustal deformation models (Willams and Wallace, 2015, 2018). To assess the influence of realistic elastic properties on our slip models, we forward model the displacements produced by our resolved slip distribution for the 2019 SSE using both heterogeneous and homogeneous Green's functions (see description of Green's function generation in Section 4 and Williams and Wallace, 2018), and calculate the difference between the surface displacement patterns. (Figure 8). Using heterogeneous Green's functions predicts less horizontal motion at sites located on the down-dip side of the SSE area and more horizontal motion at sites located closer to the SSE source on the Gisborne coast and offshore (compared to uniform elastic models, using identical slip distributions). In the vertical component, for equivalent models we see that the heterogeneous assumption predicts less uplift offshore and less subsidence (or more uplift) onshore (although the onshore vertical displacement differences are small, <5 mm). This is consistent with the findings and synthetic 2-D models of Williams and Wallace (2018), where they show the displacement differences are explained by by interpreting the heterogeneous contributions to the displacement field as body forces reflecting the interactions of material property gradients with the strain field. These additional body forces (not present in the homogeneous solution) perturb both the horizontal and vertical displacement fields with respect to the homogeneous solution, yielding significantly different results for homogeneous versus heterogeneous models when the same SSE slip distribution is applied to both.

For a set of surface displacements we would therefore expect the resolved subduction interface slip amplitude and distribution to vary depending on the assumptions made about elastic structure. The forward-model example in Figure 8 indicates that accounting for realistic, heterogeneous elastic properties produces more SSE slip (as less uplift is predicted for the same amount of slip) compared to the slip distribution when assuming a homogeneous half-space.

Inversions using a heterogeneous or homogeneous half-space reveal that the heterogeneous model estimates as much as 70–80 mm more slip along the interface beneath the offshore Gisborne and Hawke Bay APG arrays (Figure 8b). This is consistent with the findings of Williams and Wallace (2018), implying that the homogeneous half-space assumption leads to an under-estimation of the amplitude of offshore SSE slip.

We compare the slip models derived using homogeneous and heterogeneous properties (Figure 8b) in terms of seismic potency (a measure of the size of an event), calculated by integrating the slip over the slip area, which means it is independent of the material elastic property variations (i.e., shear modulus). We estimate that the heterogeneous slip distribution is overall ~15% higher in seismic potency than the resolved slip distribution using the homogeneous Green's functions. This is a smaller difference than what Williams and Wallace (2018) found for the 2014 SSE offshore Gisborne, where they calculated ~64% higher seismic potency, using the heterogeneous Green's functions. Our tests indicate that less slip is resolved closer to the coast in the heterogeneous model relative to the homogeneous model for the 2019 SSEs, beneath a region with no seafloor pressure data. Williams and Wallace (2018) had a much larger seafloor pressure dataset to constrain their slip model, meaning the 2014 SSE slip distribution is better resolved than our model of the 2019 SSEs, and likely explains some of the differences we observe compared to Williams and Wallace (2018). The interaction of the strain field with the gradients of the material properties strongly influence the slip model results, and and this will vary depending on the details of the slip distribution, which may another source of the difference between our results and those of Williams and Wallace (2018).

6 Discussion

6.1 Shallow SSE regions can also rupture seismically

Although the rheology, frictional properties and physical processes producing episodic SSE behavior is widely discussed and debated (Liu and Rice, 2007; Segall et al., 2010; Leeman et al., 2016; Im et al., 2020; Shreedharan et al., 2023), many studies have suggested that regions hosting slow slip events and/or steady creep are unlikely to rupture seismically (Hyndman, 2013; Dixon et al., 2014; Rolandone et al., 2018). Such assumptions have propagated into seismic hazard models (Petersen et al., 2020; Wong et al., 2014).

In contrast to common assumptions about the seismic rupture potential of SSE regions, there is strong evidence for past, large subduction earthquake rupture within the source area of the Gisborne and Hawke Bay SSEs. Two Mw ~7.0 earthquakes occurred in March and May of 1947, located within the Gisborne SSE region (Bell et al., 2014). These events had mechanisms consistent with the plate interface, and are considered “tsunami earthquakes” as they caused much larger tsunami (6-10 m) than expected given their magnitude (Doser and Webb, 2003; Downes et al., 2000). Along the Hawke Bay coastline, evidence for repeated meter-scale abrupt coastal subsidence events (with some accompanied by tsunami deposits) are evidence for for great (M ~8.0) subduction interface rupture offshore the Hawkes Bay region (Clark et al., 2019; Cochran et al., 2006; Hayward et al., 2015). The source of such events coincide with the source of shallow Hawke Bay SSEs, such as the SSE we observed in 2019 (Fig 9). Although a recent re-evaluation of these data suggests that some of these coastal deformation events may be related to splay faulting in the upper plate, it is likely that at least some of these subsidence events are due to subduction interface ruptures beneath Hawke Bay, or a combination of shallow subducton interface rupture and splay faulting (Pizer et al., 2023).

The spatial coincidence of large seismic rupture and SSEs offshore Gisborne and Hawkes Bay suggest that shallow SSE regions may also host hazardous seismic slip. Although onshore GNSS stations have previously revealed the existence of large SSEs offshore Hawkes Bay (Wallace and Beavan, 2010; Wallace et al., 2012; Wallace and Eberhart-Phillips, 2013), the data and models we present here are from the first seafloor geodetic deployment to capture the distribution of SSEs beneath Hawke Bay. Improved resolution of the Hawke Bay SSE region provided by the offshore instrumentation indicates that SSE slip occurs between <3-15 km depth, revealing a nearly complete overlap with estimates of the source area of SSEs and prehistoric Great earthquakes offshore Hawkes Bay (Fig. 9).

Numerical modelling studies can reproduce scenarios where faults host both slow and fast rupture, due to large contrasts between effective stress in the slow slip and coseismic slip zones permitting the coseismic slip to extend into SSE areas (Lin et al., 2020; Ramos and Huang, 2019), dramatic fault weakening at high slip velocities (Di Toro et al., 2011; Tsutsumi et al., 2011), or arising from fault zone geometrical complexities (Romanet et al., 2018). There is observational evidence of SSE and seismic slip being hosted along the same portion of the Hawaiian décollement, where regularly recurring SSEs overlap spatially with the source area of the 2018 Mw 7.1 Hawaii earthquake (Lin et al., 2020). There are also intriguing suggestions of SSEs occurring before and potentially triggering large earthquakes, such as the 2011 Mw 9.0 Tohoku-Oki earthquake in Japan (Kato et al., 2012; Ito et al., 2013), the 2014 Mw 8.1 Iquique in Chile earthquake (Ruiz et al., 2014), and the 2014 Mw 7.3 Papanoa earthquake in Mexico (Radiguet et al., 2016), although it is not clear in these cases if regions undergoing SSE slip also slipped coseismically. Observations of coeval brittle and viscous deformation in exhumed subduction shear zones (Fagereng et al., 2019; Rowe et al., 2011), and evidence for coseismic shear heating from vitrinite reflectance and biomarker thermal maturity in near trench rocks where SSEs are also observed (Sakaguchi et al. 2011; Coffey et al., 2021) are also consistent with the possibility that shallow SSE regions can also undergo dynamic rupture.

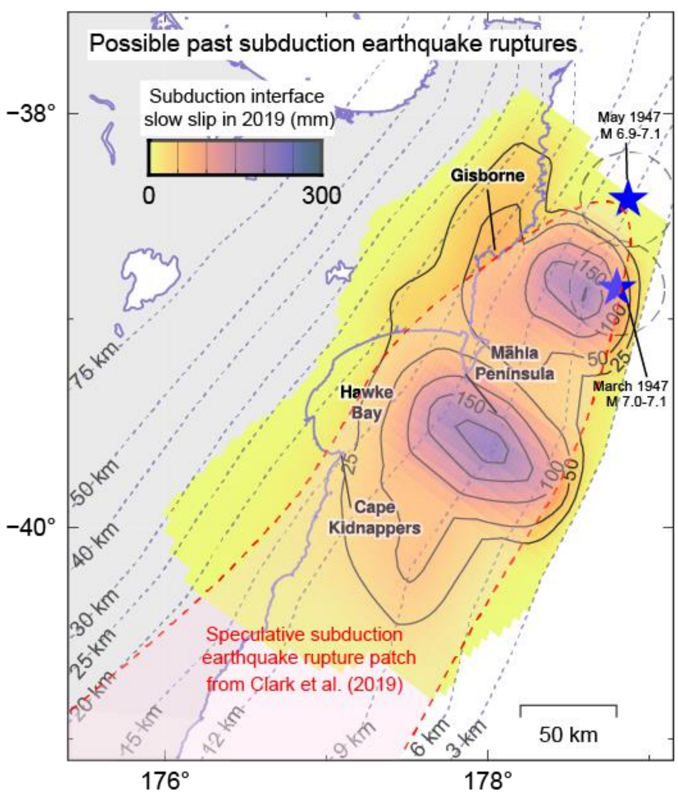

Figure 9: *Slip distribution of the 2019 SSEs (black contours, in millimetres) relative to the two 1947 tsunami earthquakes (blue stars with black dashes indicating the 25 km location uncertainty; Doser and Webb, 2003; Bell et al., 2014) and the speculative subduction zone earthquake rupture patch (outlined by red dashed lines) estimated by Clark et al. (2019). Grey dashes show the depth to the subduction interface, extracted from the geometry determined by Williams et al. (2013).*

Whether SSE regions are also prone to seismic rupture has important implications for our understanding of the temporal evolution of slip throughout multiple earthquake cycles at subduction zones, and for quantifying the seismic and tsunami hazard posed by subduction zones. Hazard models relying heavily on interseismic estimates of slip deficit rate (to define locations and rates of future ruptures) for subduction megathrusts may under-estimate the seismic and tsunami potential of regions dominated by SSEs and/or creep. Seismic slip could also penetrate into SSE regions, increasing the area, and therefore magnitude, of the rupture (Lin et al., 2020). We expect that this could be the case for the Hawkes Bay region, which is adjacent to the deeply coupled southern Hikurangi margin (Fig. 9; Wallace, 2020). It is plausible that ruptures initiated at southern Hikurangi could propagate into the Hawkes Bay region, with the large dynamic stress changes pushing the Hawke Bay SSE region to seismic failture. Indeed, Clark et al. (2019) identified possible paleoseismic evidence for possible ruptures spanning the southern and central segments of the Hikurangi subduction zone.

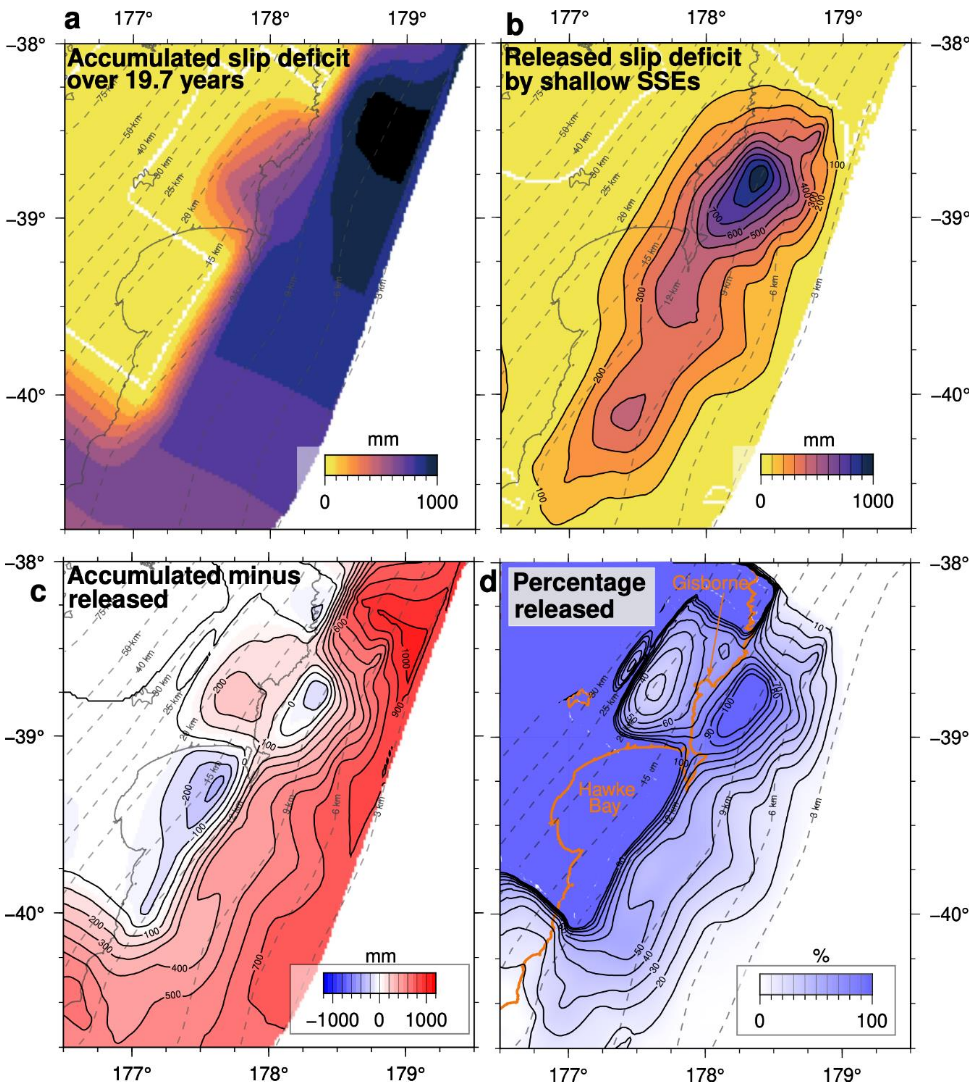

Figure 10: *Released slip deficit between April 2002 and March 2022. a) The accumulated slip deficit on the subduction interface in 19.7 years (April 2002 to March 2022 minus the large amplitude SSE periods - approximated as ∼10 weeks), based on the slip deficit rates accruing between slow slip events from Wallace and Beavan (2010). b) Released slip deficit by large SSEs from 2002 to March 2022 (summing the 2002–2014 SSE slip distribution of Wallace (2020), the 2014 Gisborne SSE slip distribution of Wallace et al. (2016), and the 2019 SSEs resolved in our study). c) The accumulated minus released slip deficit, where blue areas indicate SSEs have released more than has been accumulated in the ∼20 year period and red areas are where slip deficit remains. d) The percentage of slip deficit SSEs have released since April 2002. However, until the last several years, there were no seafloor geodetic constraints on the distrubtion of slip on the shallow plate boundary (<6-9 km depth), so the percentage of slip deficit released for the shallow interface (<9 km) may be severely underestimated on panels c and d.*

6.2. Contribution of shallow SSE slip to the plate motion budget at north and central Hikurangi

Understanding the role that SSEs play in the accommodation of the plate motion budget is required to address which proportion of the plate motion budget may be released seismically vs. aseismically. Comparing the 2019 SSE slip with the slip deficit being accumulated during the time between SSEs (e.g., during the "inter-SSE" period, from Wallace and Beavan, 2010) indicates that the 2019 Gisborne and Hawke Bay SSEs recovered up to 4-5 years of slip deficit (Figure 10d) in the regions of peak slow slip (~9 km depth). The largest Gisborne SSEs have occurred in 2004, 2010, 2014, and 2019 (every 4.5–5.5 years), with smaller SSEs occurring more frequently (at least every 2 years) in the period between the large SSEs.

With long-term convergence rates in the Gisborne region of 50 mm/yr and 40 mm/yr at the trench near Hawke Bay, we estimate that in the ~20 years between April 2002 to March 2022, that the shallow plate boundary may have accumulated up to 1 meter of slip deficit offshore Gisborne, and 0.8 meters offshore Hawkes Bay. The large shallow SSEs detected and modelled since April 2002 (see Wallace, 2020, and this study) have released 400–1000 mm of slip deficit offshore Gisborne and 100–500 mm beneath Hawke Bay (Figure 10b). Shallow SSEs immediately offshore Gisborne (at 9–12 km depth) appear to be releasing 70–100% of the slip deficit accumulated during the inter-SSE periods (Figures 10c and 10d), and 40-100% of total plate motion. Prior to 2014 there were no seafloor geodetic constraints for north and central Hikurangi SSEs, which could lead to an underestimate of slip on portions of the plate boundary >30 km offshore; thus, the total SSE slip accommodated over the last 20 years on the shallowest reaches of the plate boundary (<6-9 km depth) are likely underestimated and the remaining slip deficits should be considered a maximum. These calculations also don't include some of the smaller SSEs that may have occurred within the last ~20 years, and are another source of error that may produce an over-estimate of remaining slip deficit rate. Regardless, at least for the last decade, SSEs accommodate the majority of plate motion (and in some places 100% of the plate motion) at the offshore northern and central Hikurangi subduction margin.

6.3 Trenchward migration and longer duration of offshore slow slip events

Both the Gisborne and Hawke Bay SSEs suggest along-dip migration of the 2019 SSE (Figure 4). This migration is most notable in the Hawke Bay portion of the 2019 SSE sequence, with slip occurring at 9-12 km depth from late April to late May, with the locus of slip migrating up-dip to 6-9 km depth from late May to mid-July. The APG data are crucial to detect this up-dip migration of the SSEs, as the near trench (<6-9 km depth) phase of slip is not detectable with the onshore GNSS stations, since this is taking place 50-100 km offshore the Hawkes Bay coastline. Likewise, the time-dependent model of the 2014 Gisborne SSE estimated by Yohler et al. (2019) captured by the HOBITSS network also suggests that longer durations slip occurred near the trench, relative to the more rapid, earlier slip along the interface close to the coastline.

Observations of up-dip migration of SSEs at the shallow portions of subduction zones are far less common than observations of along-strike and along-dip migration of deep SSEs, primarily due to the lack of seafloor geodetic observations needed to detect the offshore (up-dip) SSE slip evolution. However, pore pressure changes (as a proxy for volumetric strain) detected by transects of IODP CORK observatories at the shallow portions of Nankai Trough (Araki et al., 2017; Ariyoshi et al., 2021) and Costa Rica (Davis et al., 2015) subduction margins suggest up-dip migration may in fact be a common feature of shallow SSEs. The migration of an SSE inferred by Araki et al. (2017) at the Nankai Trough has estimated up-dip propagation velocities of ~0.5 km/day, based on the 11 km spacing (along-dip) of borehole observatories and their approximated migration period of 3 weeks. Davis et al. (2015) estimate up-dip propagation rates of ~5 km/day for an offshore Costa Rica SSE. If a patch of slow slip did migrate from the interface beneath Hawke Bay to the near-trench portion of the interface, then we estimate from our geodetic model that this could have occurred over the 1–3 weeks from mid-May (Figure 4), with potential propagation velocities of 1–6 km/day (based on a 20–40 km up-dip change in the location of the SSE slip), comparable to the Nankai and Costa Rica examples.

The near-trench slip occurring during the last month of the 2019 East Coast SSE offshore Hawkes Bay was not clearly detectable using onshore GNSS data, although the seafloor pressure data indicate that the event persisted for at least another month (well into July). This implies that using onshore GNSS data alone to estimate the duration of shallow SSEs like those in New Zealand (Wallace, 2020 and references therein), Costa Rica (Dixon et al., 2014), Ecuador (Vallee et al., 2013) and elsewhere may underestimate the duration of shallow SSEs by as much as 50%. This has important implications for shallow SSE duration estimates used in establishing Moment-duration scaling relationships (e.g., Ide et al., 2007). The nature of Moment-duration scaling relationships of SSEs has important implications for whether SSEs and earthquakes arise from the same fundamental process, and there has been much controversy about this topic with many studies obtaining results with very different implications (e.g., Ide et al., 2007; Gomberg et al., 2016; Frank and Brodsky, 2019; Michel et al., 2019; Dal Zillio et al., 2020). The much longer duration of Hawke Bay SSEs than expected using only onshore GNSS indicates that the moments and durations of offshore shallow SSEs must be utilized with care in establishing such relationships, as the duration (and to some extent, the magnitude) may be severely underestimated due to observational limitations.

7 Conclusions

Using onshore continuous GNSS data, InSAR LOS displacements, and seafloor pressure as a proxy for the vertical deformation of the seafloor, we model the spatiotemporal evolution of shallow, <15 km depth, SSEs at the northern and central Hikurangi subduction zone taking place between February 2019 and July 2019. Peaks of 150–200 mm and >200 mm total slip are estimated offshore Gisborne (at 6–9 km depth) and beneath Hawke Bay (at 9–12 km depth) respectively (releasing 4-5 years of slip deficit). Insight into the vertical seafloor deformation in these regions, from seafloor pressure sensors, indicates that the slow slip may have persisted on the shallow plate interface longer than indicated by onshore GNSS stations. Seafloor pressure data from sites offshore central Hikurangi (Hawkes Bay) reveal up-dip migration of the SSE occurred over a few weeks beneath Hawke Bay, which is too far offshore to be resolvable by the GNSS network. This indicates that shallow SSEs may last longer (several weeks or more) than is detectable by coastal GNSS networks—this has important implications for our ability to robustly characterize offshore SSE durations in the absence of seafloor geodetic data. We identify overlapping source regions between the 2019 east coast SSE sequence and locations of the March Mw 7.0–7.1 1947 tsunami earthquake offshore Gisborne and past megathrust earthquake rupture beneath Hawke Bay inferred from paleoseismic investigations. This raises the need to include SSE regions in potential earthquake and tsunami sources in hazard models at subduction zones. Denser seafloor geodetic monitoring of the shallow margin is essential to better resolving the spatio-temporal evolution of offshore slip and improving our understanding of shallow subduction processes and how the present-day SSEs interact with regional seismicity and influence the potential of future seismic megathrust ruptures.

Acknowledgments

This research was supported by funding to GNS Science from New Zealand's Ministry of Business, Innovation and Employment's Endeavour Research Fund (contract CO5X1605), funding by NSF to SCW (Grant number OCE-1754929), and Japanese Government funding to Univ. Tokyo, Kyoto University and Tokyo University. To our knowledge there are no real or perceived financial conflicts of interest for any author. We thank the Captain and crew of the R/V Tangaroa without whom this work would not have been possible.

Open Research

Seafloor pressure data used in this study (published in Woods et al., 2022) are publicly available at https://doi.org/10.5281/zenodo.5834879. The GeoNet GNSS timeseries data are available from www.geonet.org.nz.. The InSAR Line-of-Sight change data used in the modeling is included in the supplementary material of this manuscript. The modeling software utilized in this research (TDEFNODE) is publicly available at https://robmccaffrey.github.io/TDEFNODE/TDEFNODE.html. All figures were generated using Generic Mapping Tools (GMT 6; Wessel et al., 2013).

References

Aagaard, B., Knepley, M., and Williams, C. (2017a). PyLith v2.2.1, Computational Infrastructure for Geodynamics. https://doi.org/10.5281/ zenodo.886600, Retrieved from https://geodynamics.org/cig/software/pylith/

Aagaard, B., Knepley, M., and Williams, C. (2017b). PyLith user manual, version 2.2.0, Computational Infrastructure for Geodynamics, Davis, CA. Retrieved from https://geodynamics.org/cig/software/github/pylith/v2.2.0/pylith-2.2.0_manual.pdf

Aagaard, B. T., Knepley, M. G., and Williams, C. A. (2013). A domain decomposition approach to implementing fault slip in finite-element models of quasi-static and dynamic crustal deformation. *Journal of Geophysical Research Solid Earth*, *118*, 3059–3079. https://doi.org/10.1002/ jgrb.50217

Araki, E., Saffer, D. M., Kopf, A. J., Wallace, L. M., Kimura, T., Machida, Y., Ide, S., Davis, E., and IODP Expedition 365 shipboard scientists (2017). Recurring and triggered slow-slip events near the trench at the Nankai Trough subduction megathrust. Science, 356:1157–1160.

Ariyoshi, K., Iinuma, T., Nakano, M., Kimura, T., Araki, E., Machida, Y., Sueki, K., Yada, S., Nishiyama, T., Suzuki, K., Hori, T., Takahashi, N., and Kodaira, S. (2021). Characteristics of Slow Slip Event in March 2020 Revealed From Borehole and DONET Observatories. Frontiers in Earth Science, 8.

Barker, D., Wallace, L., Woods, K., Savage, M., and TAN1809 Science Party (2019). Hikurangi Ocean Bottom Investigation of Tremor and Slow Slip (HOBITSS V). Technical report, GNS Science, Lower Hutt, NZ.

Bartlow, N.M., Miyazaki, S.I., Bradley, A.M. and Segall, P., 2011. Space-time correlation of slip and tremor during the 2009 Cascadia slow slip event. *Geophysical Research Letters*, *38*(18).

Beavan, J., Tregoning, P., Bevis, M., Kato, T. and Meertens, C., 2002. Motion and rigidity of the Pacific Plate and implications for plate boundary deformation. *Journal of Geophysical Research: Solid Earth*, *107*(B10), pp.ETG-19.

Bell, R., C. Holden, W. Power, X. Wang, and G. Downes, Hikurangi margin tsunami earthquake generated by slow seismic rupture over a subducted seamount, Earth and Planet. Sci. Lett., 397, 1-9, 2014.

Bürgmann, R. and Chadwell, D. (2014). Seafloor Geodesy. Annu. Rev. Earth Planet. Sci, 42:509–534.

Clark, K., Howarth, J., Litchfield, N., Cochran, U. A., Turnball, J., Dowling, L., Howell, A., Berryman, K., and Wolfe, F. (2019). Geological evidence for past large earthquakes and tsunamis along the Hikurangi subduction margin, NewZealand. Marine Geology, 412:139–172.

Cochran, U., Berryman, K., Zachariasen, J., Mildenhall, D., Hayward, B., Southall, K., Hollis, C., Barker, P., Wallace, L., Alloway, B., and Wilson, K. (2006). Paleoecolog- ical insights into subduction zone earthquake occurrence, eastern North Island, New Zealand. Bulletin of the Geological Society of America, 118(9–10):1051–1074.

Coffey, G.L., Savage, H.M., Polissar, P.J., Meneghini, F., Ikari, M.J., Fagereng, Å., Morgan, J.K., and Wang, M., 2021, Evidence of seismic slip on a large splay fault in the Hikurangi subduction zone: Geochemistry, Geophysics, Geosystems, v. 22, no. 8, https://doi .org /10 .1029 /2021GC009638.

Cummings, J. A. (2006). Operational multivariate ocean data assimilation. Quarterly Journal of the Royal Meteorological Society, 131(613).

Cummings, J. A. and Smedstad, O. M. (2013). Variational data assimilation for the global ocean. In Data Assimilation for Atmospheric, Oceanic and Hydrologic Applications (Vol. II).

Dal Zilio, L., Lapusta, N. and Avouac, J.P., 2020. Unraveling scaling properties of slow-slip events. *Geophysical Research Letters*, *47*(10), p.e2020GL087477.

Davis, E. E., Villinger, H., and Sun, T. (2015). Slow and delayed deformation and uplift of the outermost subduction prism following ETS and seismogenic slip events beneath Nicoya Peninsula, Costa Rica. Earth and Planetary Science Letters.

Delahaye, E. J., Townend, J., Reyners, M. E., and Rogers, G. (2009). Microseismicity but no tremor accompanying slow slip in the Hikurangi subduction zone, New Zealand. Earth and Planetary Science Letters, 277(1-2):21–28.

Di Toro, G., R. Han, T. Hirose, N. De Paola, S. Nielsen, K. Mizoguchi, F. Ferri, M. Cocco, and T. Shimamoto (2011), Fault lubrication during earthquakes, *Nature*, **471**, 494–498, doi:10.1038/nature09838.

Doser, D. I. and Webb, T. H. (2003). Source parameters of large historical (1917–1961) earthquakes, North Island, New Zealand. Geophysical Journal Interna- tional, 152(3):795–832.

Downes, G., T.H. Webb, M.J. McSaveney, C. Chague-Goff, D.J. Darby, and A. Barnett (2000), The March 25 and May 17 1947 Gisborne earthquakes and tsunami: Implication for tsunami hazard for East Coast, North Island, New Zealand, in *Tsunami Risk Assessment Beyond 2000: Theory, Practice and Plans*, Proceedings of Joint IOC–IUGG International Workshop, V.K. Gusiakov, B.W. Levin, and O.I. Yakovenko, eds, Moscow, pp. 55-67.

Eberhart-Philips, D. and Bannister, S. (2015). 3-D imaging of the northern Hikurangi subduction zone, New Zealand: variations in subducted sediment, slab fluids and slow slip. Geophysical Journal International, 201:838–855.

Eberhart-Phillips, D. and Reyners, M. (2012). Imaging the Hikurangi Plate interface region, with improved local-earthquake tomography. Geophysical Journal International, 190(2):1221–1242.

Eberhart-Phillips, D., Reyners, M., Bannister, S., Chadwick, M., and Ellis, S. (2010). Establishing a versatile 3-D seismic velocity model for New Zealand. Seismological Research Letters, 81(6).

Fagereng, Å., et al., 2019, Mixed deformation styles observed on a shallow subduction thrust, Hikurangi margin, New Zealand, Geology, doi .org /10 .1130 /G46367.1

Frank, W.B. and Brodsky, E.E., 2019. Daily measurement of slow slip from low-frequency earthquakes is consistent with ordinary earthquake scaling. *Science advances*, *5*(10), p.eaaw9386.

Fredrickson, E. K., Wilcock, W. S., Schmidt, D. A., MacCready, P., Roland, E., Kurapov, A. L., Zumberge, M. A., and Sasagawa, G. S. (2019). Optimizing Sensor Configurations for the Detection of Slow-Slip Earthquakes in Seafloor Pressure Records, Using the Cascadia Subduction Zone as a Case Study. Journal of Geophysical Research: Solid Earth.

Gagnon, K., C. D. Chadwell, and E. Norabuena Measuring the onset of locking in the Peru-Chile trench with GPS and acoustic measurements, *Nature*, 434(7030), 205-208,.doi: 10.1038/nature03412,2005.

Gomberg, J., Wech, A., Creager, K., Obara, K. and Agnew, D., 2016. Reconsidering earthquake scaling. *Geophysical Research Letters*, *43*(12), pp.6243-6251.

Hamling, I. J., Wright, T. J., Hreinsdöttir, S., and Wallace, L. M. (2022). A Snapshot of New Zealand's Dynamic Deformation Field From Envisat InSAR and GNSS Observa- tions Between 2003 and 2011. Geophysical Research Letters, 49(2).

Hayward, B. W., Sabaa, A. T., Grenfell, H. R., Cochran, U. A., Clark, K. J., Litchfield, N. J., Wallace, L., Marden, M., and Palmer, A. S. (2015). Foraminiferal record of Holocene paleo-earthquakes on the subsiding south-western Poverty Bay coastline, New Zealand. New Zealand Journal of Geology and Geophysics, 58(2).

Helber, R. W., Townsend, T. L., Barron, C. N., Dastugue, J. M., and Carnes, M. R. (2013). Validation Test Report for the Improved Synthetic Ocean Profile (ISOP) System, Part I: Synthetic Profile Methods and Algorithm. Technical report, Naval Research Lab Stennis Detachment Stennis Space Center MS Oceanography Div.

Hooper, A. J. (2008). A multi-temporal InSAR method incorporating both persistent scatterer and small baseline approaches. Geophysical Research Letters, 35(16).

Hooper, A., Bekaert, D., Spaans, K., and Arikan, M. (2012). Recent advances in SAR interferometry time series analysis for measuring crustal deformation. Tectonophysics, 514–517:1–13.

Ide, S., Beroza, G.C., Shelly, D.R. and Uchide, T., 2007. A scaling law for slow earthquakes. *Nature*, *447*(7140), pp.76-79.

Im, K., Saffer, D., Marone, C. and Avouac, J.P., 2020. Slip-rate-dependent friction as a universal mechanism for slow slip events. *Nature Geoscience*, *13*(10), pp.705-710.

Inoue, T., Ito, Y., Wallace, L. M., Yoshikawa, Y., Inazu, D., Garcia, E. S. M., Muramoto, T., Webb, S. C., Ohta, K., Suzuki, S., and Hino, R. (2021). Water depth dependence of long-range correlation in nontidal variations in seafloor pressure. Geophysical Research Letters.

Ito, Y., Hino, R., Kido, M., Fujimoto, H., Osada, Y., Inazu, D., Ohta, Y., Iinuma, T., Ohzono, M., Miura, S., Mishina, M., Suzuki, K., Tsuji, T., and Ashi, J. (2013). Episodic slow slip events in the Japan subduction zone before the 2011 Tohoku-Oki earthquake. Tectonophysics.

Kato, A., Obara, K., Igarashi, T., Tsuruoka, H., Nakagawa, S., and Hirata, N. (2012). Propagation of Slow Slip Leading Up to the 2011 M w 9.0 Tohoku-Oki Earthquake. Science, 335:705–708.

Koulali, A., McClusky, S., Wallace, L. M., Allgeyer, S., Tregoning, P., D'Anastasio, E., and Benavente, R. (2017). Slow slip events and the 2016 Te Araroa M w 7.1 earth- quake interaction: Northern Hikurangi subduction, New Zealand. Geophysical Research Letters, 44:8336–8344.

Leeman, J.R., Saffer, D.M., Scuderi, M.M. and Marone, C., 2016. Laboratory observations of slow earthquakes and the spectrum of tectonic fault slip modes. *Nature communications*, *7*(1), p.11104.

Lellouche, J.-M., Greiner, E., Bourdallé-Badie, R., Garric, G., Melet, A., Drévillon, M., Bricaud, C., Hamon, M., Le Galloudec, O., Regnier, C., Candela, T., Testut, C.-E., Gasparin, F., Ruggiero, G., Benkiran, M., Drillet, Y., and Le Traon, P.-Y. (2021). The Copernicus Global 1/12° Oceanic and Sea Ice GLORYS12 Reanalysis. Frontiers in Earth Science, 9.

Lin, J. T., Aslam, K. S., Thomas, A. M., and Melgar, D. (2020). Overlapping regions of coseismic and transient slow slip on the Hawaiian decollement. Earth and Planetary Science Letters, 544.

Liu, Y. and Rice, J.R., 2007. Spontaneous and triggered aseismic deformation transients in a subduction fault model. *Journal of Geophysical Research: Solid Earth*, *112*(B9).

McCaffrey, R. (2009). Time-dependent inversion of three-component continuous GPS for steady and transient sources in northern Cascadia. Geophysical Research Letters, 36(L07304).

Menemenlis, D., Campin, J.-M., Heimbach, P., Hill, C. N., Lee, T., Nguyen, A. T., Schodlok, M. P., and Zhang, H. (2008). ECCO2: High resolution global ocean and sea ice data synthesis. Mercator Ocean Quarterly Newsletter, 31(October).

Michel, S., Gualandi, A. and Avouac, J.P., 2019. Similar scaling laws for earthquakes and Cascadia slow-slip events. *Nature*, *574*(7779), pp.522-526.

Miyazaki, S.I., Segall, P., McGuire, J.J., Kato, T. and Hatanaka, Y., 2006. Spatial and temporal evolution of stress and slip rate during the 2000 Tokai slow earthquake. *Journal of Geophysical Research: Solid Earth*, *111*(B3).

Petersen, M. D., Shumway, A. M., Powers, P. M., Mueller, C. S., Moschetti, M. P., Frankel, A. D., et al. (2020). The 2018 update of the US national seismic hazard model: Overview of model and implications. *Earthquake Spectra*, **36**(1), 5–41. https://doi.org/10.1177/8755293019878199

Pizer, C., K. Clark, J. Howarth, A. Howell, J. Delano, B. W. Hayward, N. Litchfield; A 5000 yr record of coastal uplift and subsidence reveals multiple source faults for past earthquakes on the central Hikurangi margin, New Zealand. *GSA Bulletin* 2023; doi: https://doi.org/10.1130/B36995.1

Polster, A., Fabian, M. and Villinger, H., 2009. Effective resolution and drift of Paroscientific pressure sensors derived from long-term seafloor measurements. *Geochemistry, Geophysics, Geosystems*, *10*(8).

Radiguet, M., Perfettini, H., Cotte, N., Gualandi, A., Valette, B., Kostoglodov, V., Lhomme, T., Walpersdorf, A., Cabral Cano, E., and Campillo, M. (2016). Triggering of the 2014 Mw 7.3 Papanoa earthquake by a slow slip event in Guerrero, Mexico. Nature Geoscience, 9(11):829–833.

Ramos, M. D. and Huang, Y. (2019). How the Transition Region Along the Cascadia Megathrust Influences Coseismic Behavior: Insights From 2-D Dynamic Rupture Simulations. Geophysical Research Letters.

Reyners, M., Eberhart-Phillips, D., and Martin, S. (2014). Prolonged canterbury earth- quake sequence linked to widespread weakening of strong crust. Nature Geoscience, 7(1).

Romanet, P. and Ide, S. (2019). Ambient tectonic tremors in Manawatu, Cape Turnagain, Marlborough, and Puysegur, New Zealand. Earth, Planets and Space, 71(1).

Rowe, C.D., Meneghini, F., and Moore, J.C., 2011, Textural record of the seismic cycle: Strain-rate variation in an ancient subduction thrust, *in* Fagereng, Å., et al., eds., Geology of the Earthquake Source: A Volume in Honour of Rick Sibson: Geological Society [London] Special Publication 359, p. 77–95, https:// doi .org /10 .1144 /SP359 .5 .

Ruiz, S., Metois, M., Fuenzalida, A., Ruiz, J., Leyton, F., Grandin, R., Vigny, C., Madariaga, R., and Campos, J. (2014). Intense foreshocks and a slow slip event pre- ceded the 2014 Iquique Mw8.1 earthquake. Science, 345(6201):1165–1169.

Sakaguchi, A., Chester, F., Curewitz, D., Fabbri, O., Goldsby, D., Kimura, G., Li, C.F., Masaki, Y., Screaton, E.J., Tsutsumi, A. and Ujiie, K., 2011. Seismic slip propagation to the updip end of plate boundary subduction interface faults: Vitrinite reflectance geothermometry on Integrated Ocean Drilling Program NanTro SEIZE cores. *Geology*, *39*(4), pp.395-398.

Segall, P., Rubin, A.M., Bradley, A.M. and Rice, J.R., 2010. Dilatant strengthening as a mechanism for slow slip events. *Journal of Geophysical Research: Solid Earth*, *115*(B12).

Shreedharan, S., Saffer, D., L.M. Wallace, and C. Williams, 2023, Ultralow frictional healing explains recurring slow slip events, Science, 379(6633), 712-717.

Tadono, T., Ishida, H., Oda, F., Naito, S., Minakawa, K., and Iwamoto, H. (2014). Precise Global DEM Generation by ALOS PRISM. ISPRS Annals of the Photogrammetry, Remote Sensing and Spatial Information Sciences, II-4.

Tadono, T., Nagai, H., Ishida, H., Ode, F., Naito, S., Minakawa, K., and Iwamoto, H. (2016). Initial Validation of the 30 m-mesh Global Digital Surface Model Generated by ALOS PRISM. The International Archives of the Photogrammetry, Remote Sensing and Spatial Information Sciences, ISPRS, XLI(B4):157–162.

Takaku, J. and Tadono, T. (2017). Quality updates of 'AW3D' global DSM generated from ALOS PRISM. In International Geoscience and Remote Sensing Symposium (IGARSS), volume July-2017.

Takaku, J., Tadono, T., and Tsutsui, K. (2014). Generation of high resolution global DSM from ALOS PRISM. In International Archives of the Photogrammetry, Remote Sensing and Spatial Information Sciences - ISPRS Archives, volume 40.

Takaku, J., Tadono, T., Doutsu, M., Ohgushi, F., and Kai, H. (2020). Updates of aw3d30' alos global digital surface model with other open access datasets. In International Archives of the Photogrammetry, Remote Sensing and Spatial Information Sciences - ISPRS Archives, volume 43.

Takaku, J., Tadono, T., Tsutsui, K., and Ichikawa, M. (2016). Validation of "AW3D" global DSM generated from ALOS prism. ISPRS Annals of Photogrammetry, Remote Sensing and Spatial Information Sciences, III-4.

Takaku, J., Tadono, T., Tsutsui, K., and Ichikawa, M. (2018). Quality improvements of 'AW3D' global DSM derived from ALOS PRISM. In International Geoscience and Remote Sensing Symposium (IGARSS), volume 2018-July.

Tsutsumi, A., Fabbri, O., Karpoff, A. M., Ujiie, K., and Tsujimoto, A. (2011). Friction velocity dependence of clay-rich fault material along a megasplay fault in the Nankai subduction zone at intermediate to high velocities. Geophysical Research Letters, 38(19).

Urlaub, M., Petersen, F., Gross, F., Bonforte, A., Puglisi, G., Guglielmino, F., Krastel, S., Lange, D. and Kopp, H., 2018. Gravitational collapse of Mount Etna's southeastern flank. *Science Advances*, *4*(10), p.eaat9700.

Vallée, M., Nocquet, J.M., Battaglia, J., Font, Y., Segovia, M., Régnier, M., Mothes, P., Jarrin, P., Cisneros, D., Vaca, S. and Yepes, H., 2013. Intense interface seismicity triggered by a shallow slow slip event in the Central Ecuador subduction zone. *Journal of Geophysical Research: Solid Earth*, *118*(6), pp.2965-2981.

Wallace, L. M. (2020). Slow Slip Events in New Zealand. Annual Review of Earth and Planetary Sciences, 48:175–203.

Wallace, L. M. and Beavan, J. (2010). Diverse slow slip behavior at the Hikurangi subduction margin, New Zealand. Journal of Geophysical Research: Solid Earth, 115(B12402).

Wallace, L. M. and Eberhart-Philips, D. (2013). Newly observed, deep slow slip events at the central Hikurangi margin, New Zealand: Implications for downdip variability of slow slip and tremor, and relationship to seismic structure. Geophysical Research Letters, 40:5393–5398.

Wallace, L. M., Barnes, P., Beavan, J., Van Dissen, R., Litchfield, N., Mountjoy, J., Langridge, R., Lamarche, G., and Pondard, N. (2012a). The kinematics of a transition from subduction to strike-slip: An example from the central New Zealand plate boundary. Journal of Geophysical Research: Solid Earth, 117(B2).

Wallace, L. M., Beavan, J., Bannister, S., and Williams, C. (2012b). Simultaneous long-term and short-term slow slip events at the Hikurangi subduction margin, New Zealand: Implications for processes that control slow slip event occurrence, duration, and migration. Journal of Geophysical Research, 117(B11402).

Wallace, L. M., Beavan, J., McCaffrey, R., and Darby, D. (2004). Subduction zone coupling and tectonic block rotations in the North Island, New Zealand. Journal of Geophysical Research: Solid Earth, 109(B12).

Wallace, L. M., Kaneko, Y., Hreinsdóttir, S., Hamling, I., Peng, Z., Bartlow, N., D'Anastasio, E., and Fry, B. (2017). Large-scale dynamic triggering of shallow slow slip enhanced by overlying sedimentary wedge. Nature Geoscience, 10:765–770.

Wallace, L. M., Webb, S. C., Ito, Y., Mochizuki, K., Hino, R., Henrys, S., Schwartz, S. Y., and Sheehan, A. F. (2016). Slow slip near the trench at the Hikurangi subduction zone, New Zealand. Science, 352(6286):701–704.

Wallace, L.M., Saffer, D.M., Barnes, P.M., Pecher, I.A., Petronotis, K.E., LeVay, L.J., and the Expedition 372/375 Scientists, 2019. *Hikurangi Subduction Margin Coring, Logging, and Observatories*. Proceedings of the International Ocean Discovery Program, 372B/375: College Station, TX (International Ocean Discovery Program). https://doi.org/10.14379/iodp.proc.372B375.2019

Werner, C., Wegmüller, U., Strozzi, T., and Wiesmann, A. (2000). GAMMA SAR and interferometric processing software. In European Space Agency, (Special Publication) ESA SP, number 461.

Wilcock, W. S. D., Manalang, D. A., Fredrickson, E. K., Harrington, M. J., Cram, G., Tilley, J., Burnett, J., Martin, D., Kobayashi, T., and Paros, J. M. (2021). A Thirty- Month Seafloor Test of the A-0-A Method for Calibrating Pressure Gauges. Frontiers in Earth Science, 8.

Williams, C. A. and Wallace, L. M. (2015). Effects of material property variations on slip estimates for subduction interface slow-slip events. Geophysical Research Letters, 42:1113–1121.

Williams, C. A. and Wallace, L. M. (2018). The Impact of Realistic Elastic Properties on Inversions of Shallow Subduction Interface Slow Slip Events Using Seafloor Geodetic Data. Geophysical Research Letters, 45:1–9.

Williams, C. A., Eberhart-Phillips, D., Bannister, S., Barker, D. H. N., Henrys, S., Reyners, M., and Sutherland, R. (2013). Revised Interface Geometry for the Hikurangi Subduction Zone, New Zealand. Seismological Research Letters, 84(6):1066–1073.

Wong I, Kulkarni R, Zachariasen J, Lawrence M, Hanson K, Clague J, Ostenaa D, Youngs R, LaForge R, McCann M. Characterising the Cascadia Subduction Zone for Seismic Hazard Assessments. Proceedings of the 10th National Conference on Earthquake Engineering, Earthquake Engineering Research Institute, Anchorage, AK, 2014.

Woods, K., S. Webb, L. M. Wallace Y Ito, C Collins, N Palmer, R Hino, MK Savage, DM Saffer, EE Davis, DHN Barker, 2022, Using sealoor geodesy to detect vertical deformation at the Hikurangi subduction zone: Insights from self-calibrating pressure sensors and ocean general circulation models, J. Geophys. Res., https://doi.org/10.1029/2022JB023989

Yohler, R., Bartlow, N., Wallace, L. M., and Williams, C. (2019). Time-Dependent Behav- ior of a Near-Trench Slow-Slip Event at the Hikurangi Subduction Zone. Geochemistry, Geophysics, Geosystems, 20(8).

Yokota, Y. and Ishikawa, T. (2020). Shallow slow slip events along the Nankai Trough detected by GNSS-A. Science Advances, 6(3).

Supplementary Material

1.0 Spatial resolution tests for our slip inversions

To test the spatial resolution enabled by our onshore and offshore instrument coverage, we undertake checkerboard tests using the TDEFNODE parameterization that inverts for slip at nodes, rather than slip sources defined by elliptical basis functions. We generate three checkerboard slip patterns (Figure S1a, 1f, 1k) with nodes of 250/150/50 mm alternating with nodes of 0 mm slip and forward model the theoretical displacements at instrument locations (both onshore and offshore). The three checkerboards alternate slip values every node along-strike and every second node in the down-dip direction (Figures S1), which is analogous to the size of slip patches we are interested in resolving at the Gisborne and Hawke's Bay SSE regions. We add Gaussian distributed random noise with uncertainties consistent with what is expected of the respective geodetic displacement components (horizontal, vertical, and LOS displacements) for each data type; this random noise is added to the forward model displacements prior to the inversions for the checkerboard test. We then invert the forward model surface displacement field (with random noise added) at each of the nodes to assess how much of the checkerboard can be recovered. For each checkerboard, we conduct tests for cases with only onshore geodetic data (continuous GNSS and InSAR displacements; Figures S1b, 1g, 1l), and cases with both onshore and offshore geodetic data (continuous GNSS, InSAR, and seafloor vertical displacements from pressure data; Figures S1c, 1h, 1m), to assess changes in spatial resolution provided by the seafloor geodetic data.

The apparent greater resolution offshore of Hawke Bay (compared to offshore Gisborne) is due to the larger spacing between fault nodes here (e.g., coarser checkers). We utilize the checkerboard tests to estimate the spatial resolution contours of the final model presented in Figure 2 (see red and blue dashed lines).

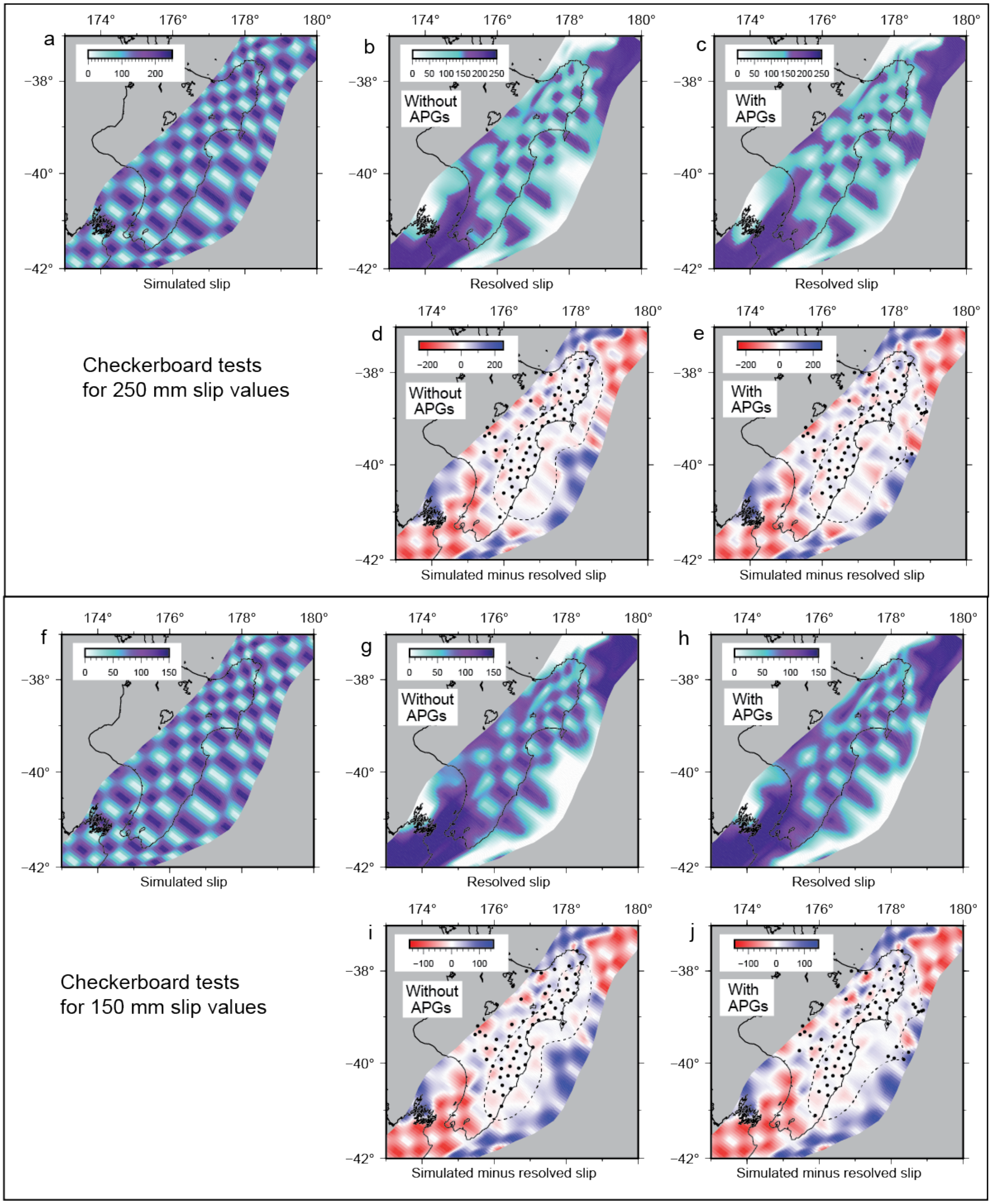
a
b
c
Without APGs
With APGs
Simulated slip
Resolved slip
Resolved slip
d
e
Without APGs
With APGs
Simulated minus resolved slip
Simulated minus resolved slip
Checkerboard tests for 250 mm slip values
f
g
h
Without APGs
With APGs
Simulated slip
Resolved slip
Resolved slip
i
j
Without APGs
With APGs
Simulated minus resolved slip
Simulated minus resolved slip
Checkerboard tests for 150 mm slip values
174°
176°
178°
180°
−38°
−40°
−42°

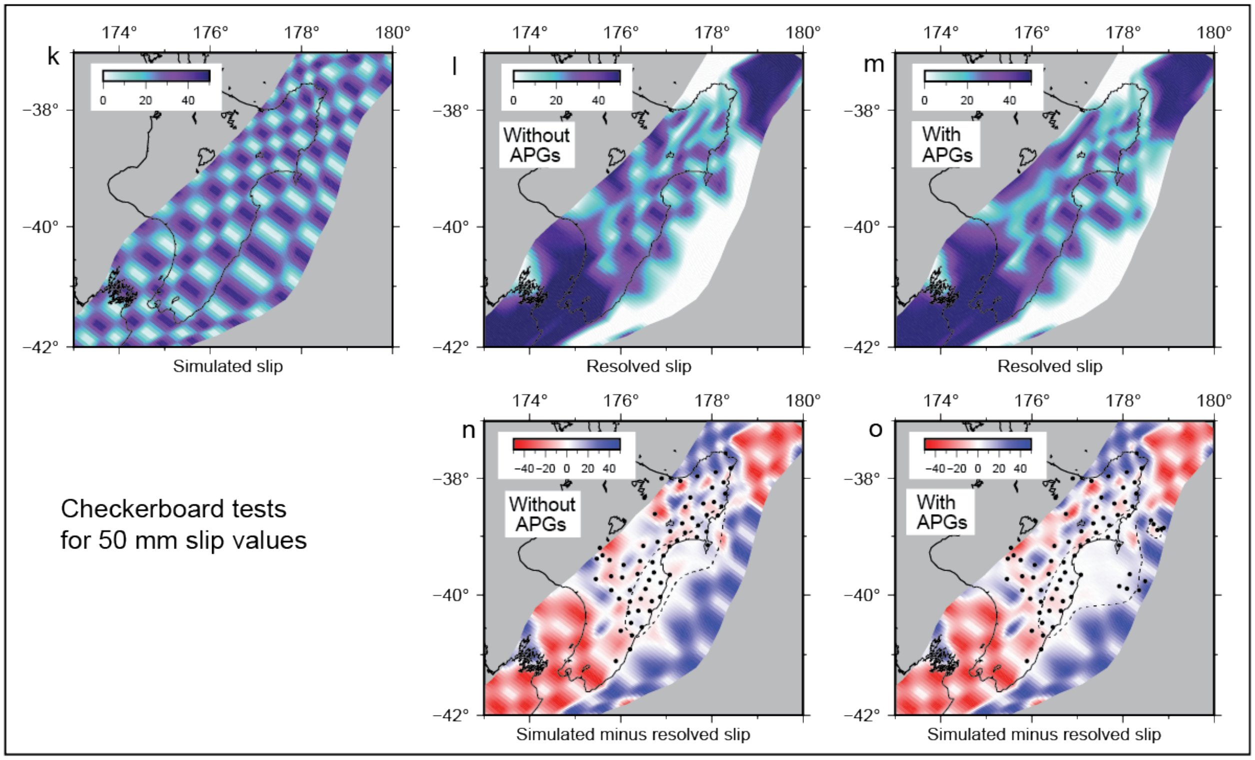

Figure S1: Checkerboard test results for 250 mm slip scenario (a-e), 150 mm (f-j), and 50 mm slip (k-o). Forward model slip distributions (with alternating nodes of slip and no slip) are shown in (a) 250 mm slip (f) 150 mm slip, and (k) 50 mm slip. Sites used in the test are shown as a block dot. Resolved slip using theoretical displacements (with noise added) from only onshore (continuous GNSS) instrumentation (b) 250 mm, (g) 150 mm, and (l) 50 mm. Resolved slip using both onshore and offshore instrumentation; (c) 250 mm, (h) 150 mm, (m) 50 mm. Panels (d), (i) and (n) show Forward model slip (a,f,k) minus resolved slip checkerboards (b,g,l) for inversions with only onshore data, with dashes indicating the estimated area of resolvable slip. Forward model slip (a,f,k) minus resolved slip checkerboards (c,h,m) for inversions using both onshore and offshore data.

2.0: Additional details of the Inversion set-up, data used, and results

We outline most of the details of the TDefnode model set-up and inversion in the main text, although we present some additional details here. Figure S2 shows the block boundary geometries, subduction interface nodes, and onshore and offshore geodetic stations used in this study, as well as data duration.

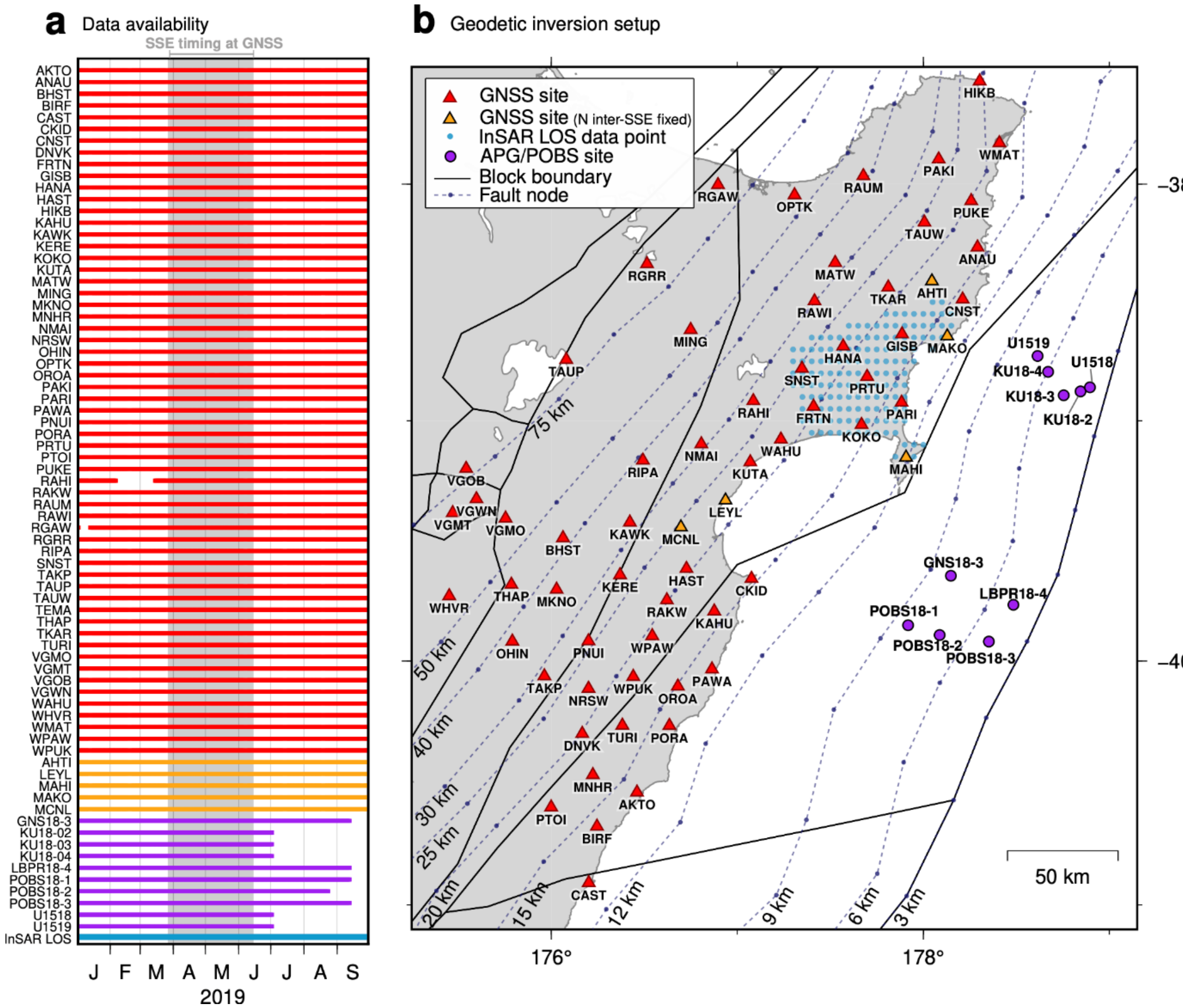

Figure S2: The TDEFNODE inversion framework for the inversion of geodetic data, and data timeframes used. a) Data timeframes used for the GNSS, seafloor pressure, and InSAR LOS data. Orange GNSS data have the north component inter-SSE rates fixed to the rates calculated by Wallace et al. (2012a), whereas these are resolved for the red GNSS data. b) Block model boundaries (Wallace et al., 2004, 2012a) are indicated by solid black lines, and the prescribed Hikurangi interface is shown by nodes (dark blue circles with dashed lines connecting nodes along the same depth contour, extracted from the geometry determined by Williams et al. (2013)). The locations of the GNSS, InSAR, and seafloor data points used in this study are overlain as red/orange triangles, light blue circles, and purple circles respectively.

To invert the seafloor vertical displacement time series with TDEFNODE, the data have to be treated like three component GNSS data, meaning an east and north component is required. To satisfy this, we set the east and north components of the seafloor time series to randomly generated data of uniformly distributed numbers in the interval from -500 mm to 500 mm. The east and north components are then given uncertainties of 499 mm. The large uncertainties means the inversion ignores the simulated data (no influence on the resolved model relative to the real data), and the wide range of east and north displacement values prevents the simulated data from acting as a restriction to the possible seafloor vertical displacement values.

In total the inversion contains 64,707 data points: 51,513 GNSS positions, 144 InSAR LOS points, and 13,050 seafloor vertical displacement points (8,700 simulated and 4,350 real). The data are weighted to account for the different number of data points, with the seafloor pressure time series and InSAR LOS displacements weighted four and 20 times more than the GNSS time series respectively. Due to the circular nature of the interferogram generation, (involving predicted SSE displacements), the InSAR data are not weighted high enough to be a controlling dataset for the resolved slip near Gisborne.

Source number	Parameter type	Minimum	Maximum
1	Longitude	177.9	178.7
1	Latitude	-39.1	-38.8
1	Down-dip width	3	55
1	Along-strike width	3	55
1	Origin Time	2019.18	2019.25
1	Time constant	0.5	3.2
2	Longitude	177.9	178.7
2	Latitude	-38.5	-38.1
2	Down-dip width	5	25
2	Along-strike width	5	25
2	Origin Time	2019.18	2019.25
2	Time constant	5	12
3	Longitude	177	178.4
3	Latitude	-39.5	-39
3	Down-dip width	3	20
3	Along-strike width	3	20
3	Origin Time	2019.31	2019.34
3	Time constant	0.9	2.5
4	Longitude	176.8	178.5
4	Latitude	-40.5	-39.7
4	Down-dip width	4	50
4	Along-strike width	4	50
4	Origin Time	2019.12	2019.18
4	Time constant	0.1	3
5	Longitude	177	178.2
5	Latitude	-39.7	-39
5	Down-dip width	3	55
5	Along-strike width	3	55
5	Origin Time	2019.18	2019.26
5	Time constant	7	18
6	Longitude	178	178.6
6	Latitude	-39.95	-39.25
6	Down-dip width	3	20

6	Along-strike width	3	20
6	Origin Time	2019.35	2019.45
6	Time constant	6	15
7	Longitude	178.2	178.8
7	Latitude	-39.1	-38.7
7	Down-dip width	3	30
7	Along-strike width	3	30
7	Origin Time	2019.1	2019.3
7	Time constant	12	20
8	Longitude	176.6	178.3
8	Latitude	-40.3	-39.6
8	Down-dip width	3	35
8	Along-strike width	3	35
8	Origin Time	2019.18	2019.28
8	Time constant	3	10

Table S1: Constraints applied to all parameter value bounds. We note that source amplitude and azimuth of the long-axis of the ellipse are not constrained.

Source	Duration (days)	Avg slip (cm)	Peak slip (cm)	Area (m^2)	Start	End	Longitude (center)	Latitude (center)	Site
1	11.5	2.7	7.5	1.45E+10	2019-03-25	2019-04-05	178.251	-38.906	MAKO
2	29.1	2.9	4.0	5.55E+09	2019-03-23	2019-04-21	178.118	-38.392	ANAU
3	6.7	2,5	8.8	6.35E+09	2019-04-29	2019-05-06	177.62	-39.201	MAHI
4	1.3	1.4	4.3	6.89E+09	2019-03-07	2019-03-08	177.459	-39.986	PAWA
5	72	3.5	10.3	1.67E+10	2019-03-14	2019-05-25	177.825	-39.608	CKID
6	42.8	4.8	12.5	5.93E+09	2019-05-18	2019-06-30	178.268	-39.626	POBS18-3
7	94.5	5.7	15.4	4.59E+09	2019-02-07	2019-05-12	178.491	-38.944	KU18-3
8	16.8	0.4	1.34	1.75E+10	2019-04-09	2019-04-26	176.905	-40.101	PAWA

Table S2: Source properties of each of the transient deformation sources in our time-dependent model (using TDefnode) of the for the 2019 SSE sequence, from our best-fitting model (reduced-Chi squared = 1.234). The last column lists an example of a GNSS or APG site that contains a notable signal due to the source. It is important to note that each transient (1-8) does not necessarily constitute a separate SSE, so this Table should not be used as an SSE catalog. In some cases, multiple transient sources are super-imposed to capture spatial migration of an individual event.

3.0 Additional InSAR figures and comparison to GNSS data

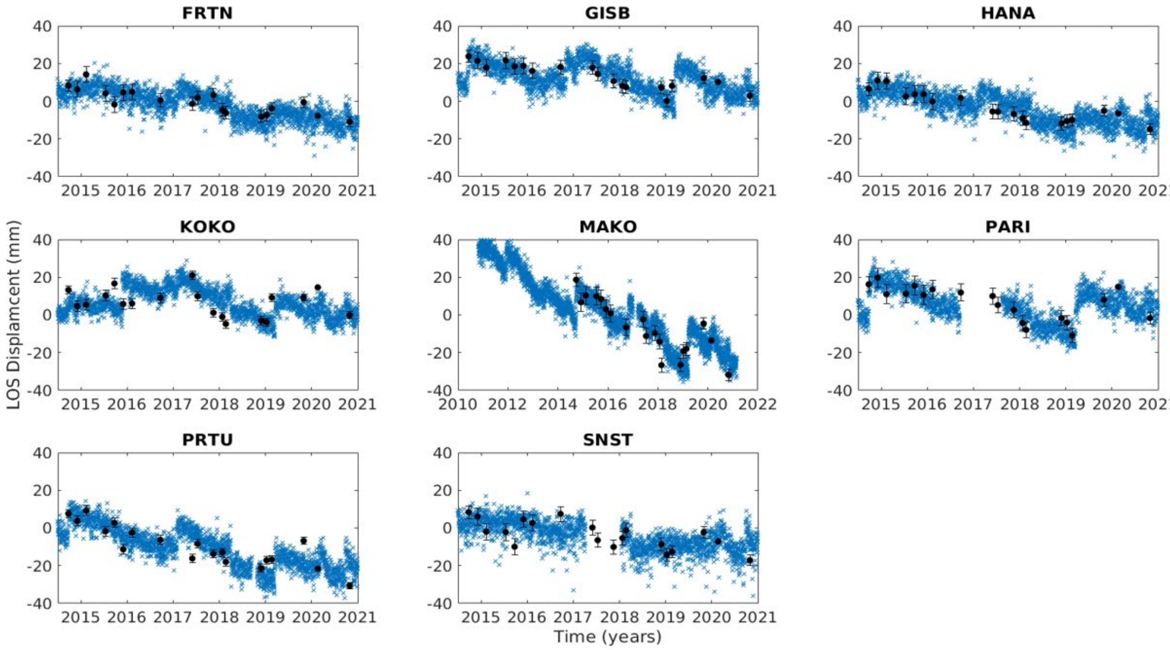

Figure S3: LOS displacement time series (in millimetres) from the August 2014 to November 2020 ALOS-2 InSAR data (black) for co-located pixels and GeoNet continuous GNSS (blue) at Gisborne for: Frasertown (FRTN), Gisborne (GISB), Hangaroa (HANA), Kokohu (KOKO), Makorori (MAKO), Paritu Road (PARI), Paparatu (PRTU), and Shannon Station (SNST). The GNSS data are the three-component GeoNet time series converted into the satellite LOS. Figure modified from Hamling and Wallace (2021).

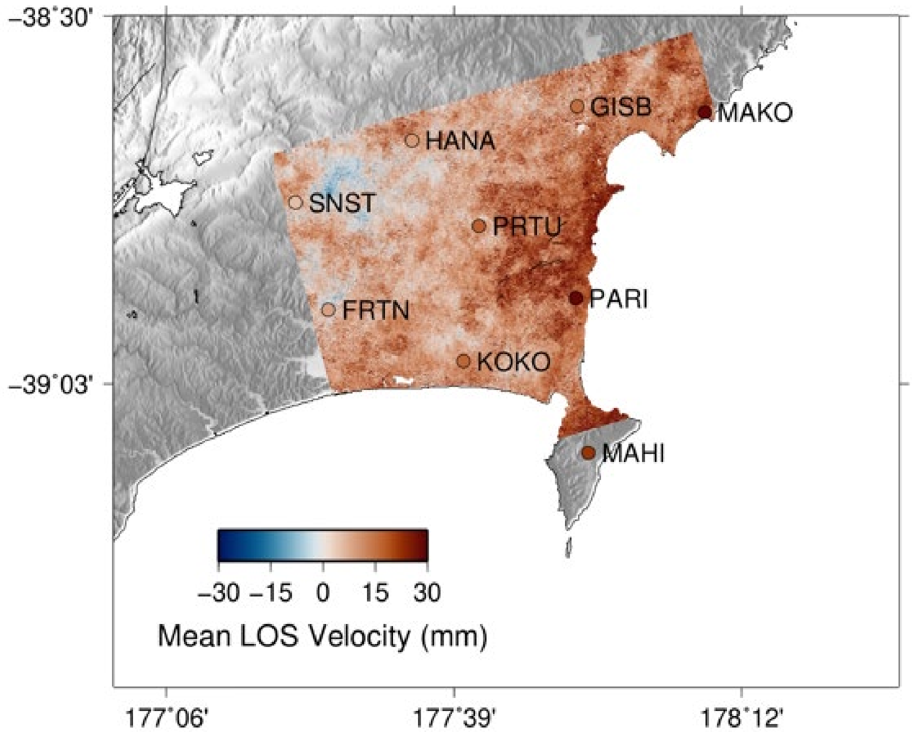

Figure S4: Resolved LOS displacement field at the Gisborne region for the 2019 SSE, extracted from the August 2014 to November 2020 InSAR time series. The coloured circles indicate the equivalent LOS displacement from GeoNet continuous GNSS sites. Positive LOS changes represent motion away from the satellite, which is equivalent to eastward, northward, and downward (subsidence) motion.

4.0 Fit to the observed GNSS and seafloor pressure timeseries

The following figures present the observed time series data with the displacement time series produced by our best-fitting model (presented in Figures 2 and 4). The plot for each site shows the east component observed displacements in red, the north component observed displacement in gold, the up component observed displacement in purple, the forward modelled displacement of our final solution as solid black lines, and the residual displacement for each component (observation minus modelled) as black circles.

AHTI

[178.046] [-38.4115]

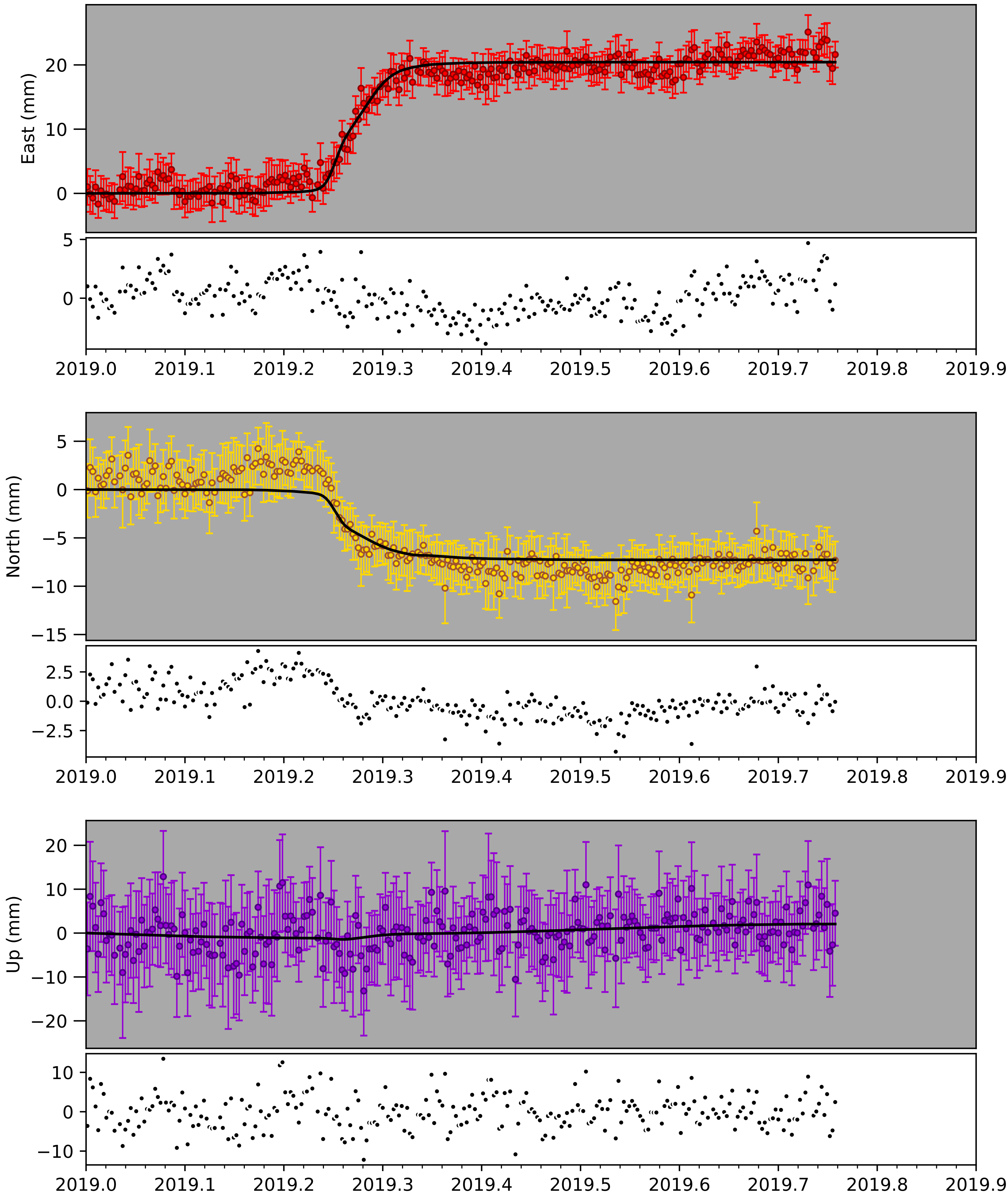

AKTO

[176.4612] [-40.5398]

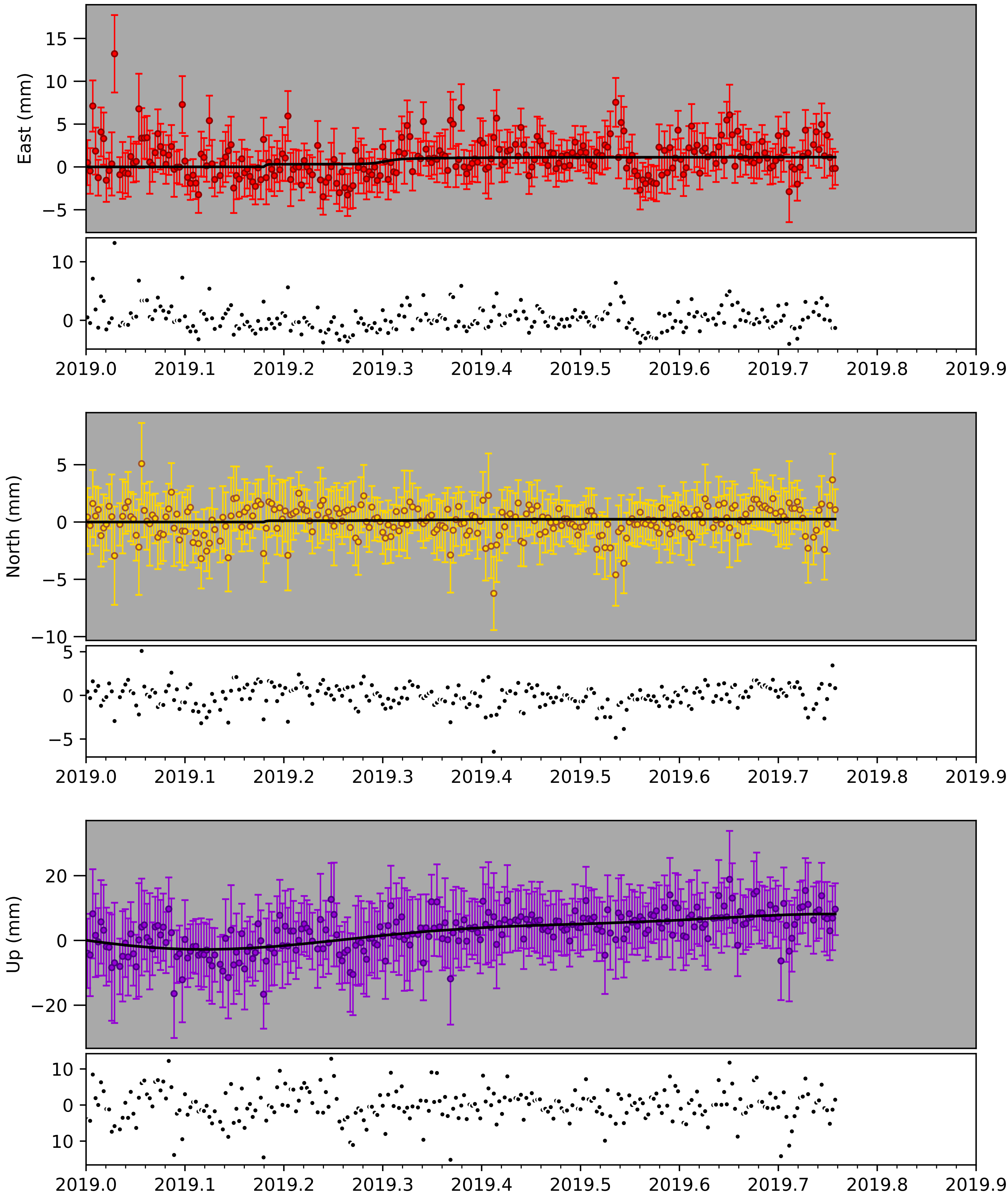

ANAU

[178.2912] [-38.2682]

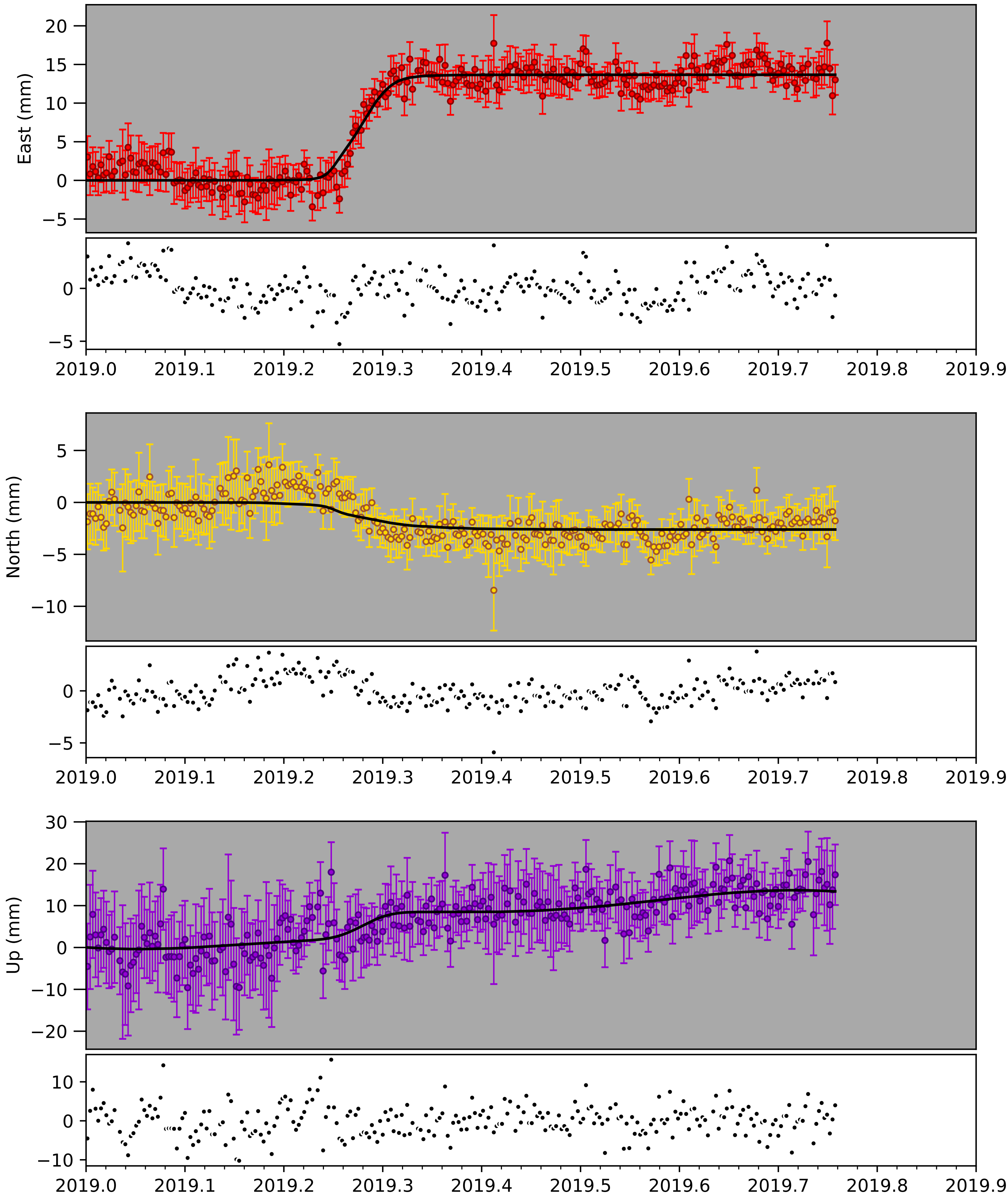

BHST

[176.0632] [-39.4892]

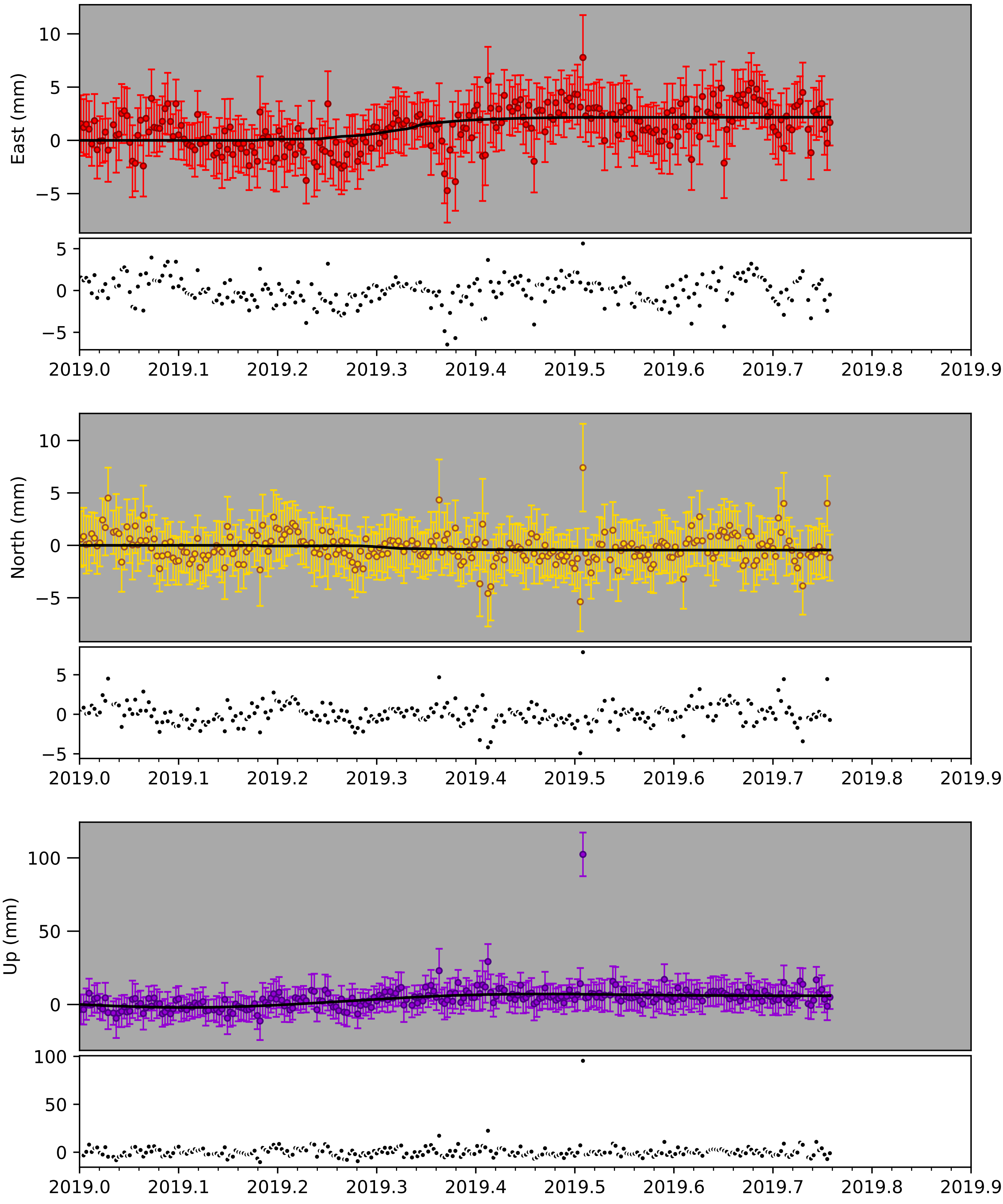

BIRF

[176.2461] [-40.6798]

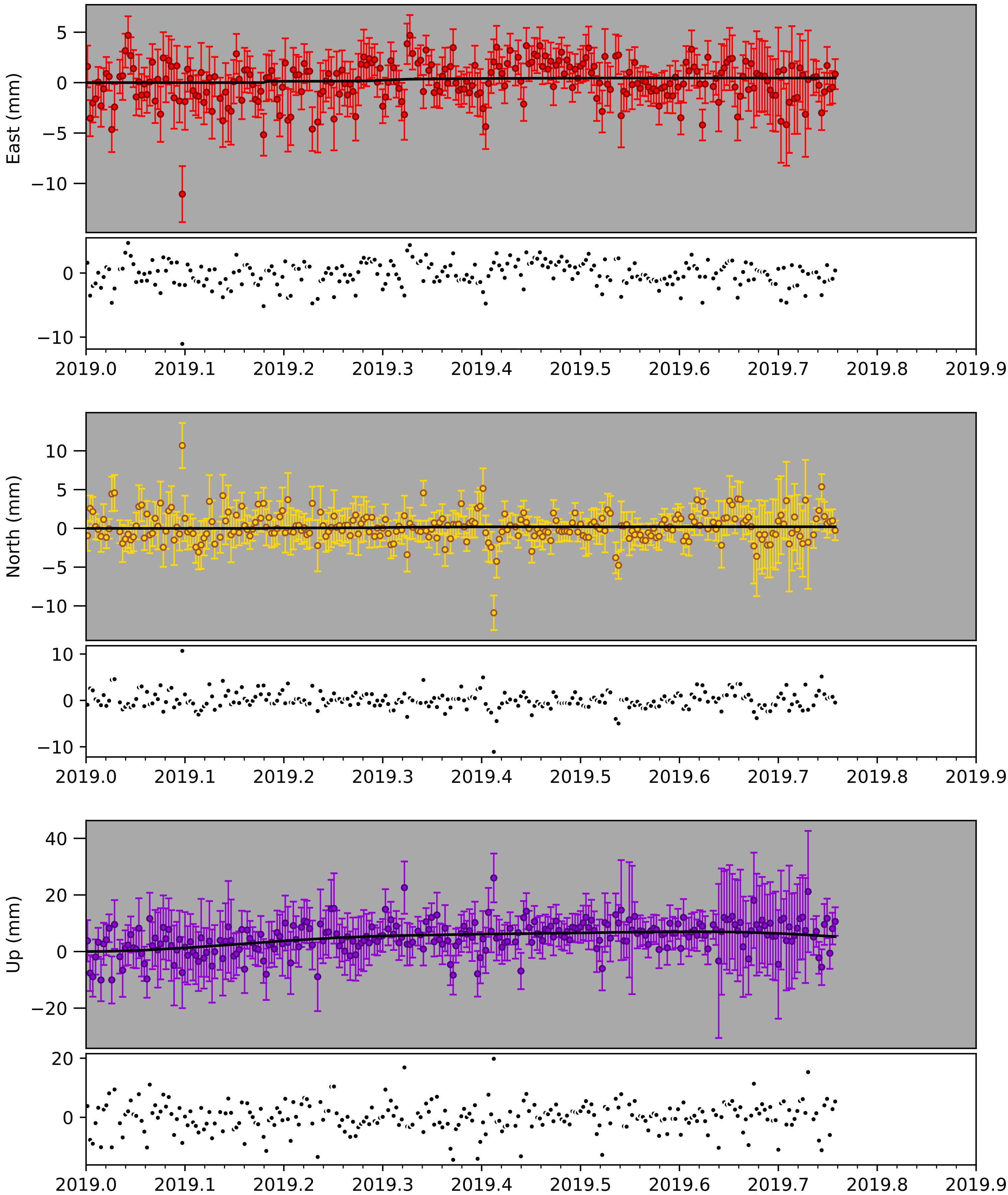

CAST

[176.2016] [-40.9098]

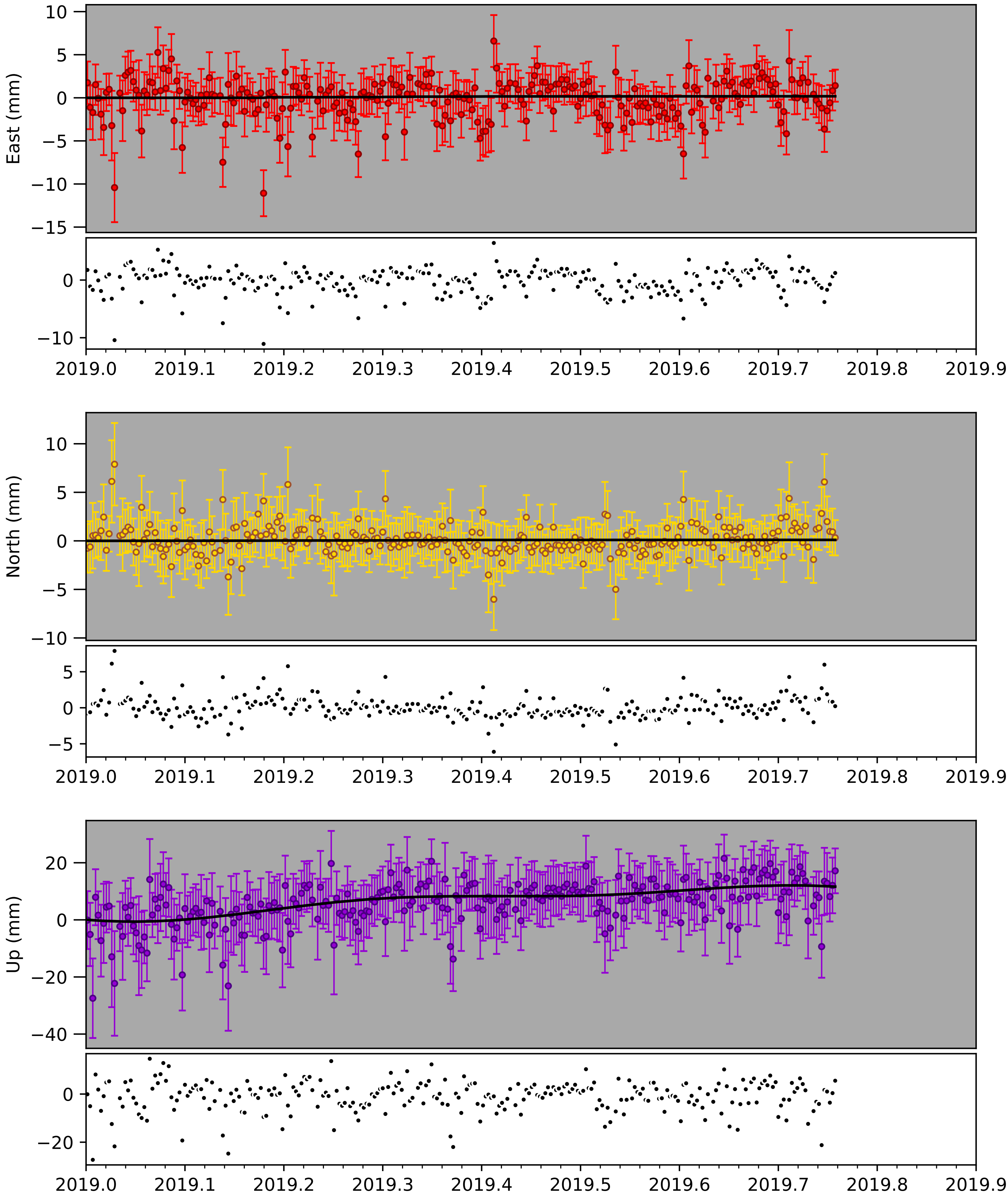

CKID

[177.0763] [-39.6579]

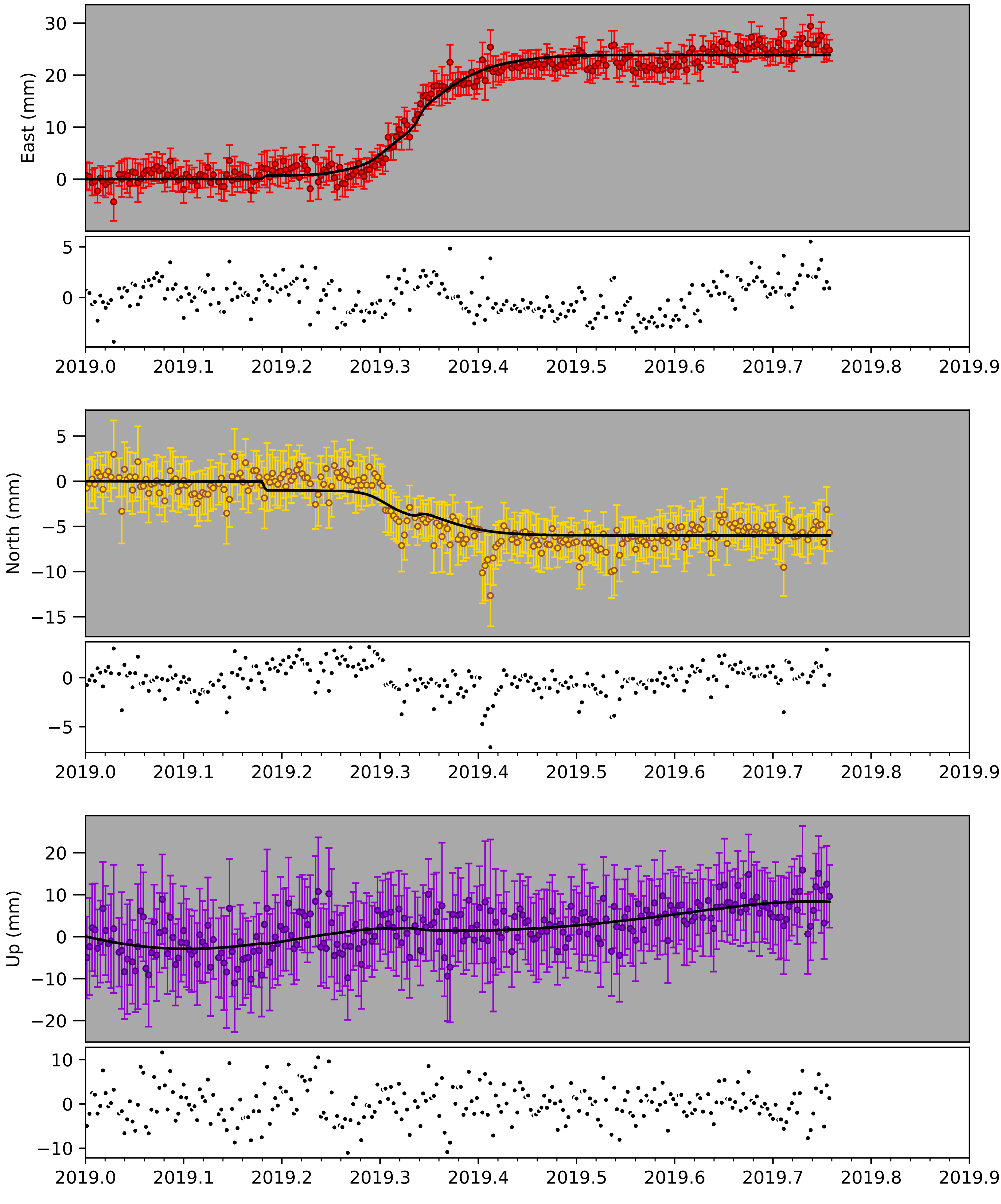

CNST

[178.2111] [-38.488]

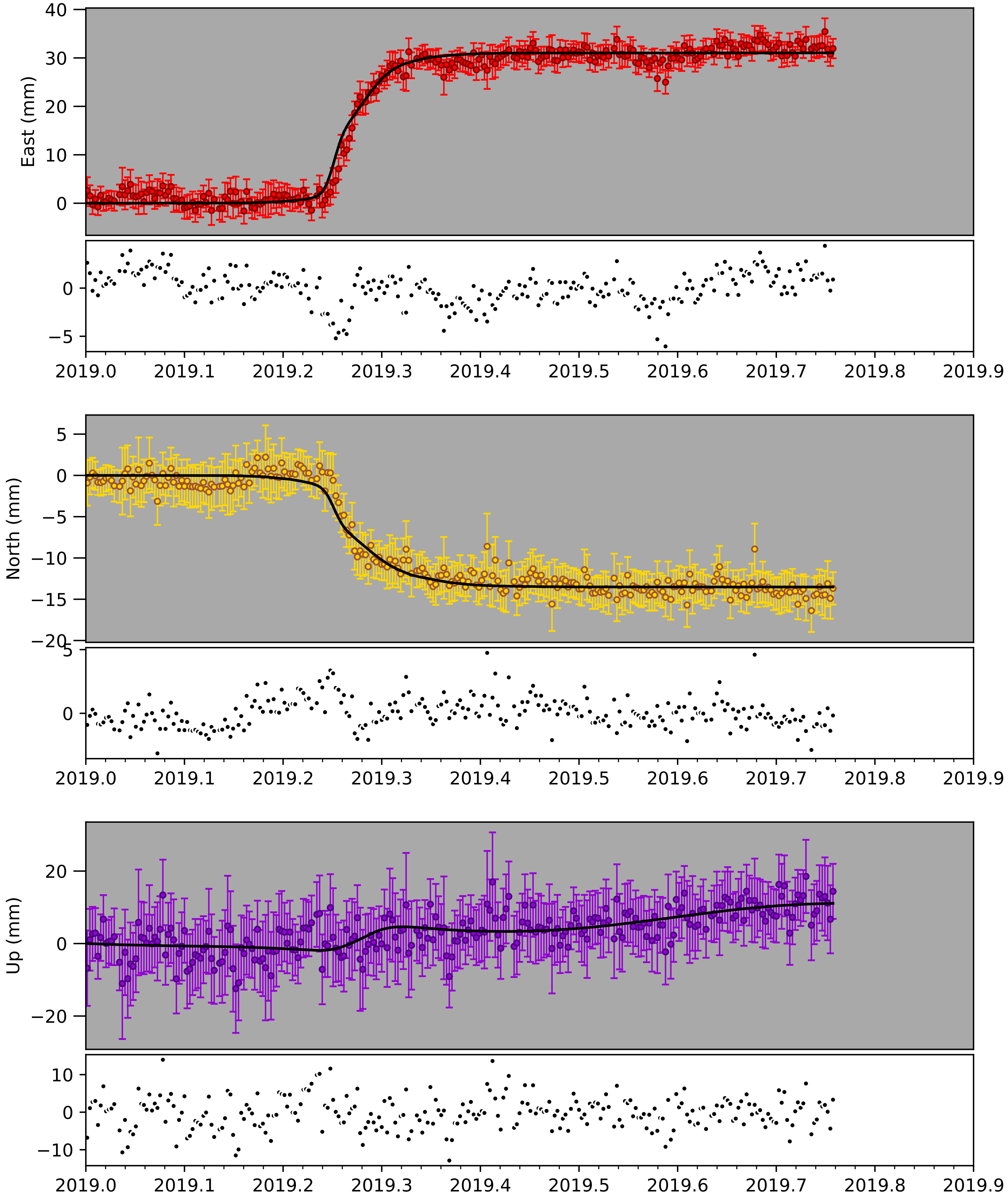

DNVK

[176.1667] [-40.2989]

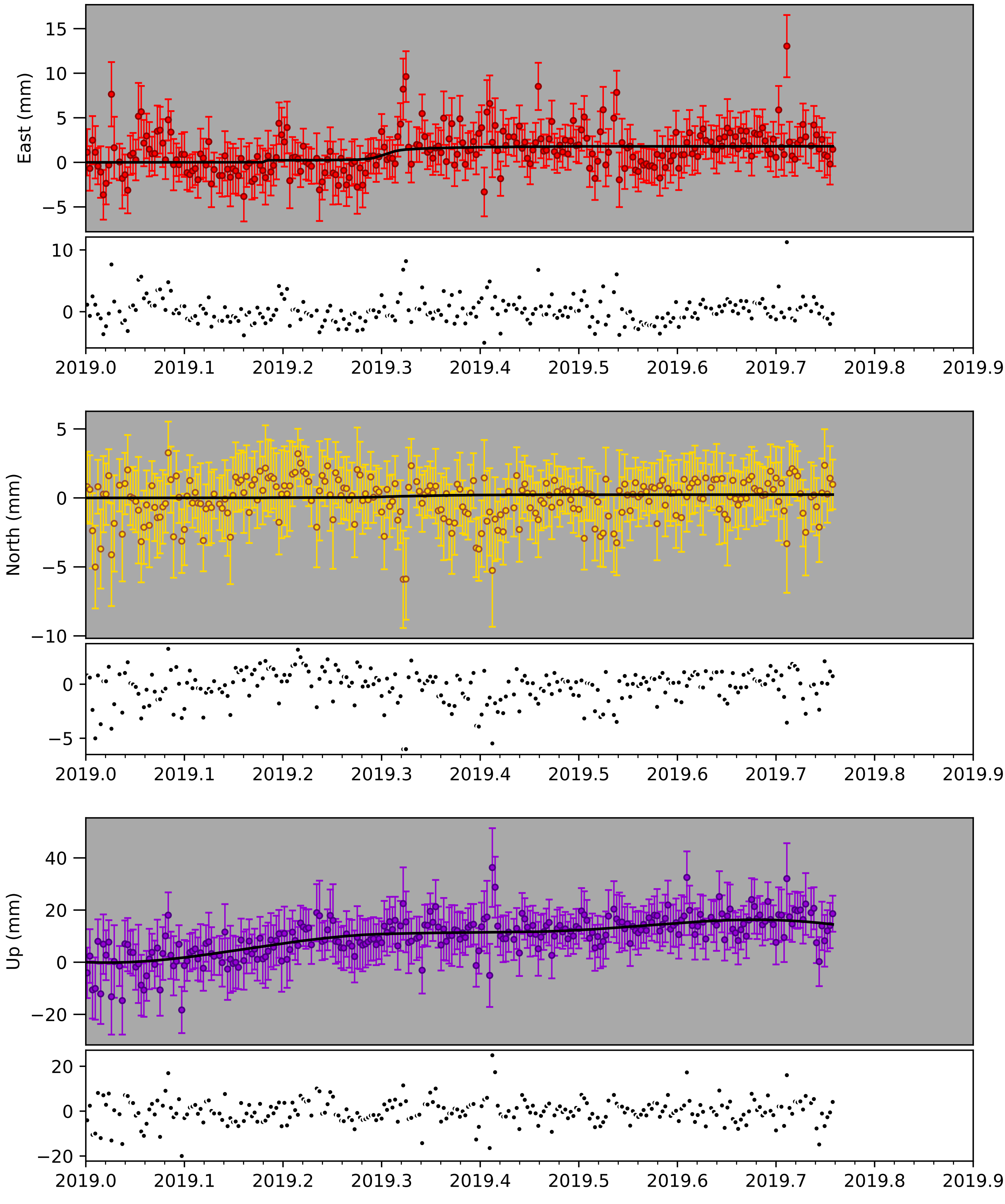

FRTN

[177.4099] [-38.9393]

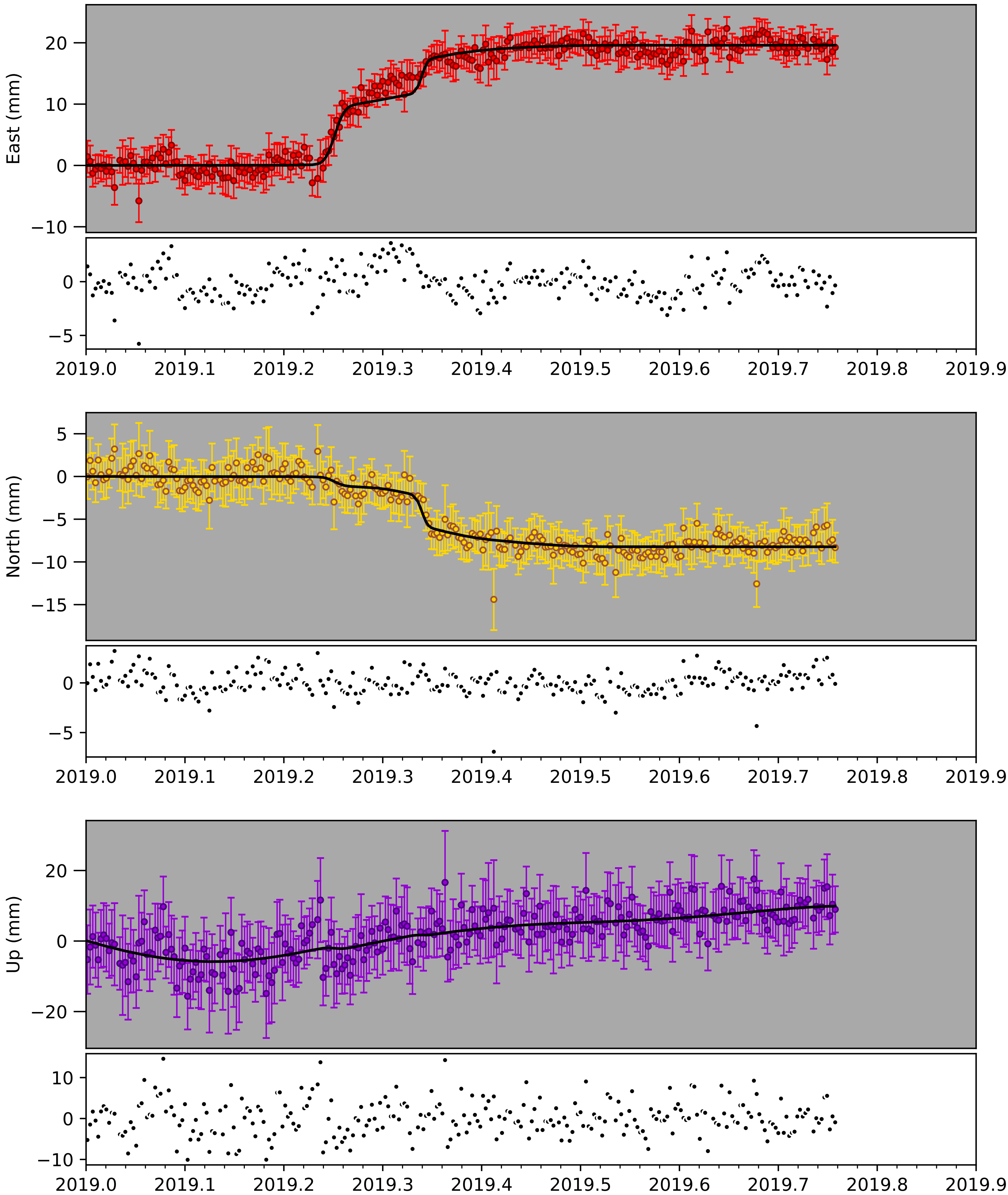

GISB

[177.886]   [-38.6353]

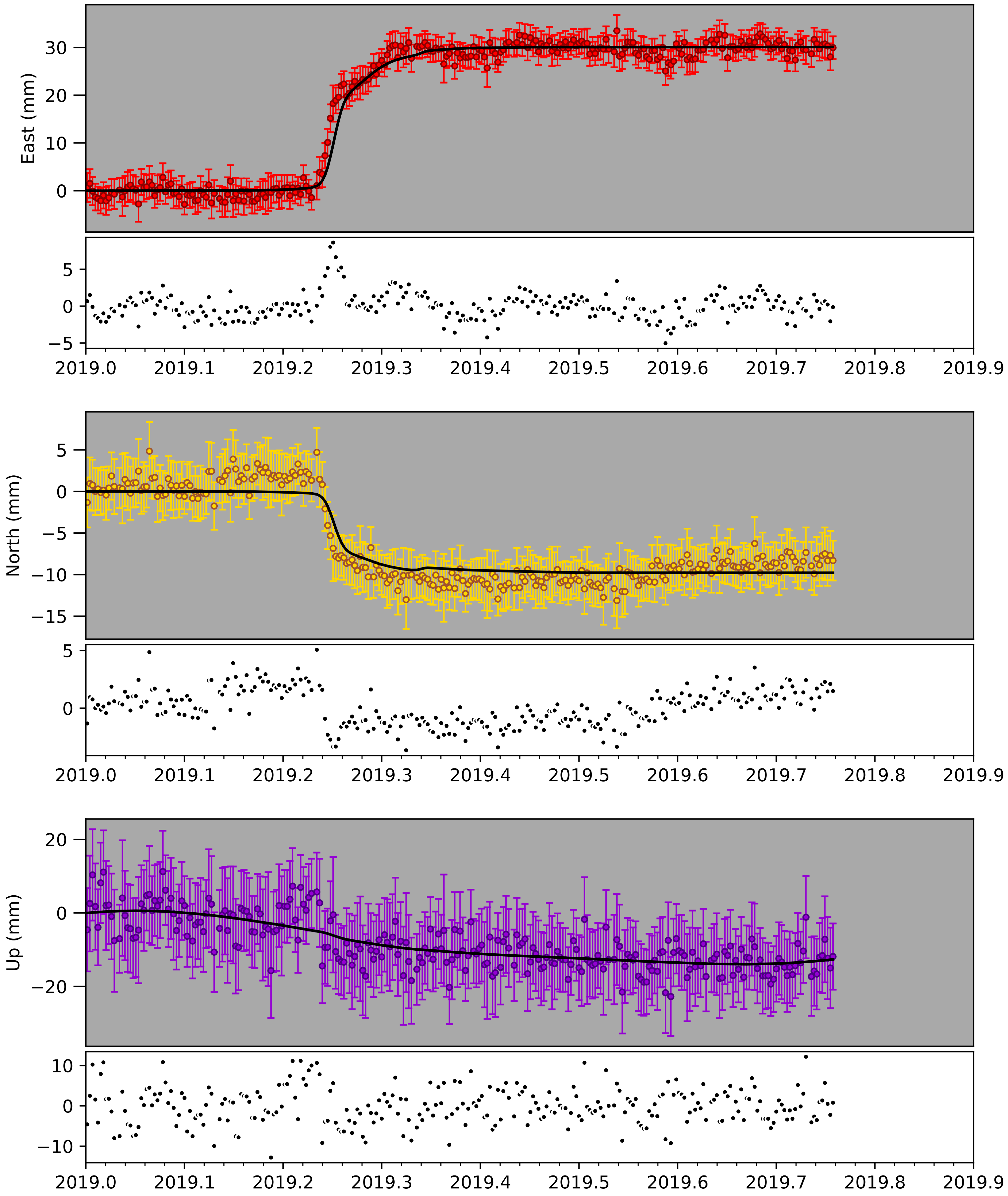

GNS3

[178.1485] [-39.6467]

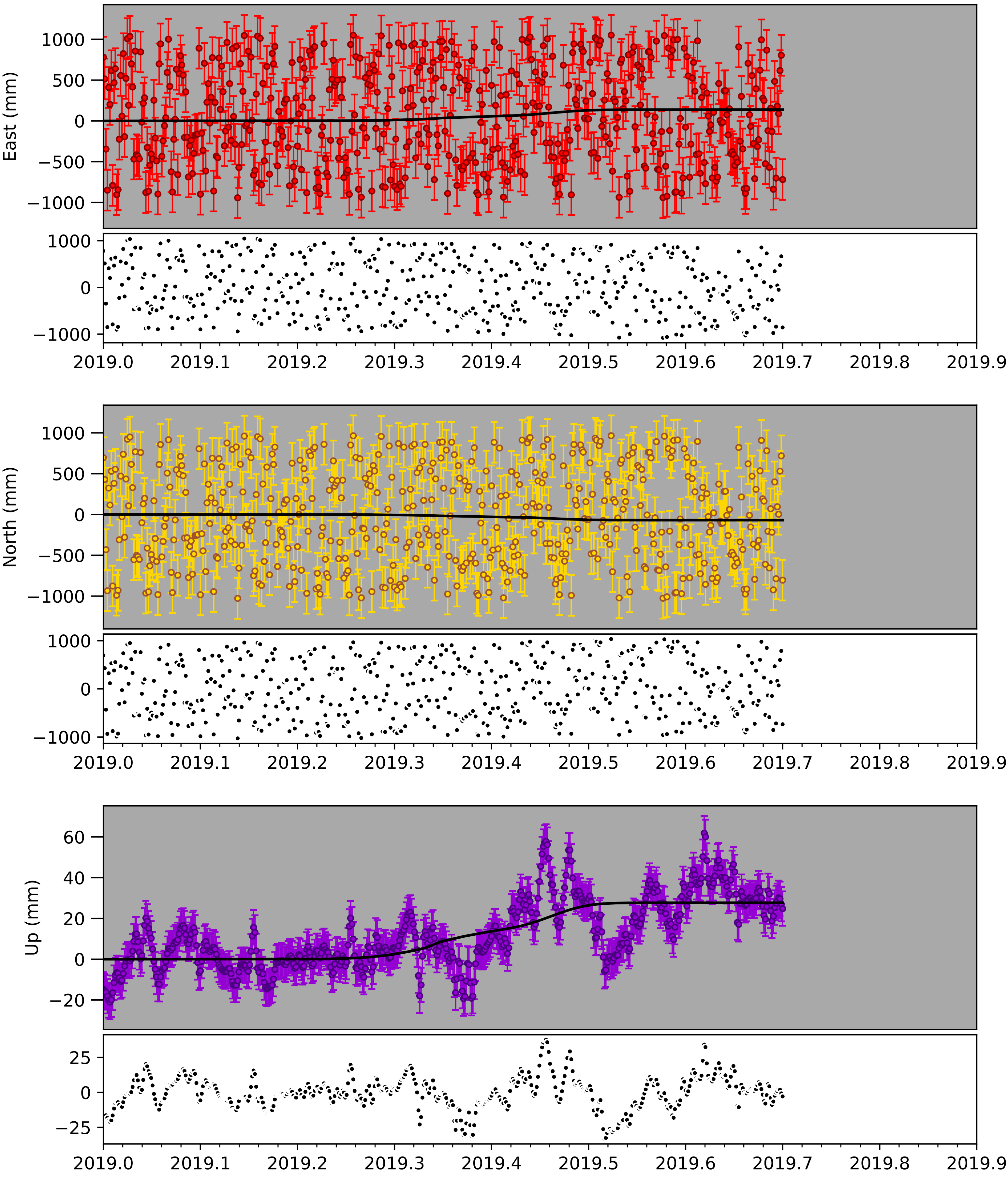

HANA

[177.5694] [-38.6868]

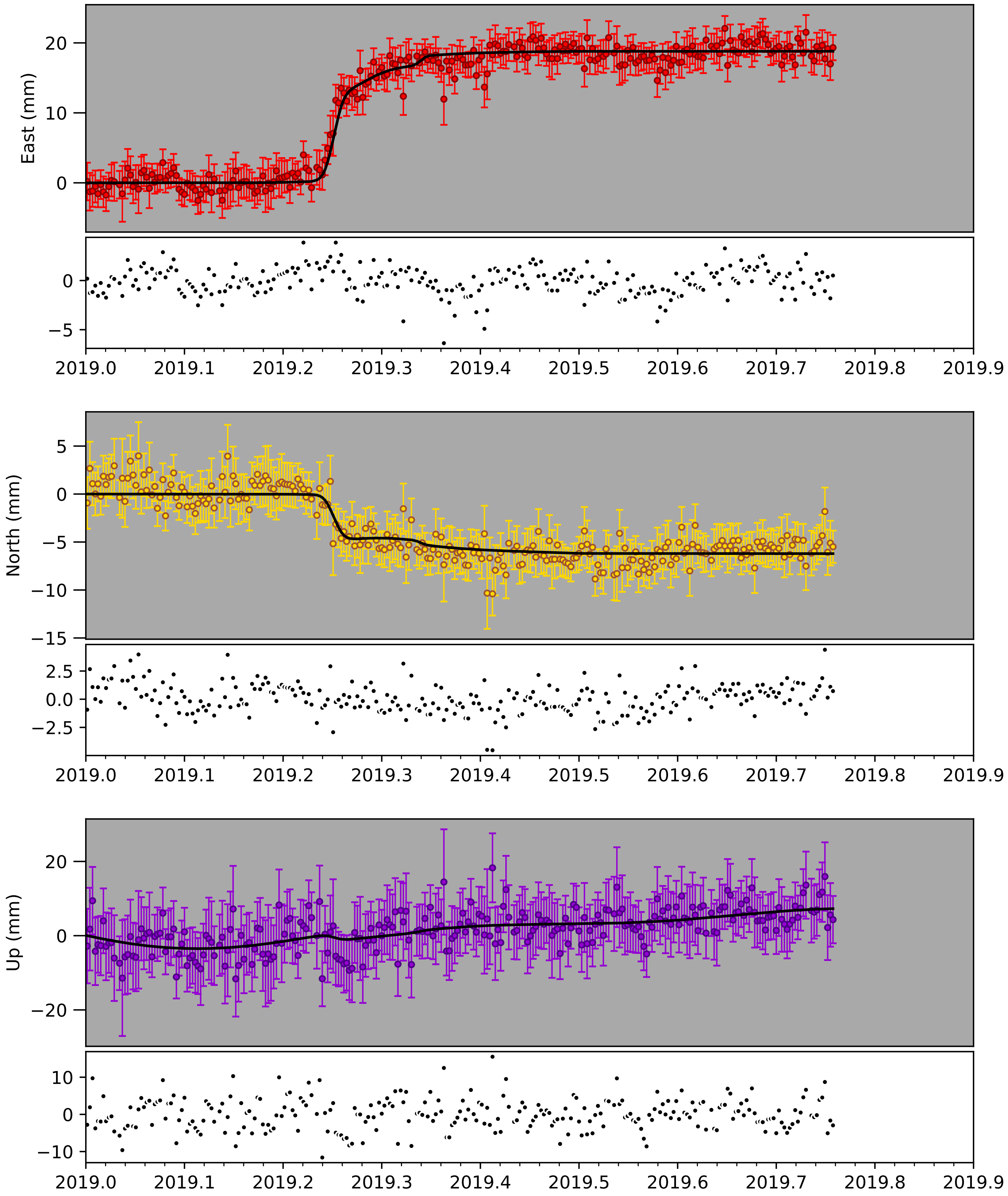

HAST

[176.7266] [-39.617]

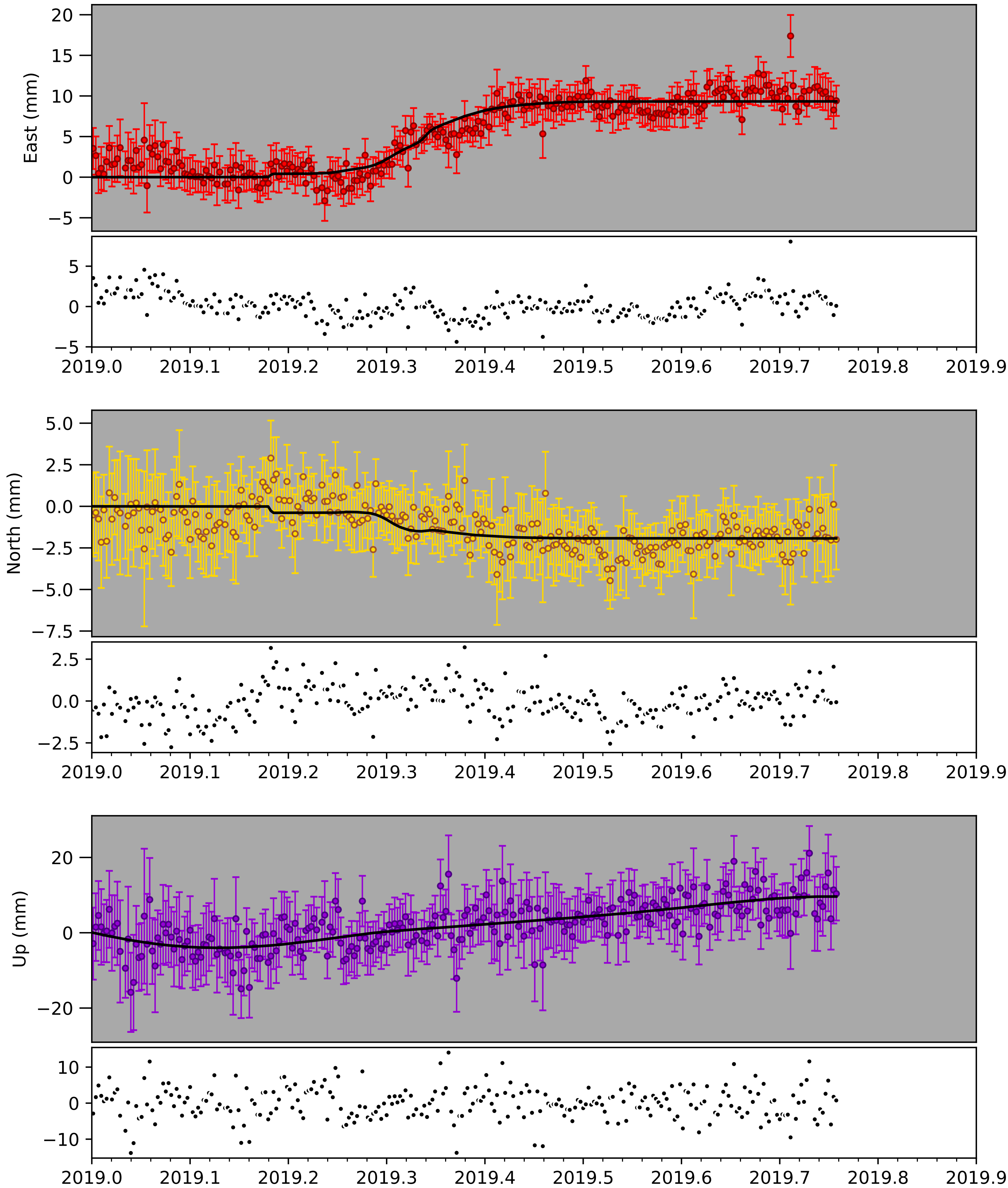

HIKB

[178.3033] [-37.561]

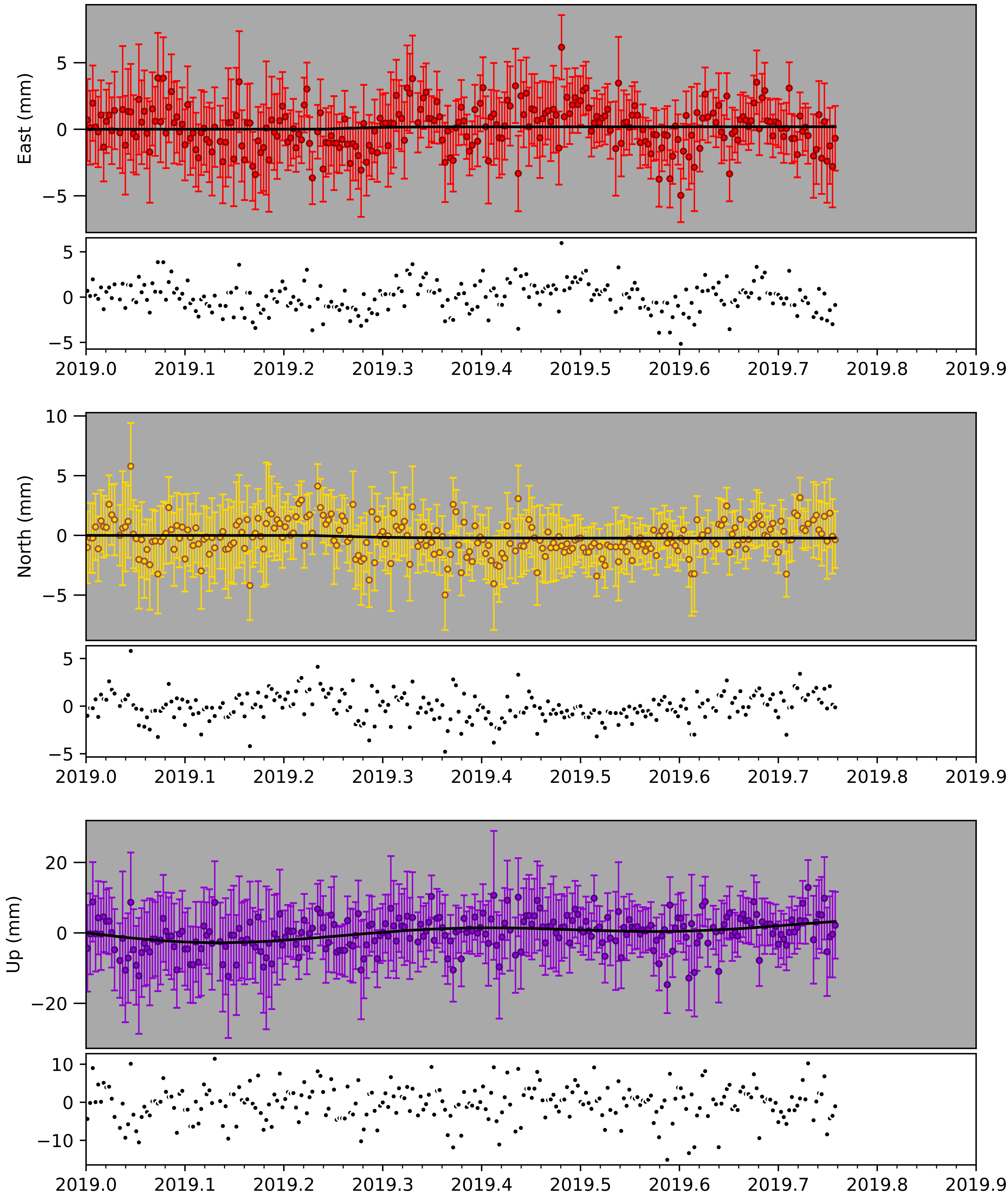

KAHU

[176.8763] [-39.7938]

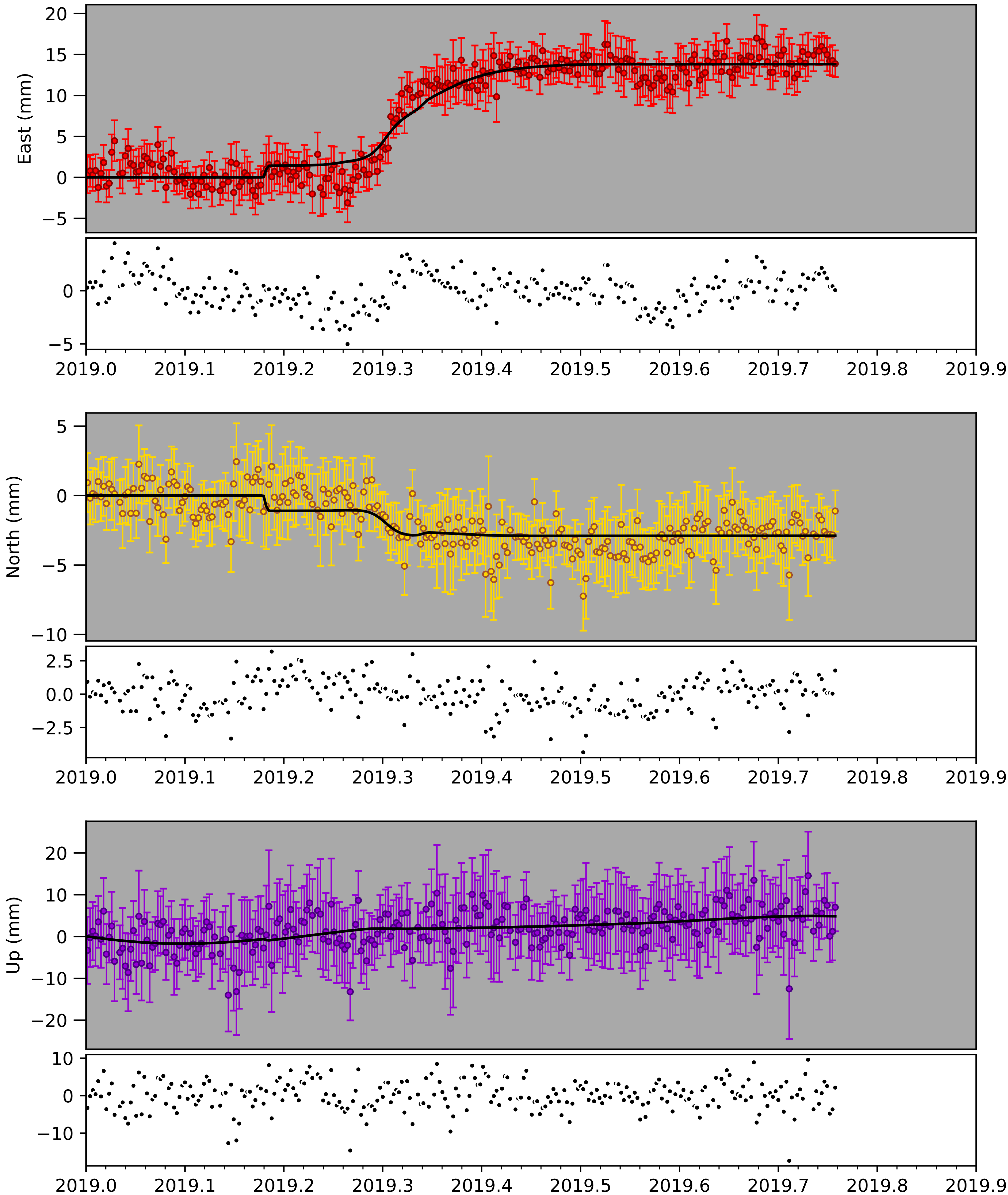

KAWK

[176.4228] [-39.424]

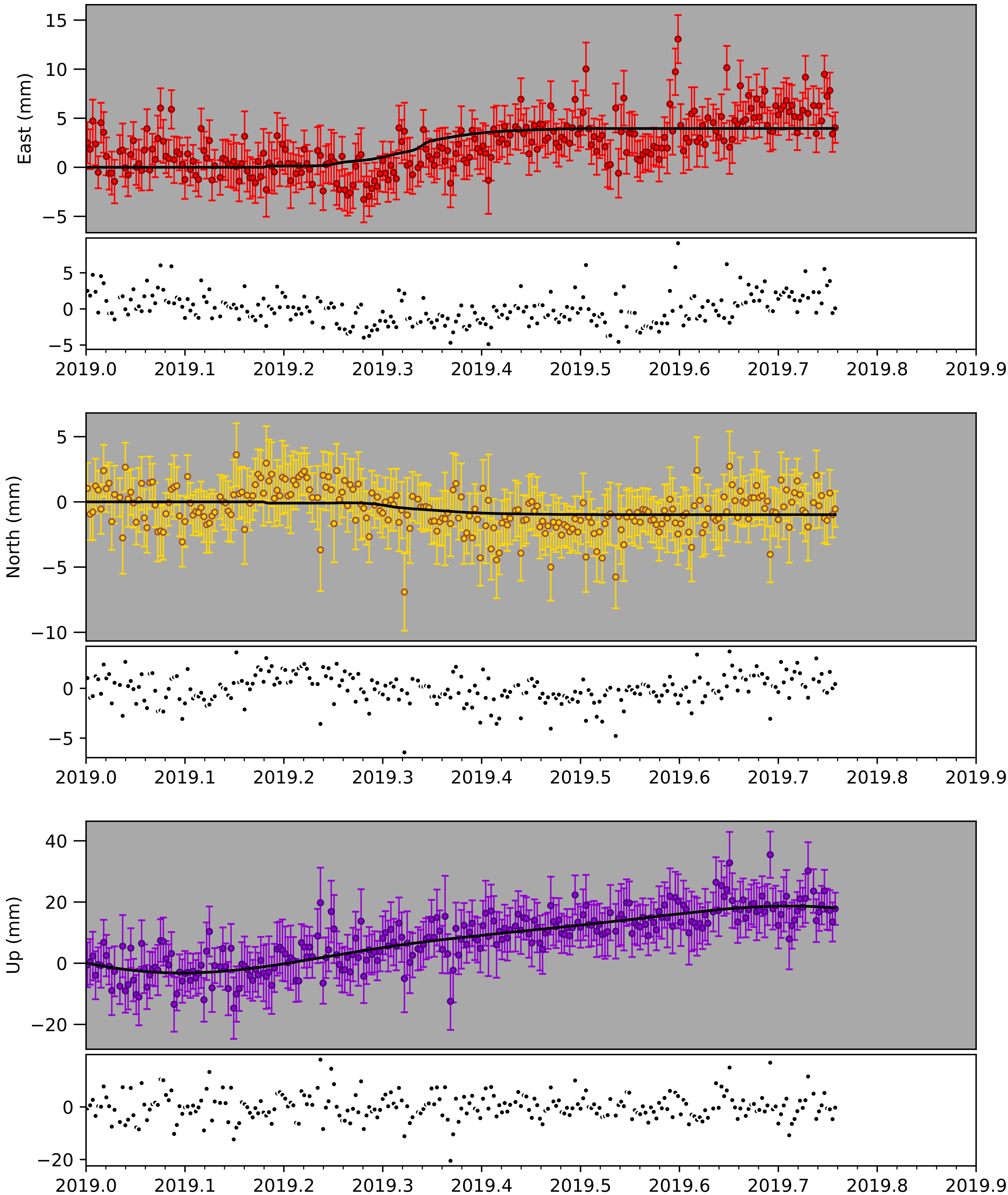

KERE

[176.3701] [-39.6432]

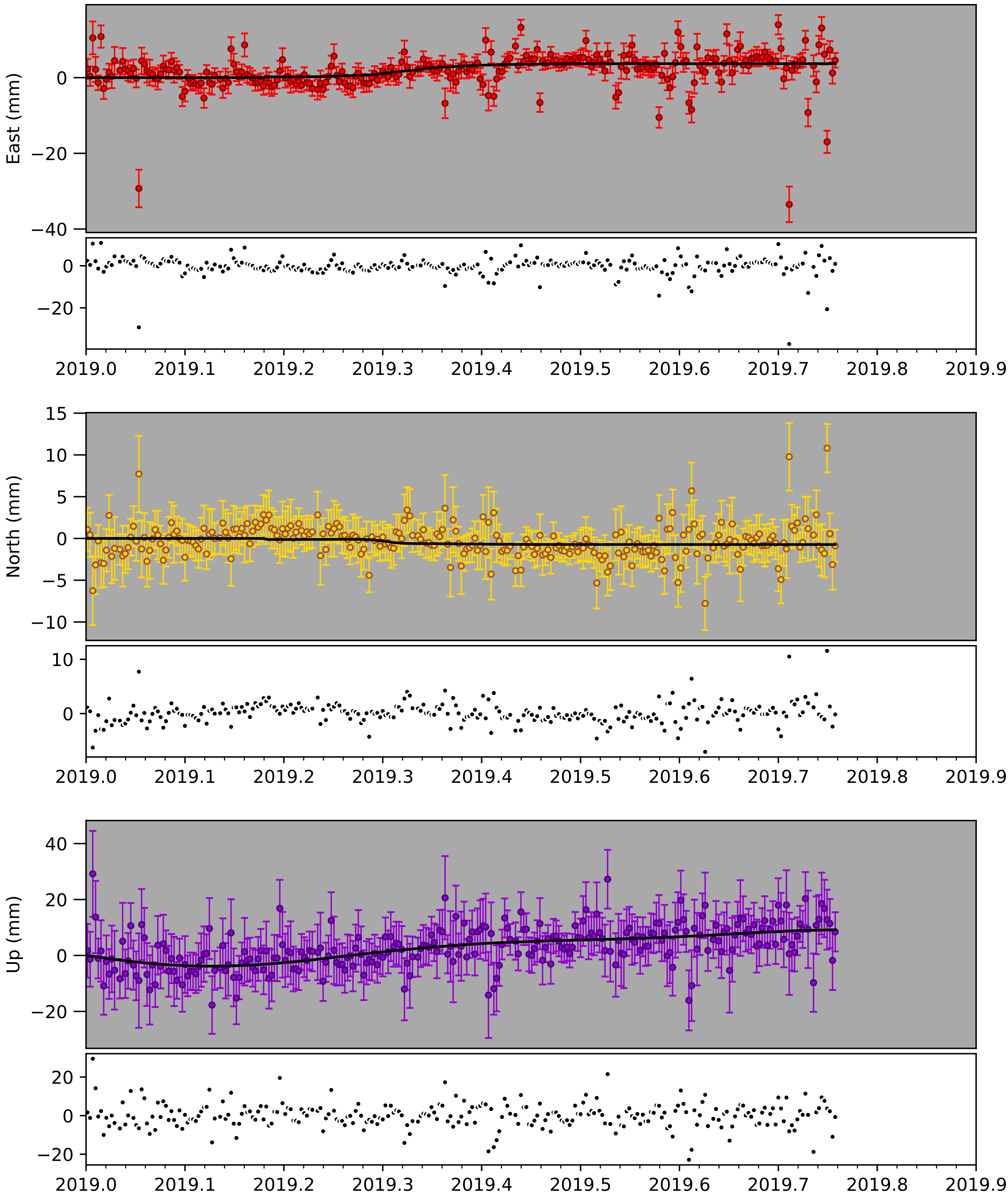

KOKO

[177.6678] [-39.0161]

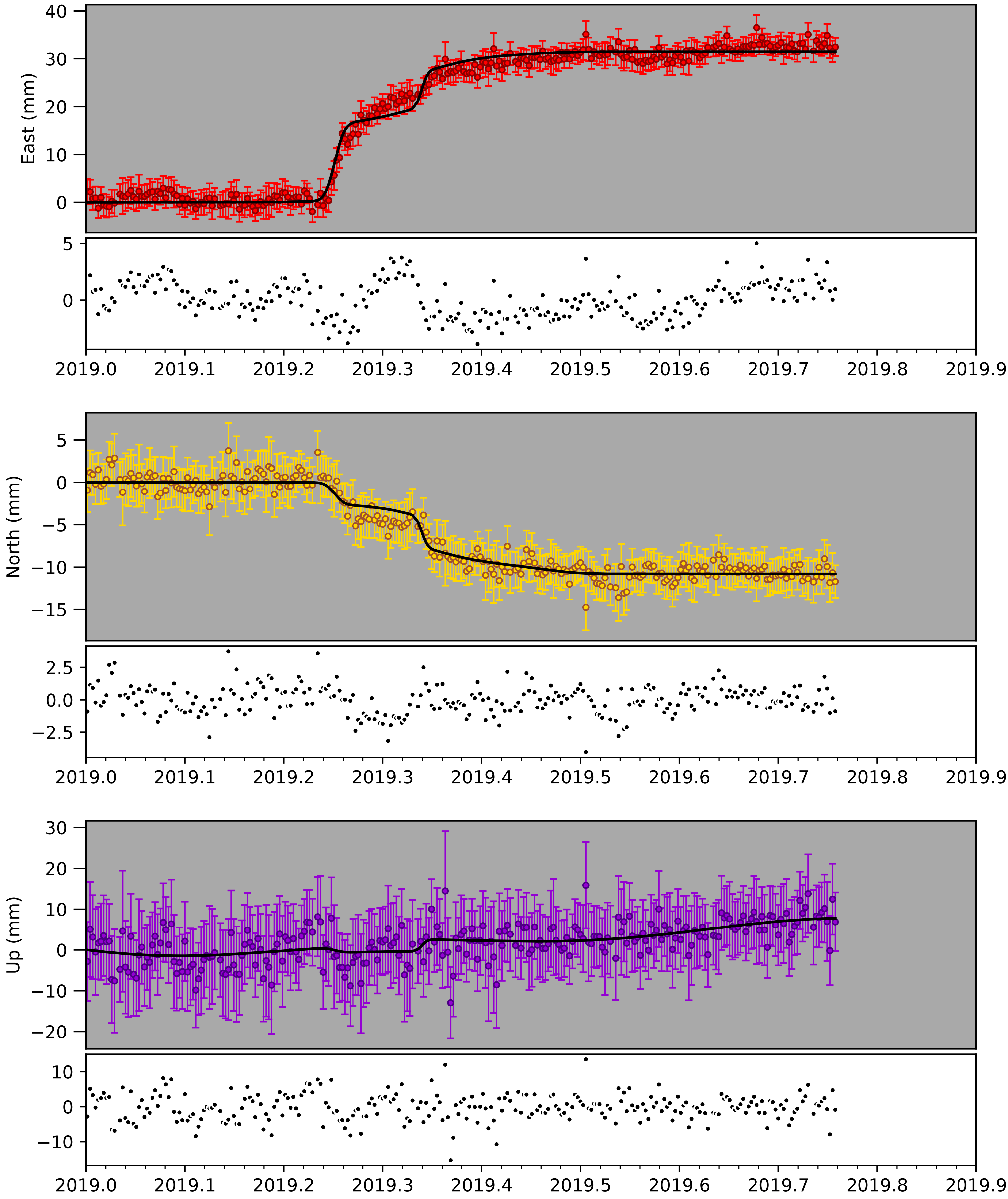

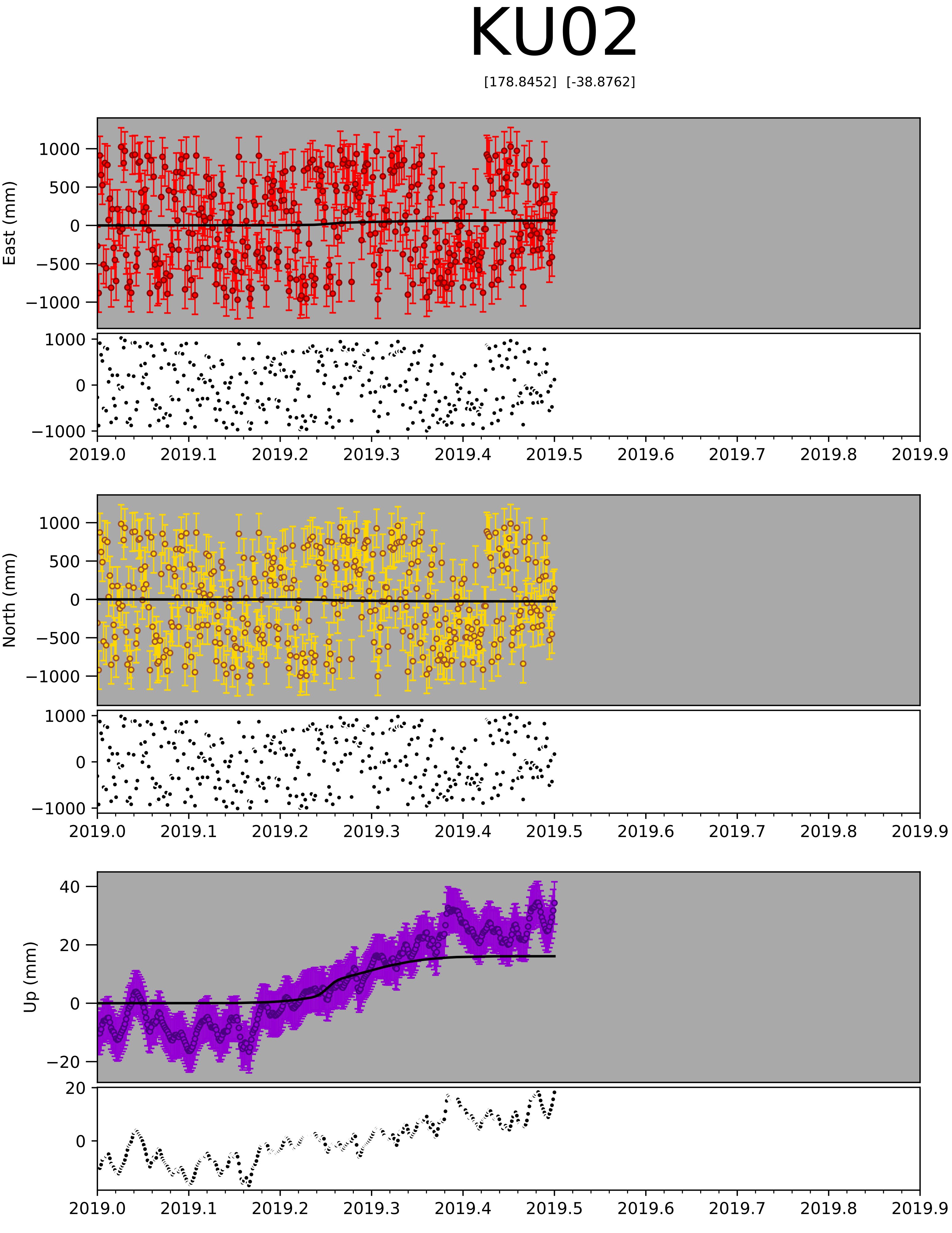

KU02
[178.8452] [-38.8762]
East (mm)
North (mm)
Up (mm)
1000
500
0
−500
−1000
40
20
−20
2019.0
2019.1
2019.2
2019.3
2019.4
2019.5
2019.6
2019.7
2019.8
2019.9

KU03

[178.7551] [-38.8926]

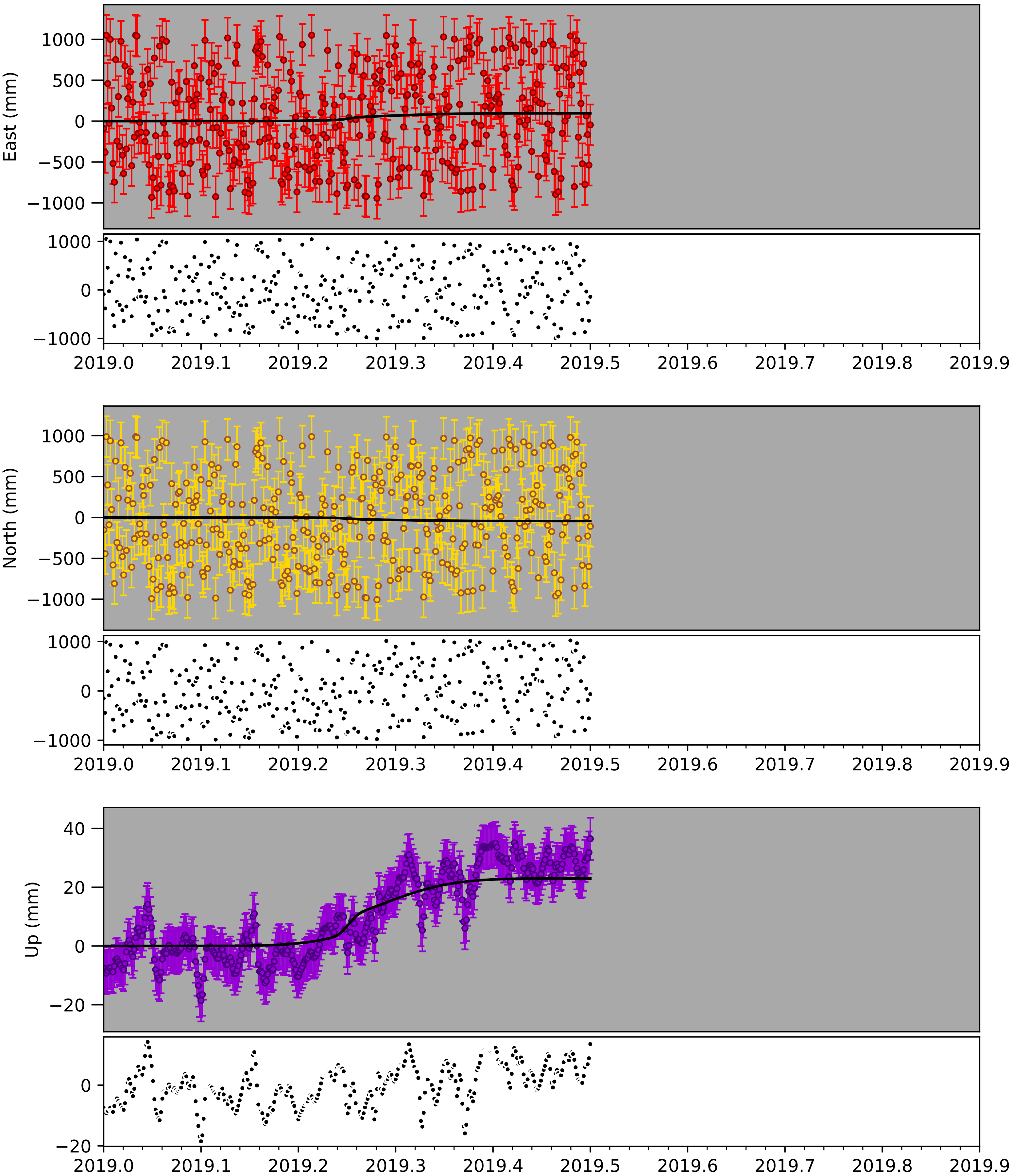

KU04

[178.671] [-38.7939]

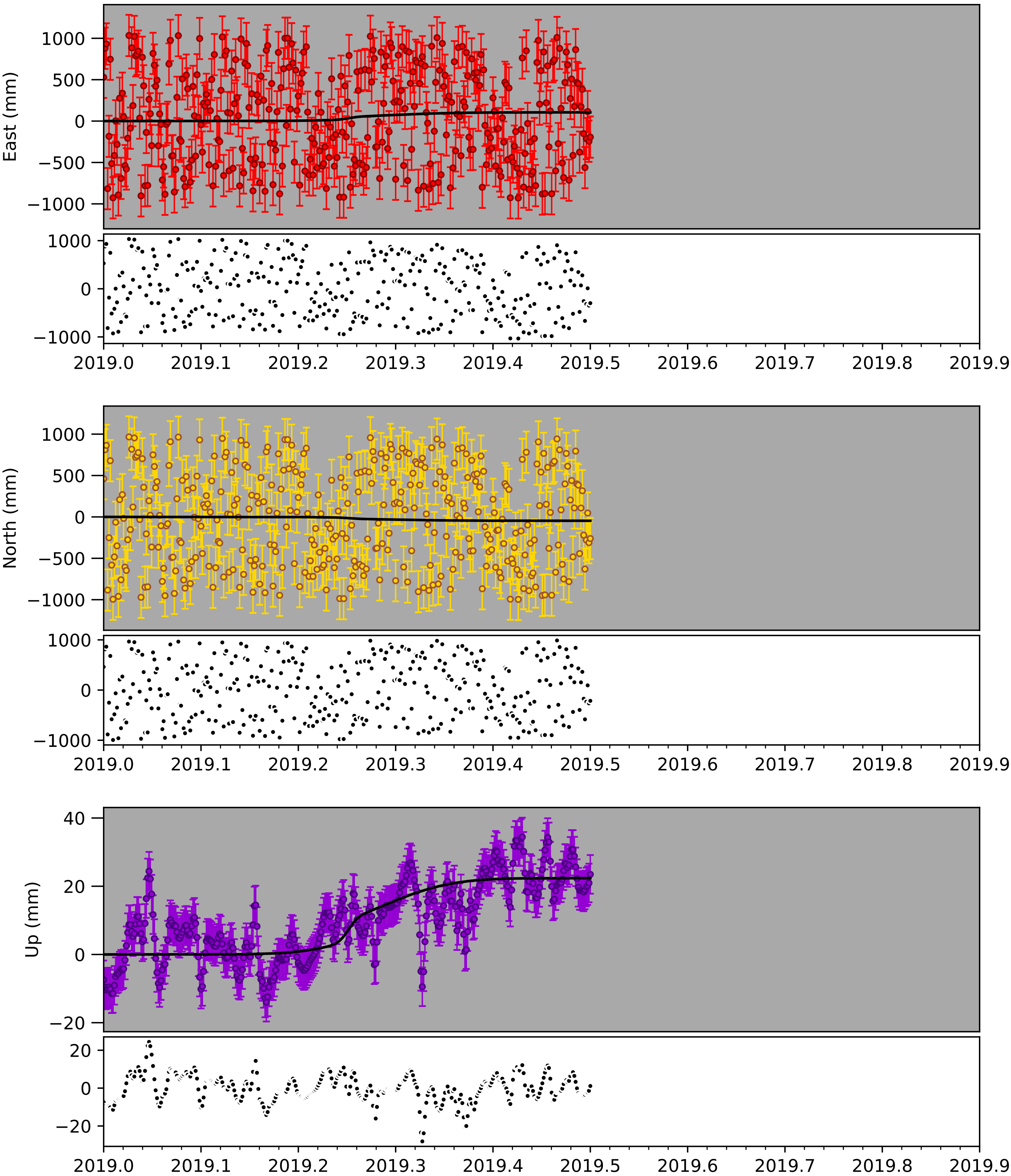

KUTA

[177.0698] [-39.1723]

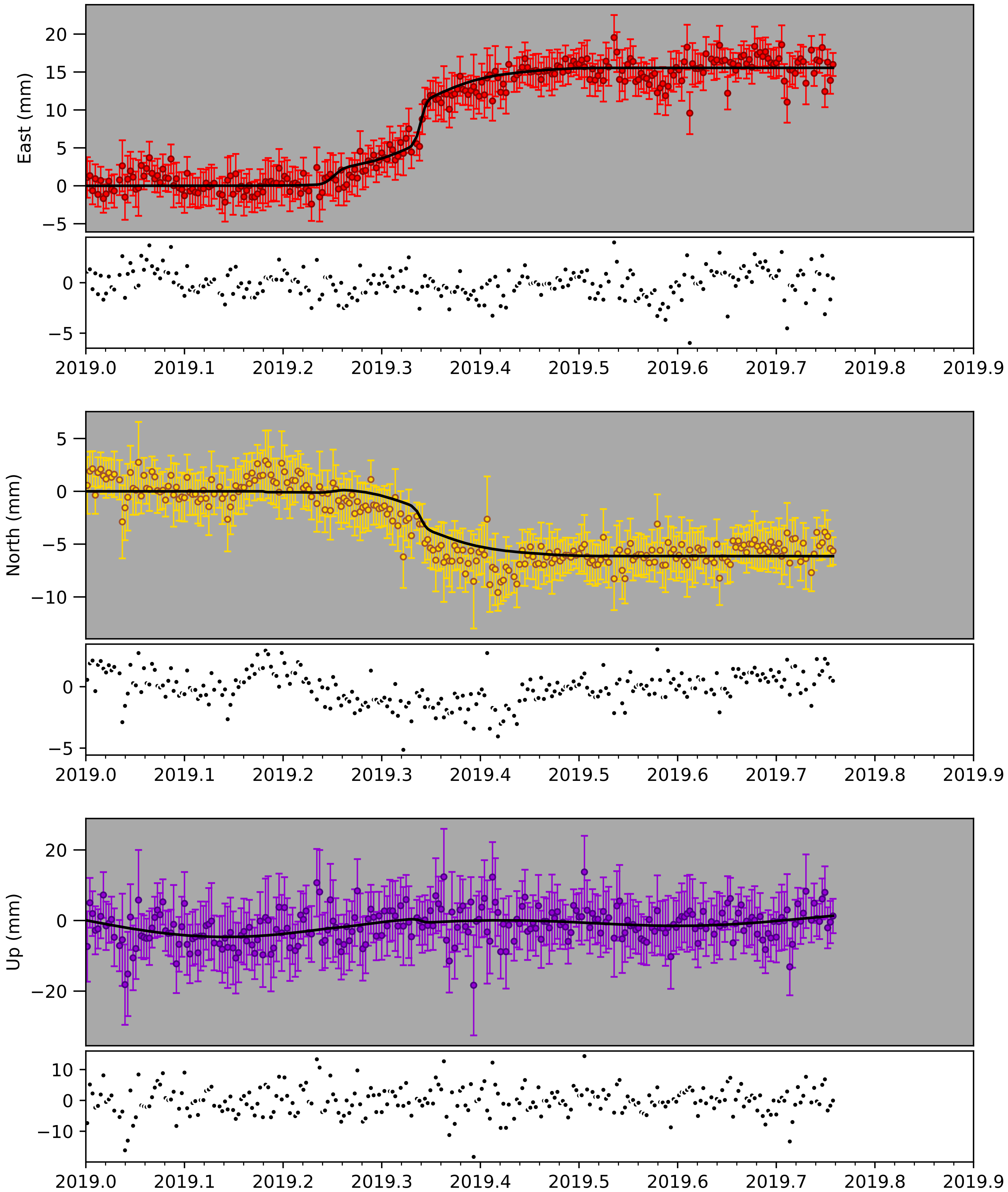

LBP4

[178.4845] [-39.7668]

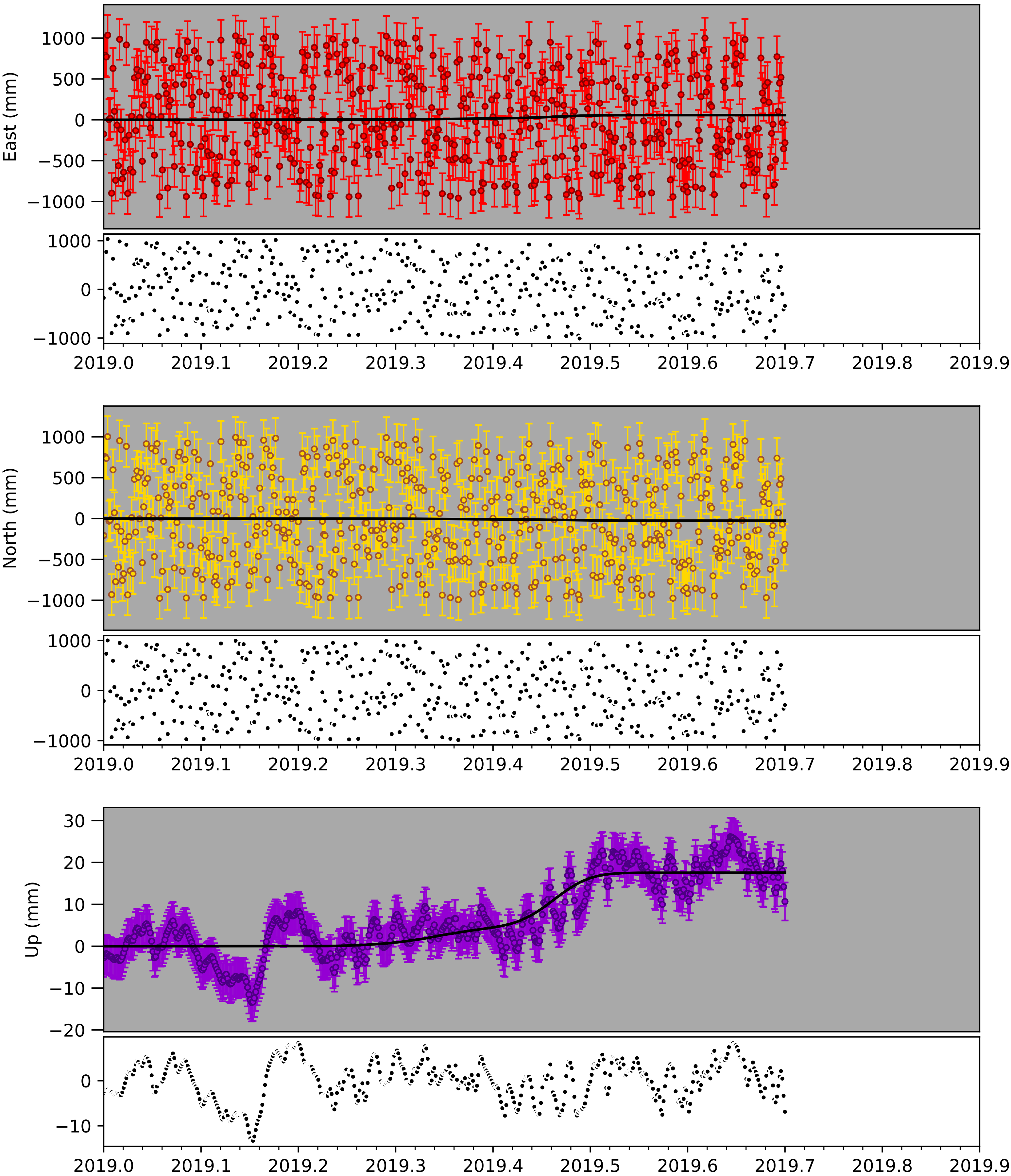

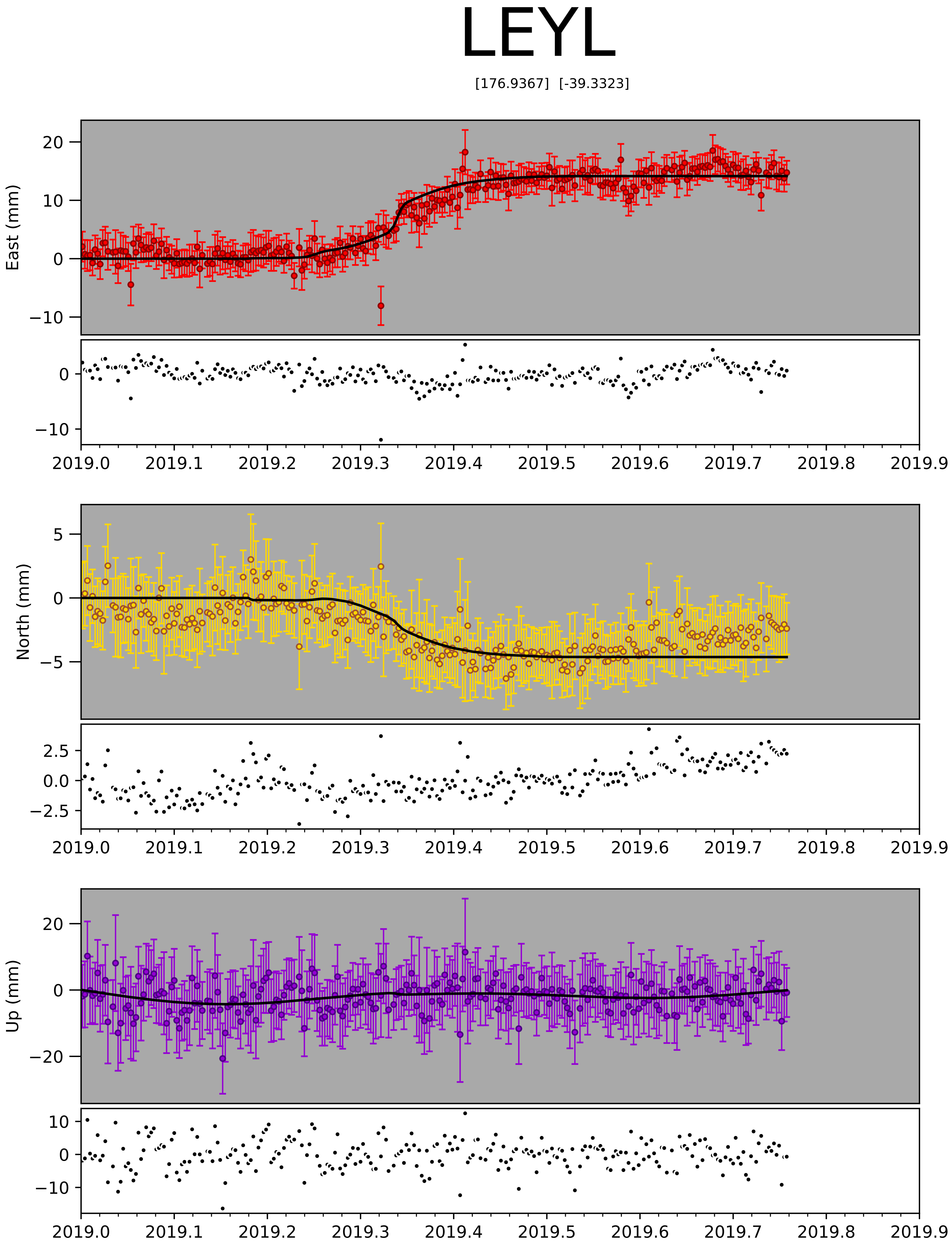

LEYL
[176.9367] [-39.3323]
East (mm)
North (mm)
Up (mm)
2019.0
2019.1
2019.2
2019.3
2019.4
2019.5
2019.6
2019.7
2019.8
2019.9

MAHI

[177.907]   [-39.1526]

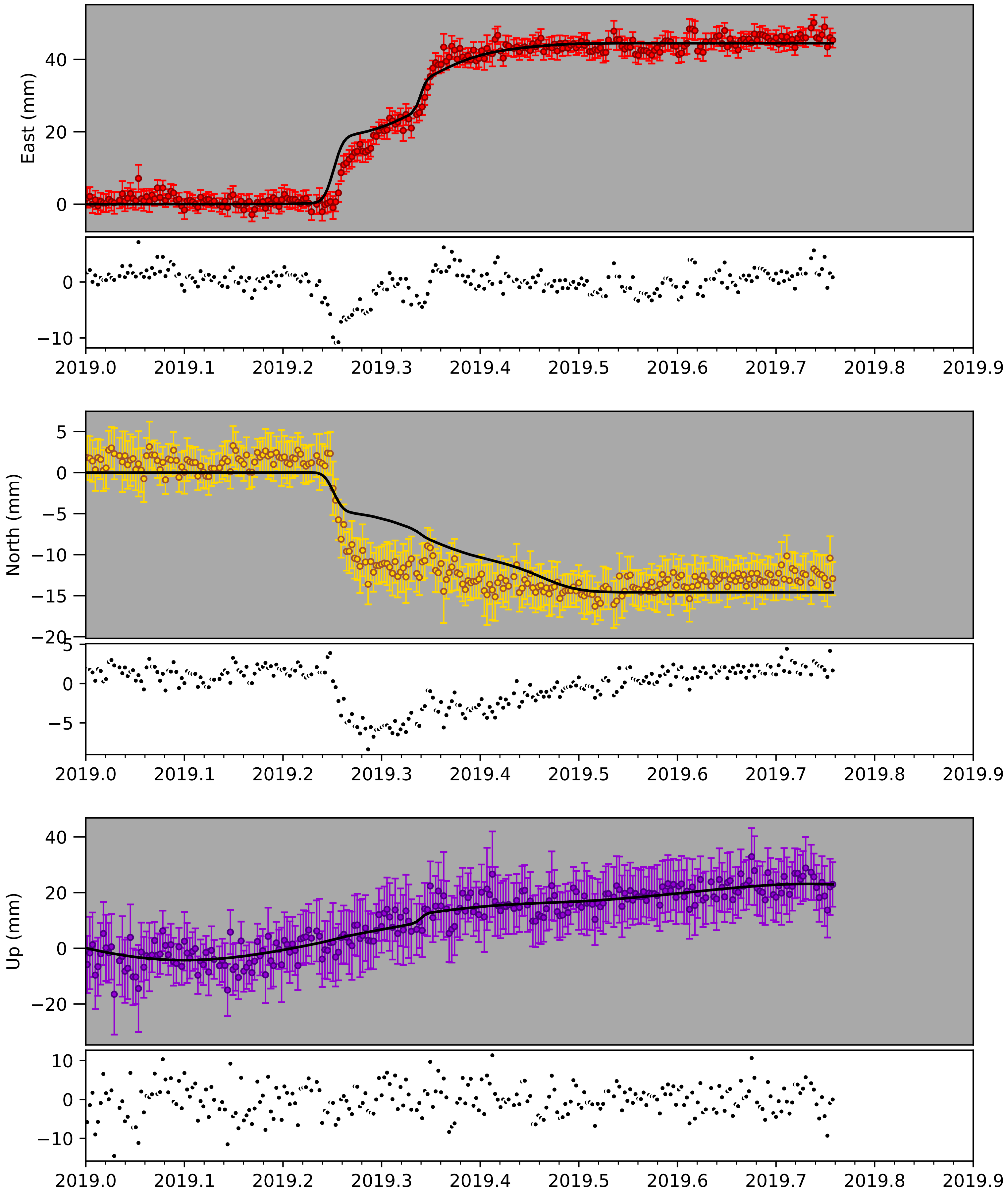

MAKO

[178.1291] [-38.6438]

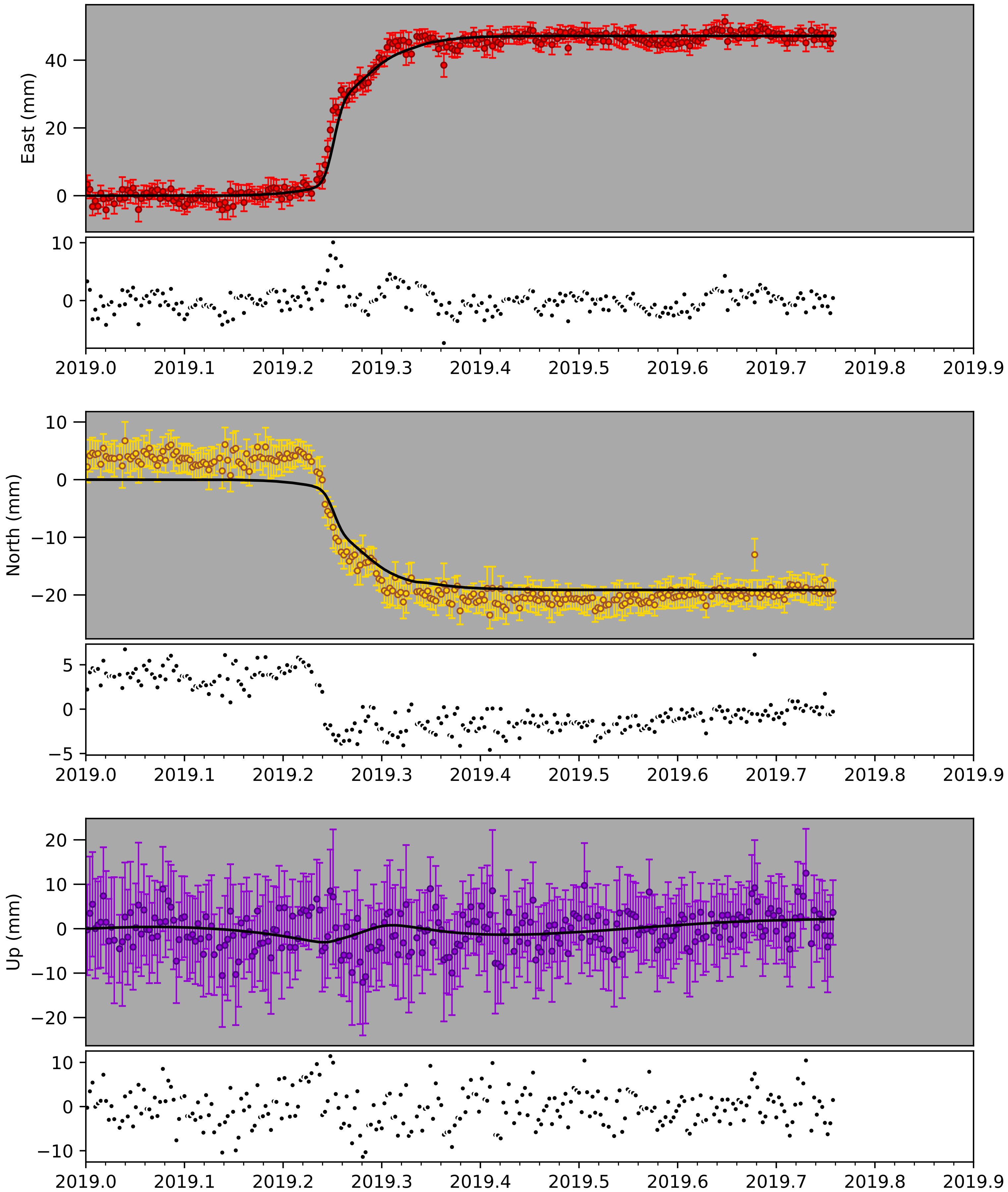

MATW

[177.5262] [-38.3338]

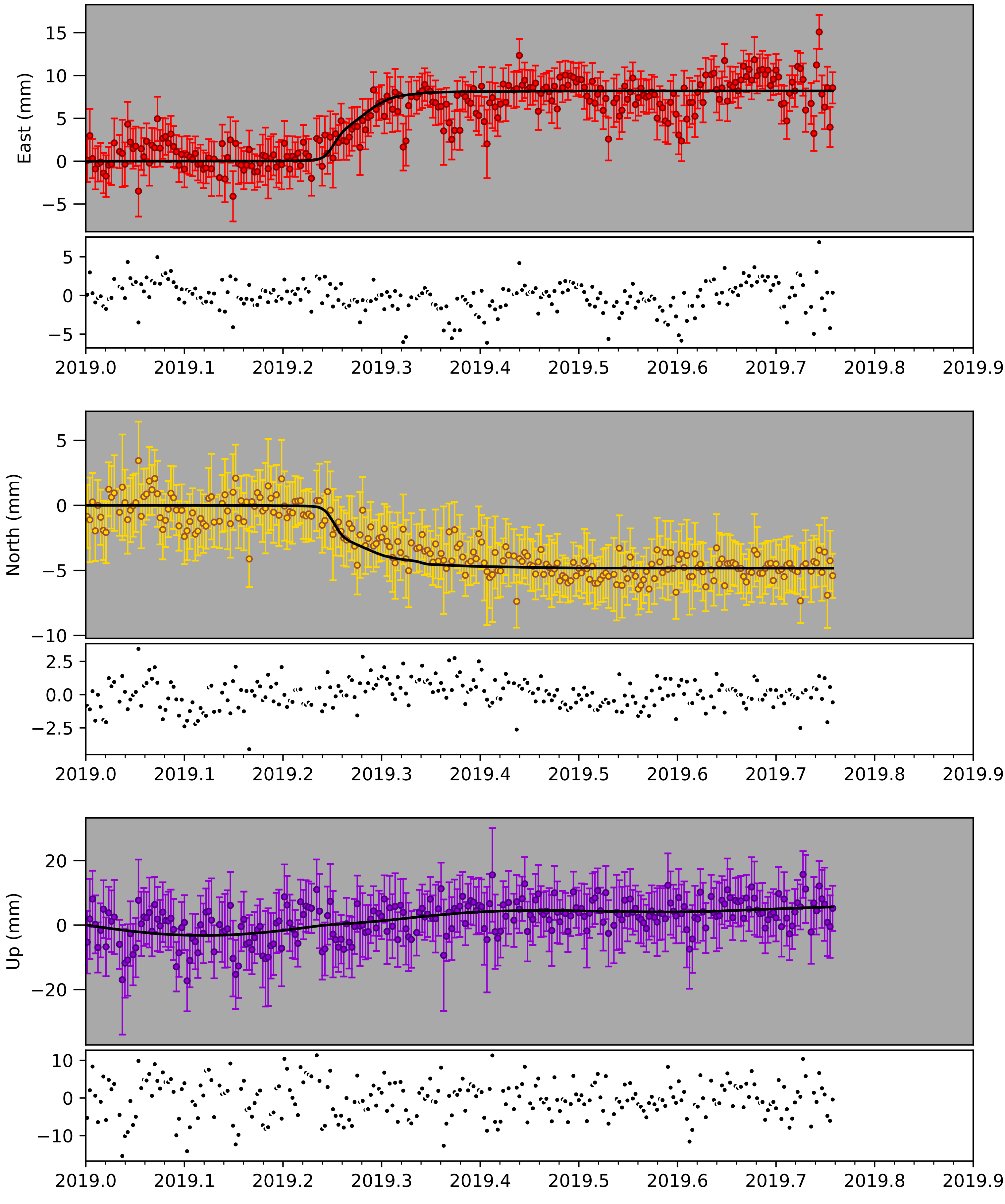

MCNL

[176.6966] [-39.4442]

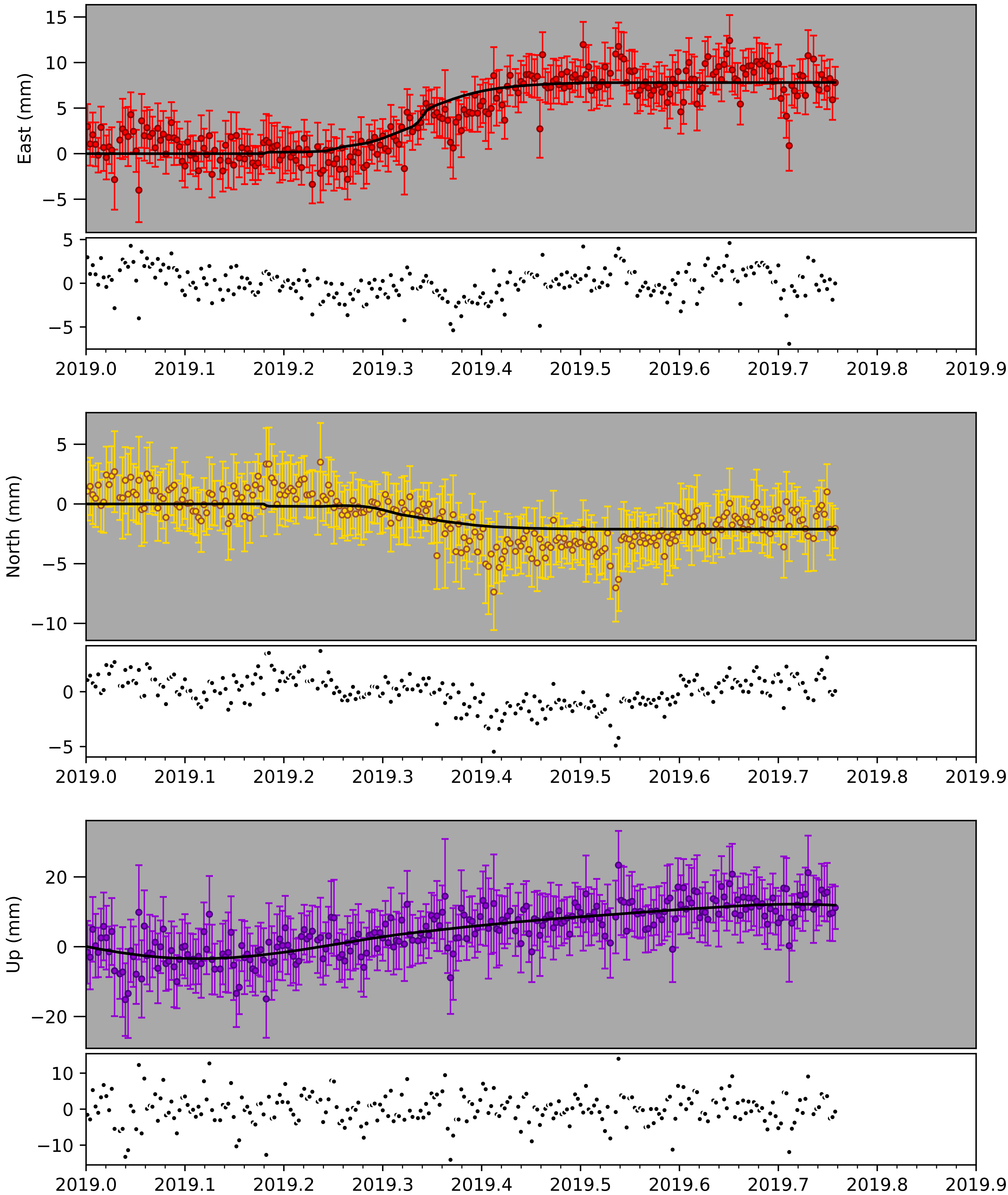

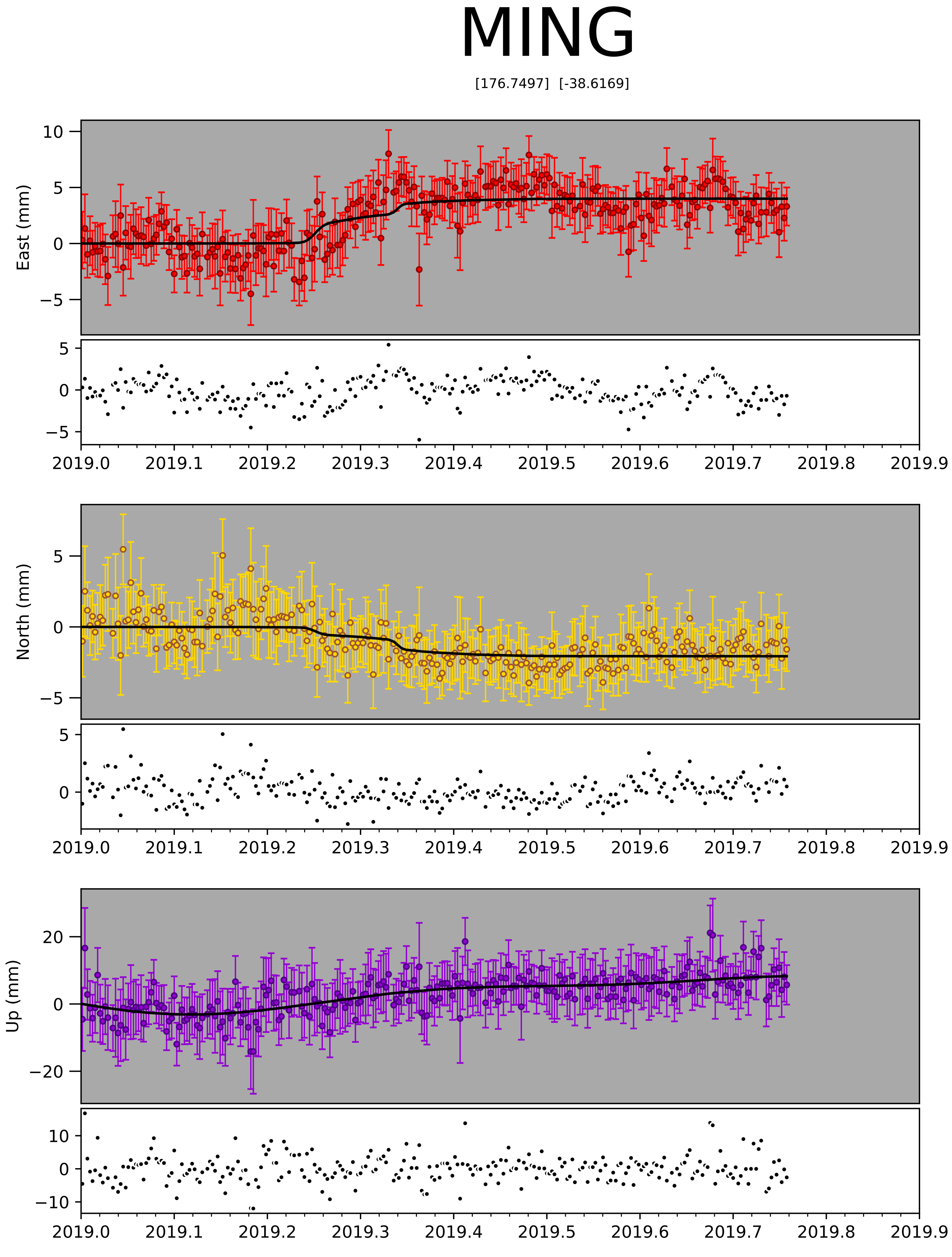
MING
[176.7497] [-38.6169]
East (mm)
North (mm)
Up (mm)
2019.0
2019.1
2019.2
2019.3
2019.4
2019.5
2019.6
2019.7
2019.8
2019.9

MKNO

[176.0288] [-39.7034]

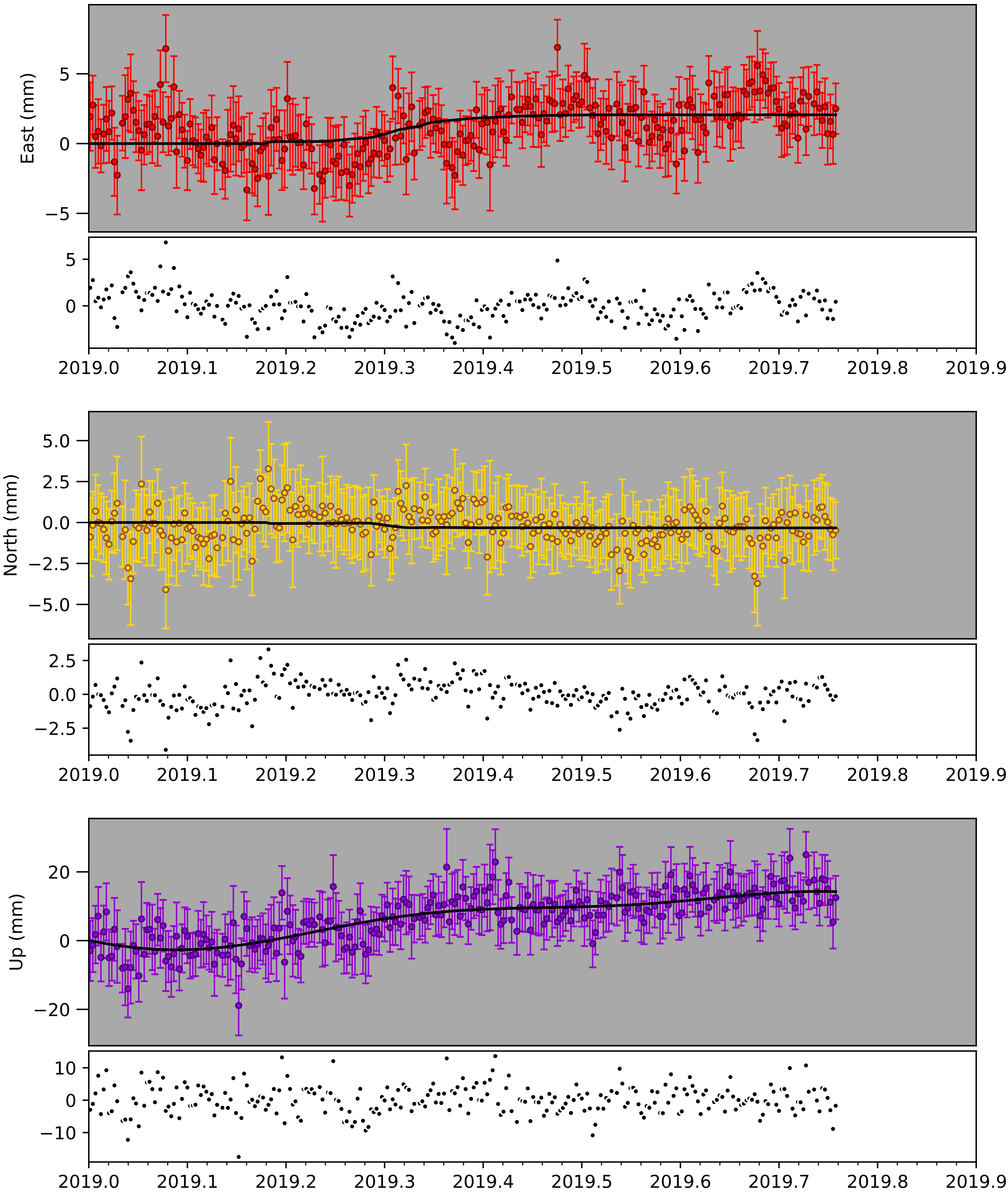

MNHR

[176.2234] [-40.4686]

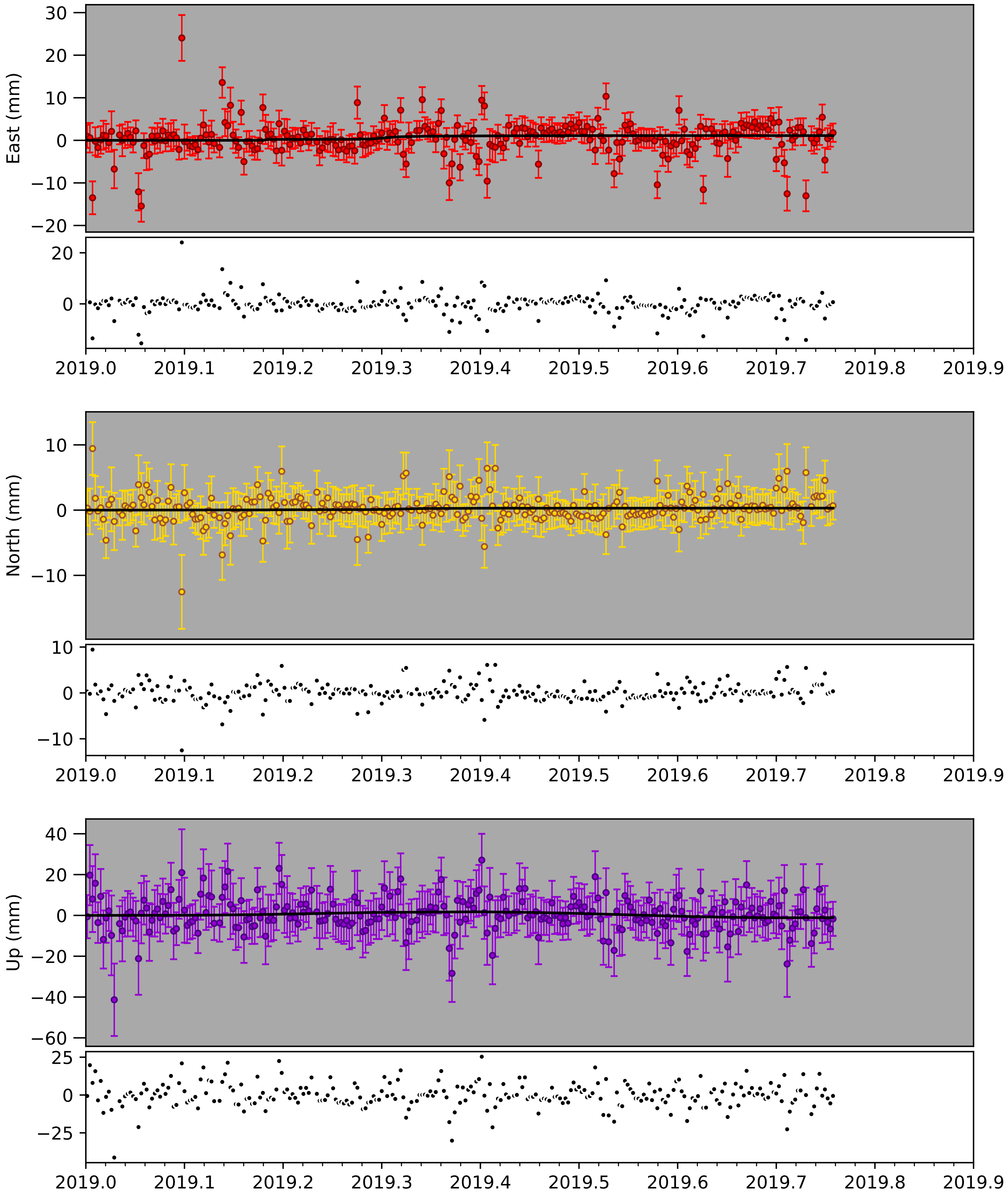

NMAI

[176.8066] [-39.097]

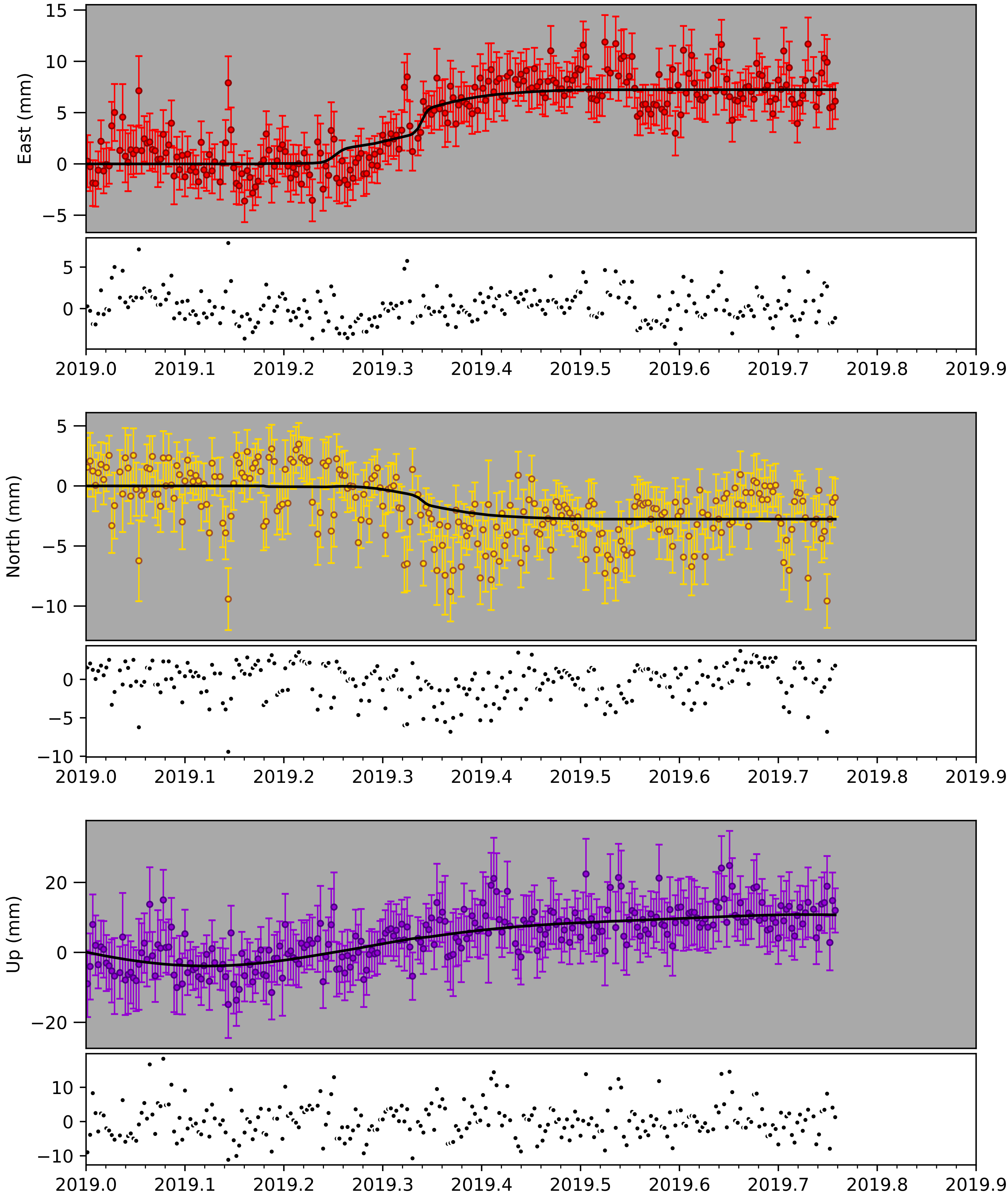

NRSW

[176.2] [-40.1133]

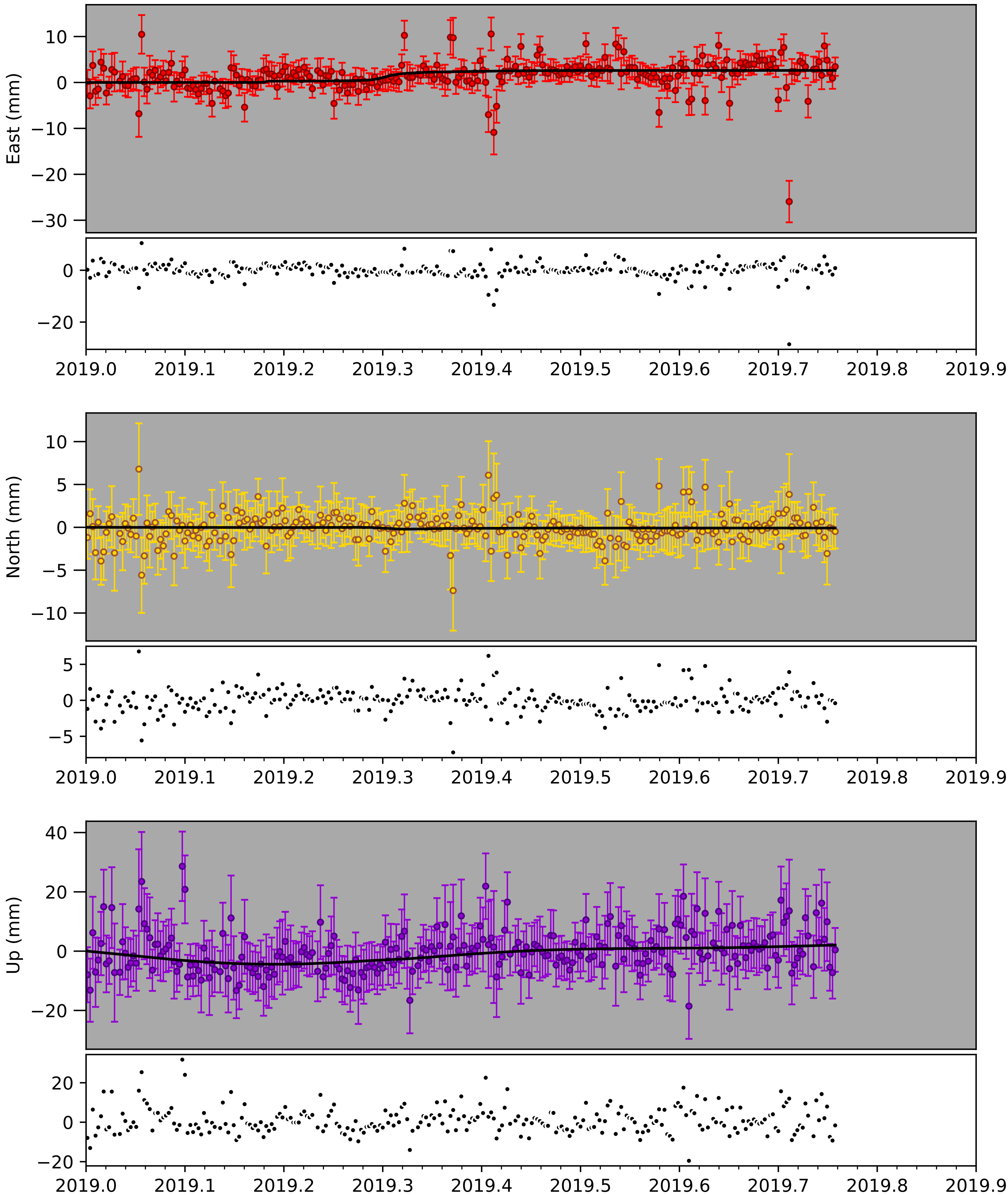

OHIN

[175.7907] [-39.9183]

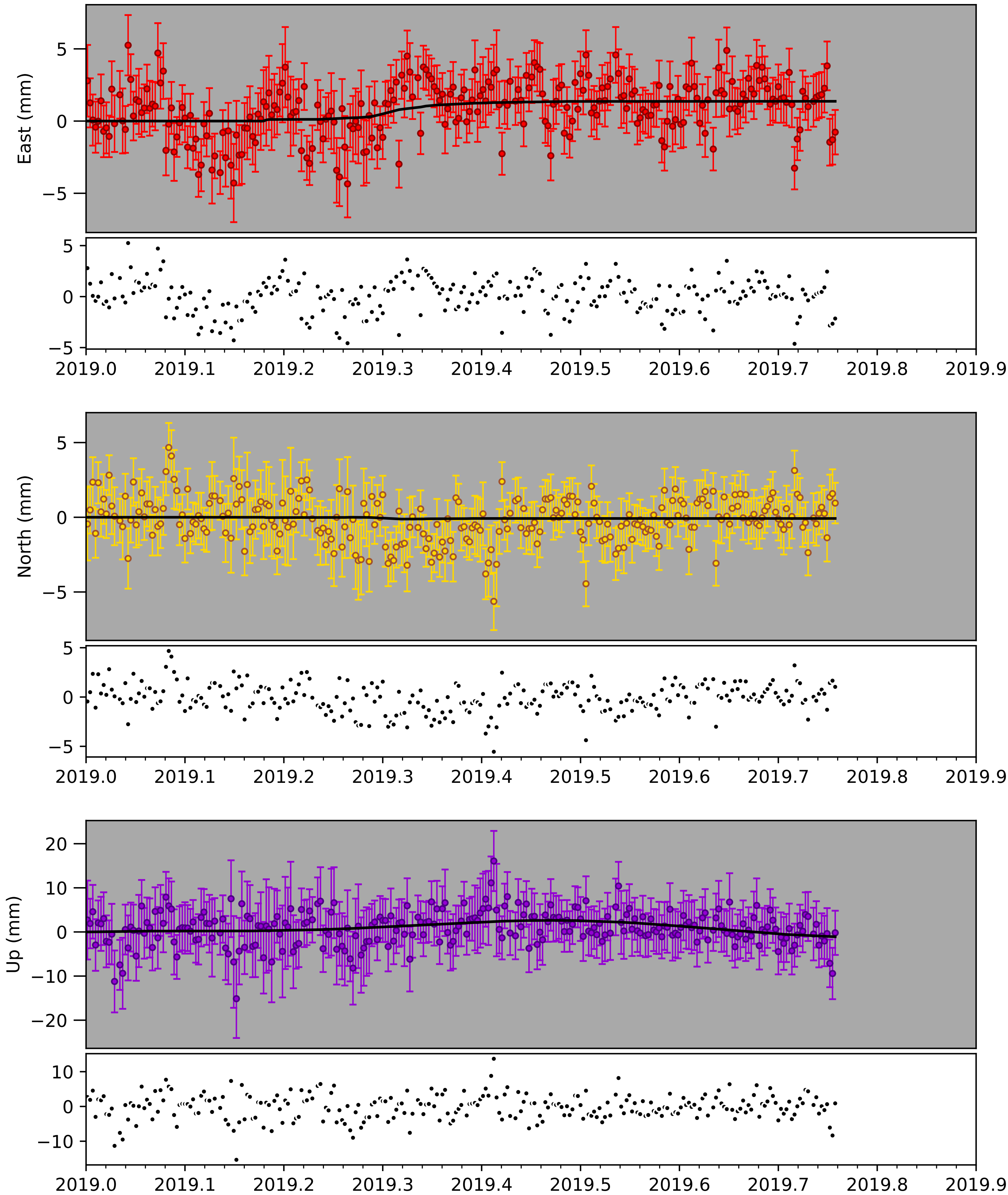

OPTK

[177.3076] [-38.0465]

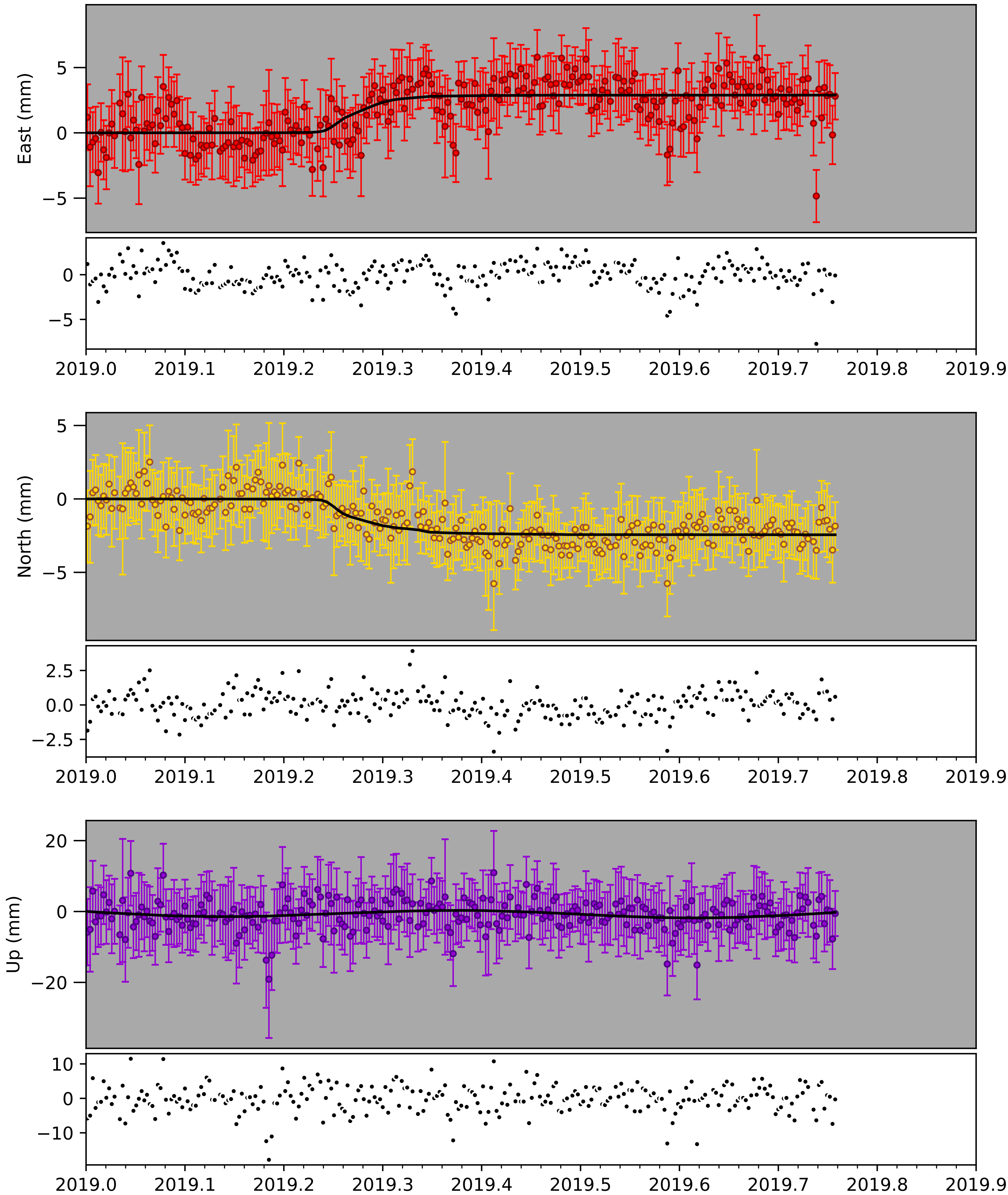

OROA

[176.6807] [-40.1044]

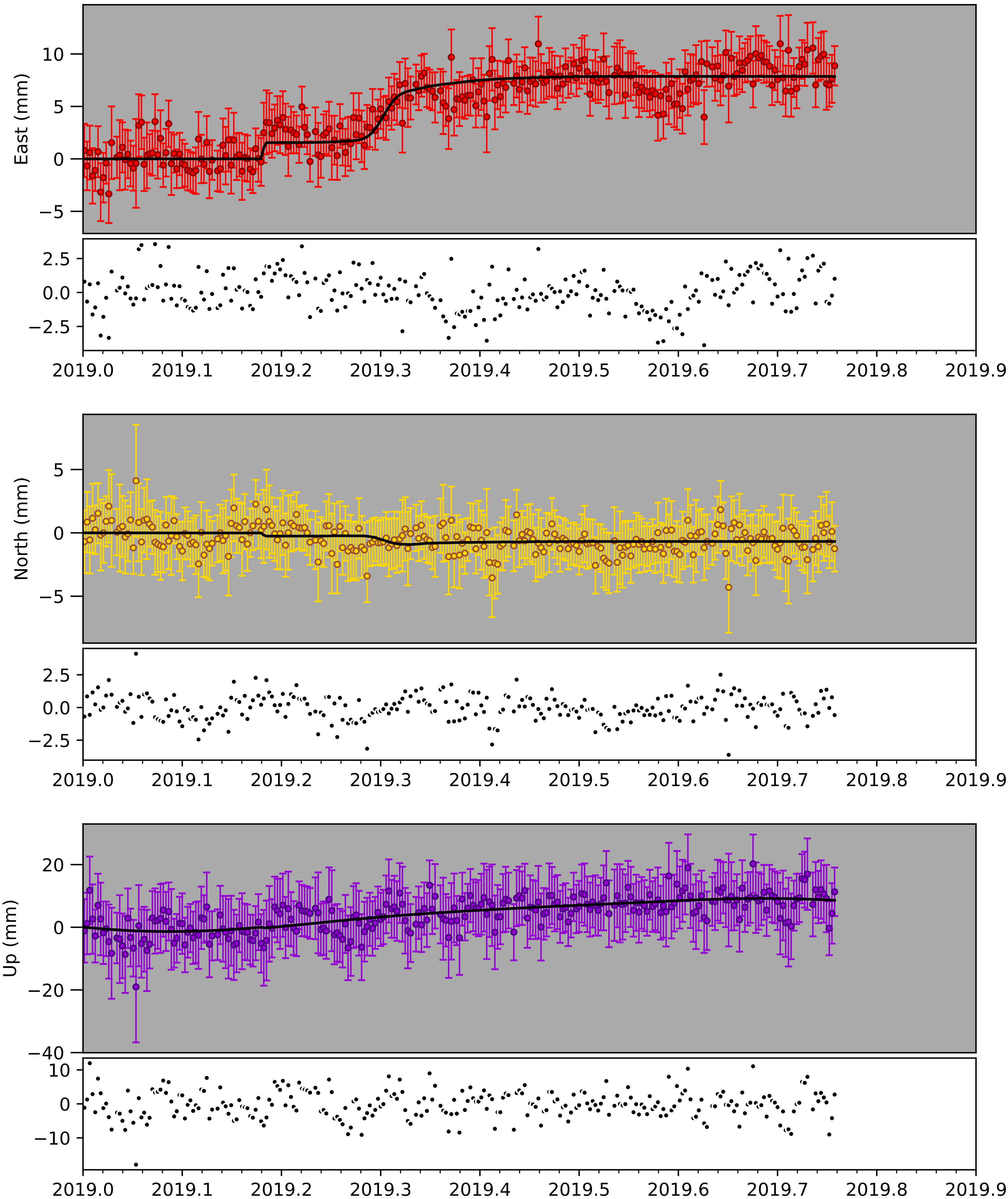

PAKI

[178.0826] [-37.894]

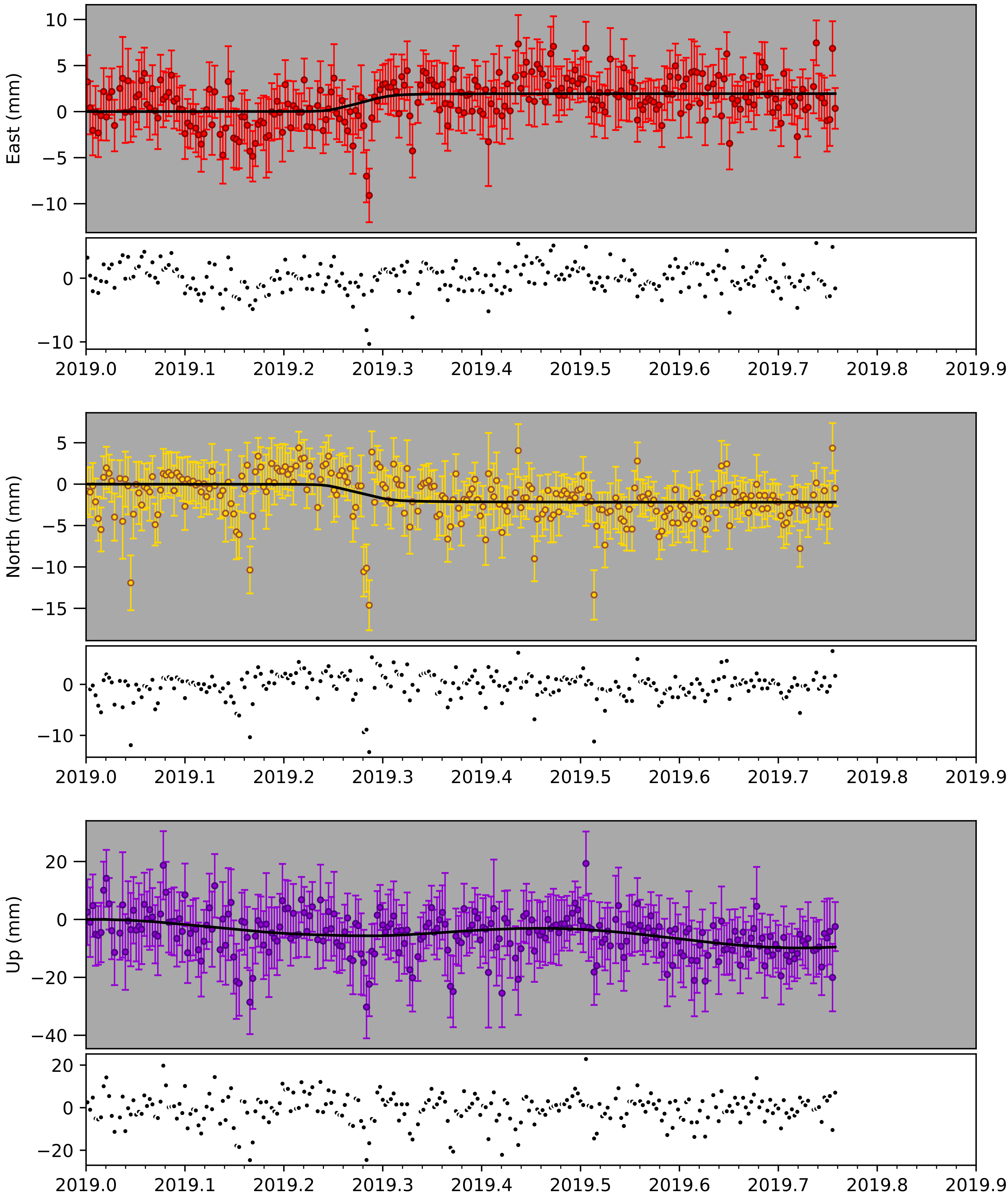

PARI

[177.8833] [-38.9226]

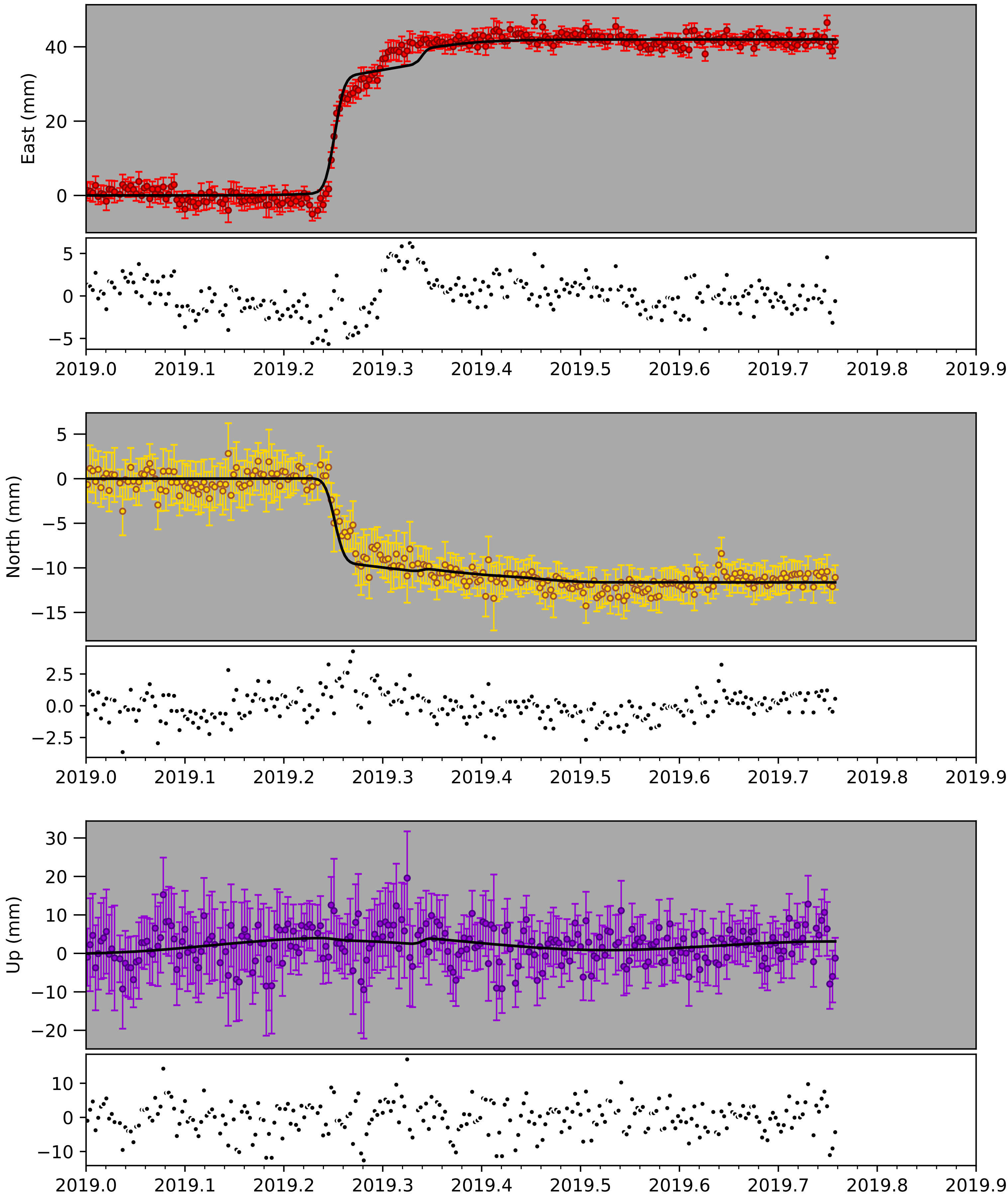

PAWA

[176.8639] [-40.0331]

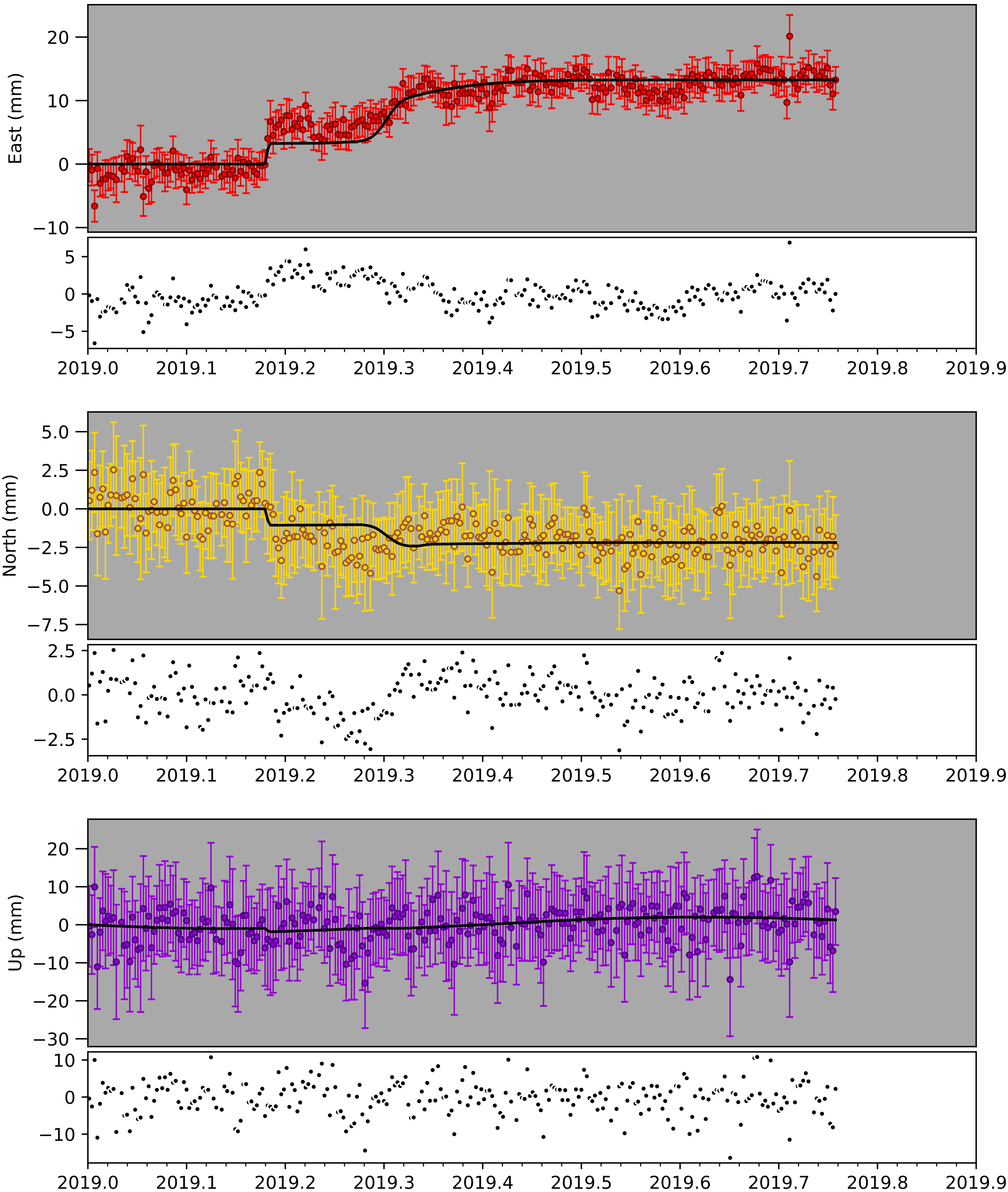

PBS1

[177.9184] [-39.8516]

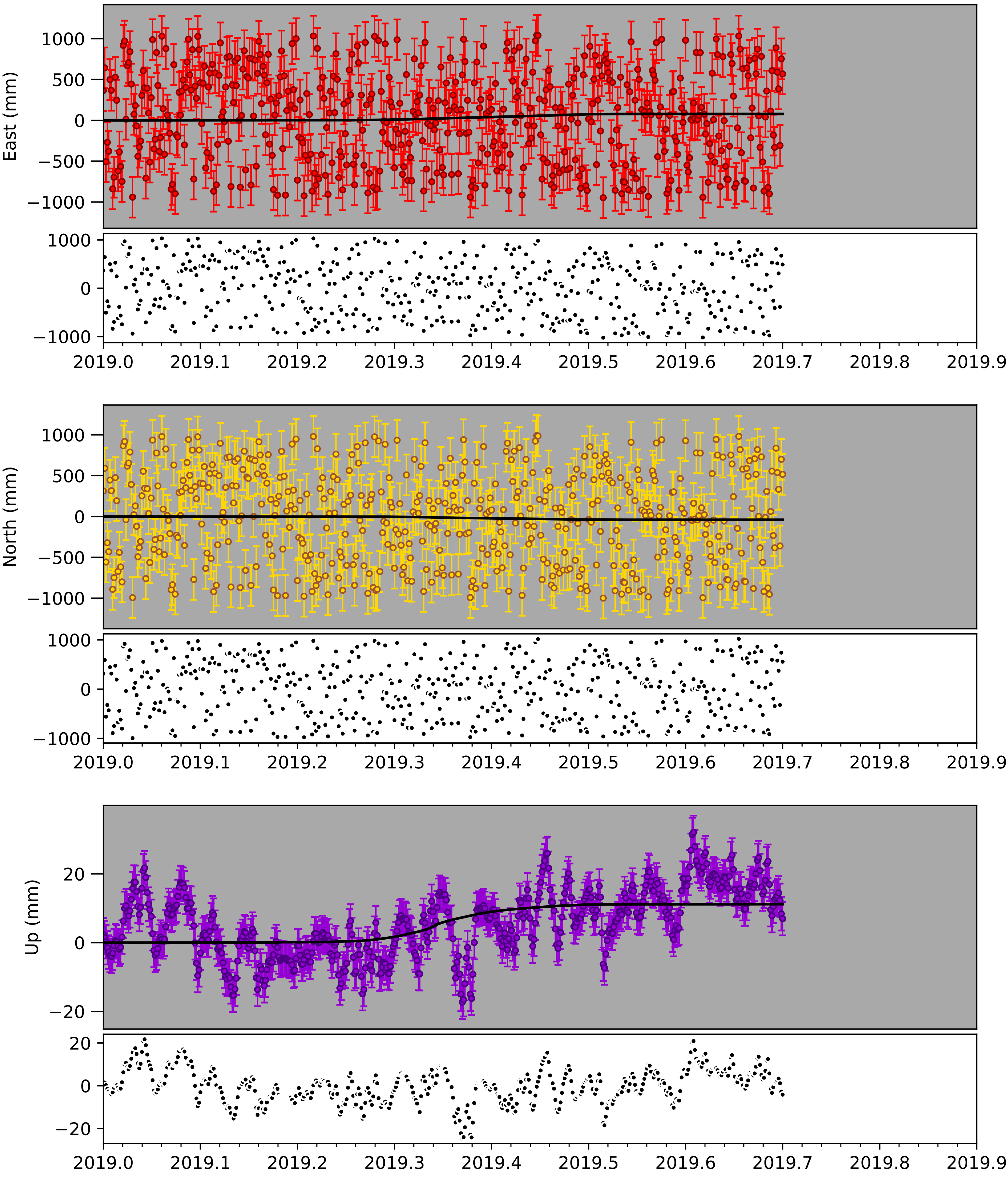

PBS2

[178.0876] [-39.8923]

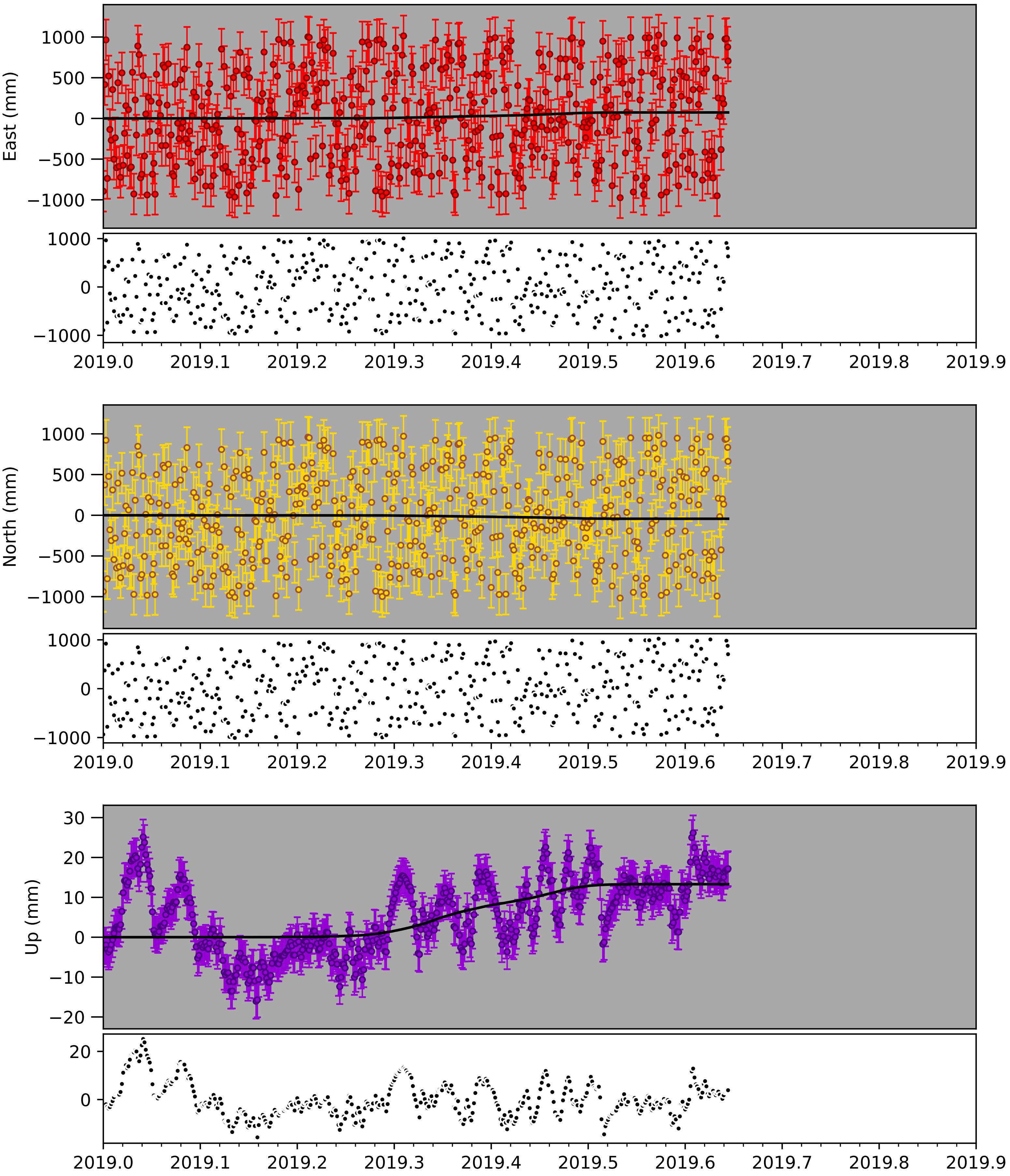

PBS3

[178.3524] [-39.9195]

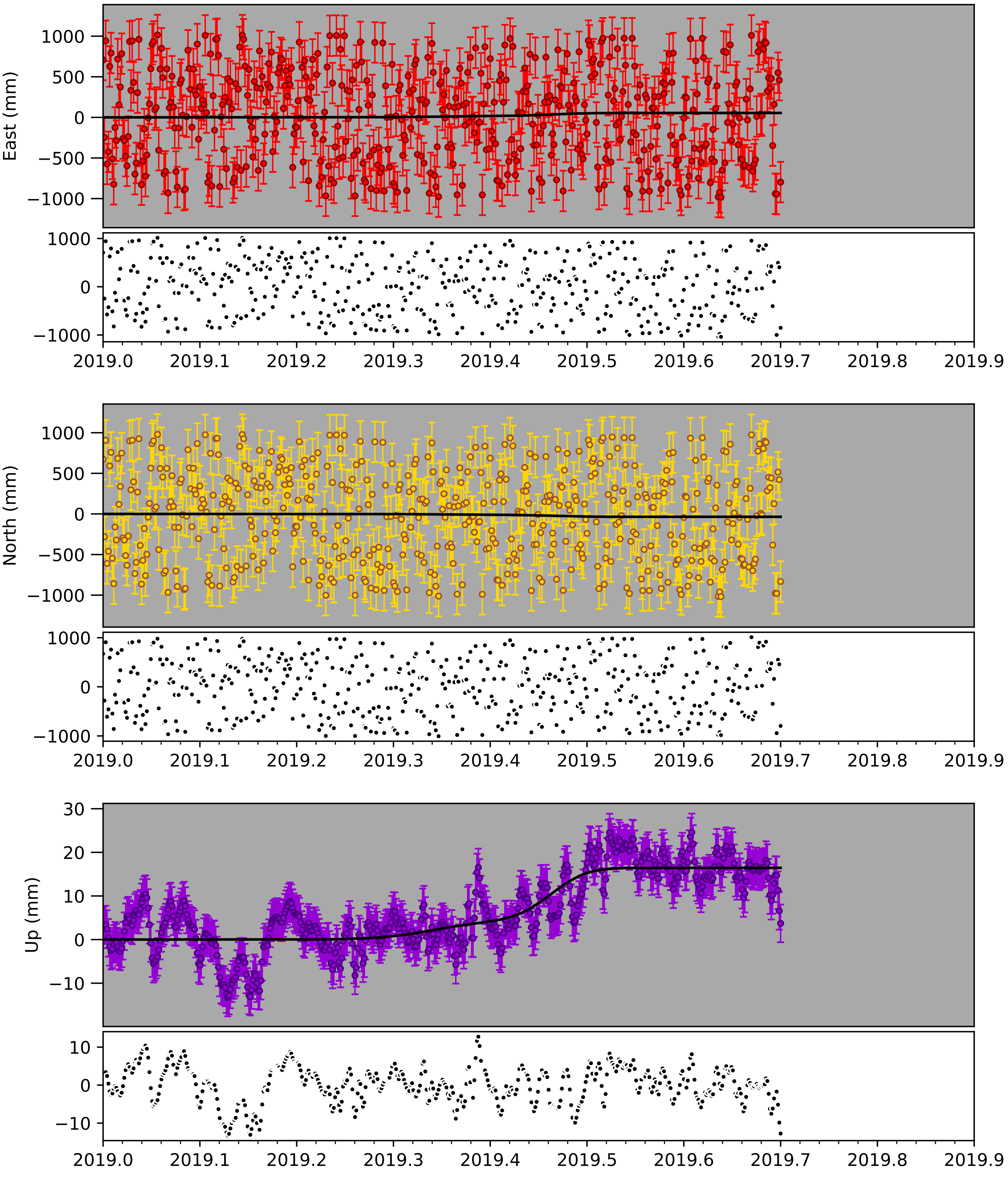

PNUI

[176.2005] [-39.9168]

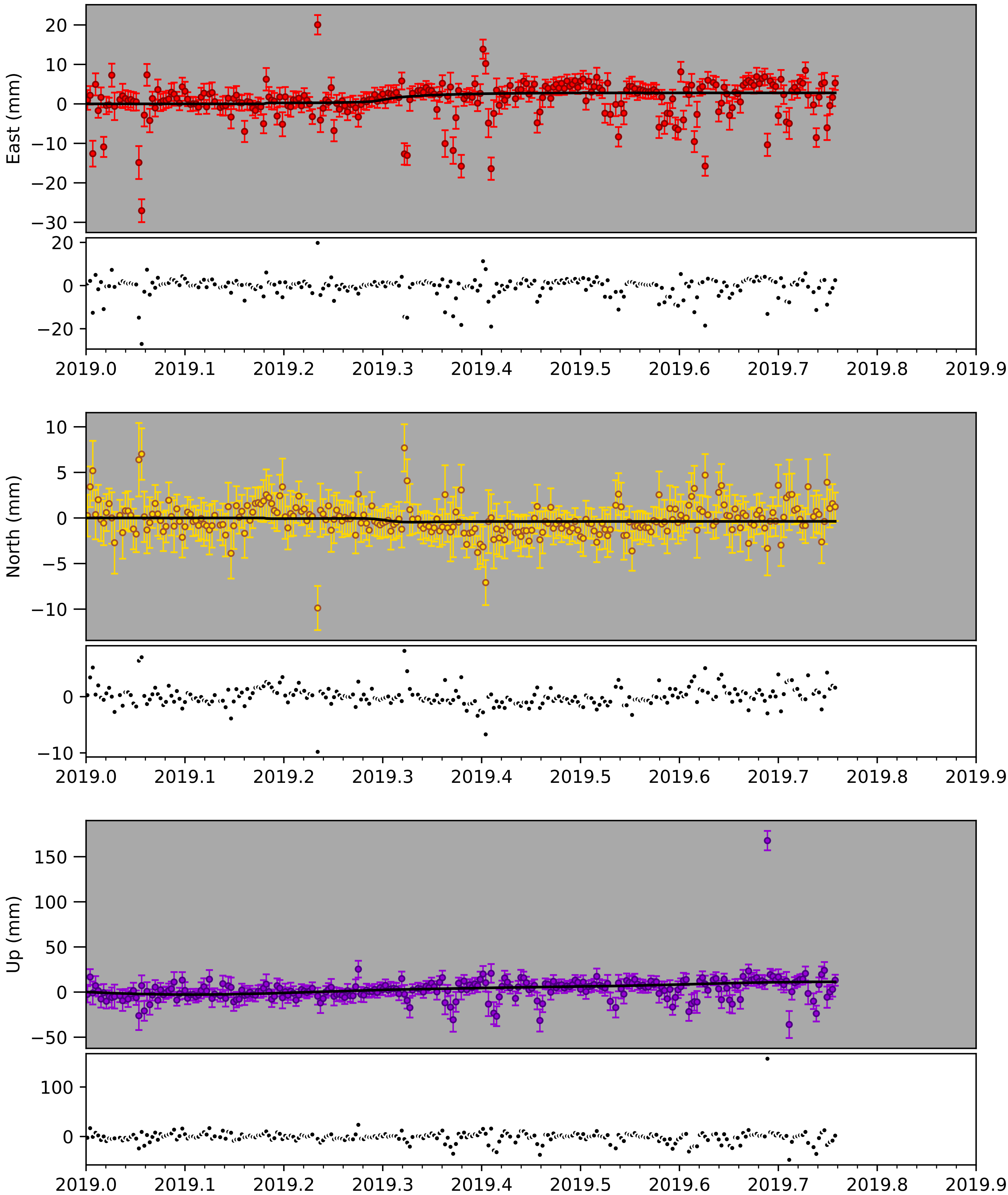

PORA

[176.6352] [-40.2664]

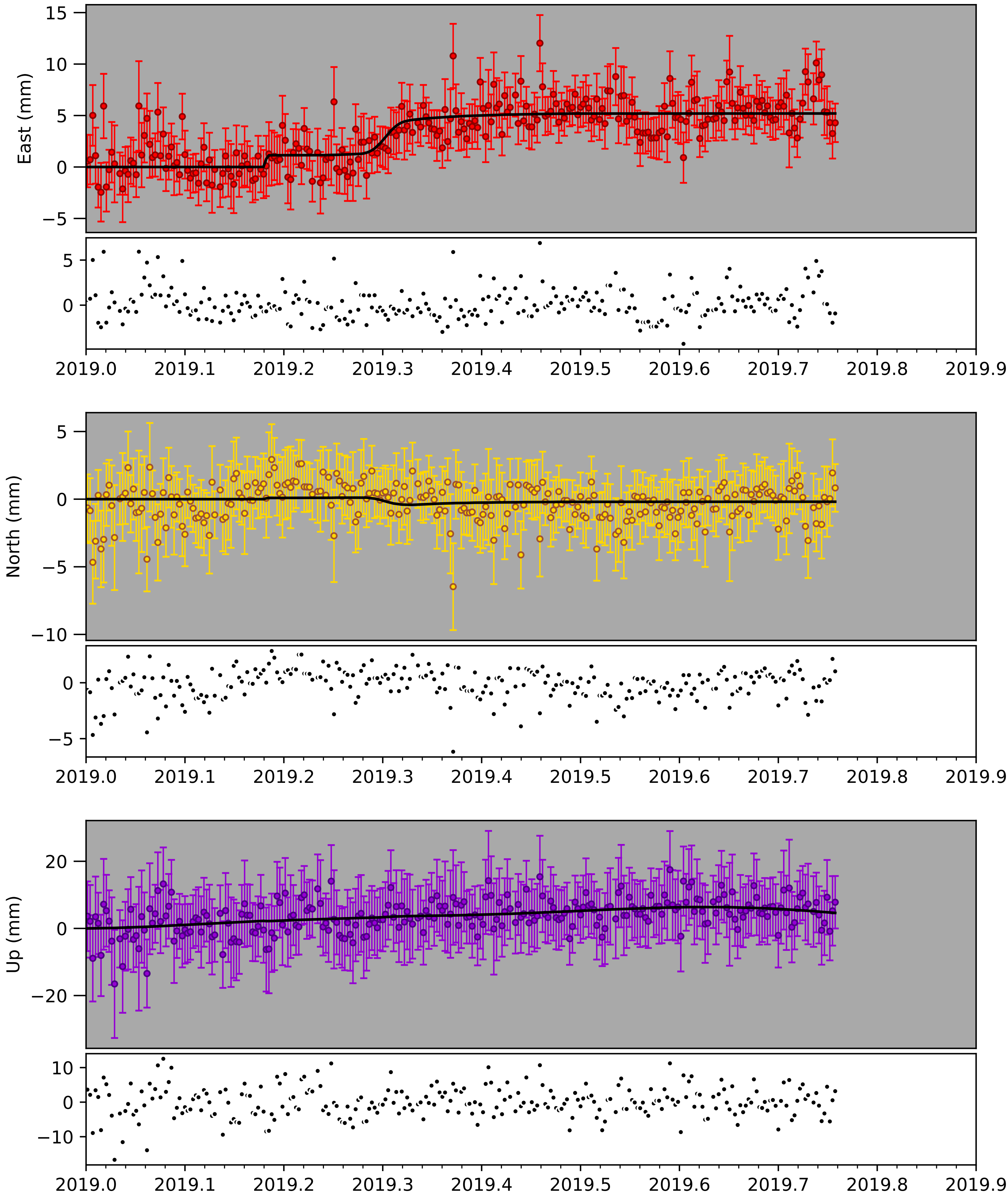

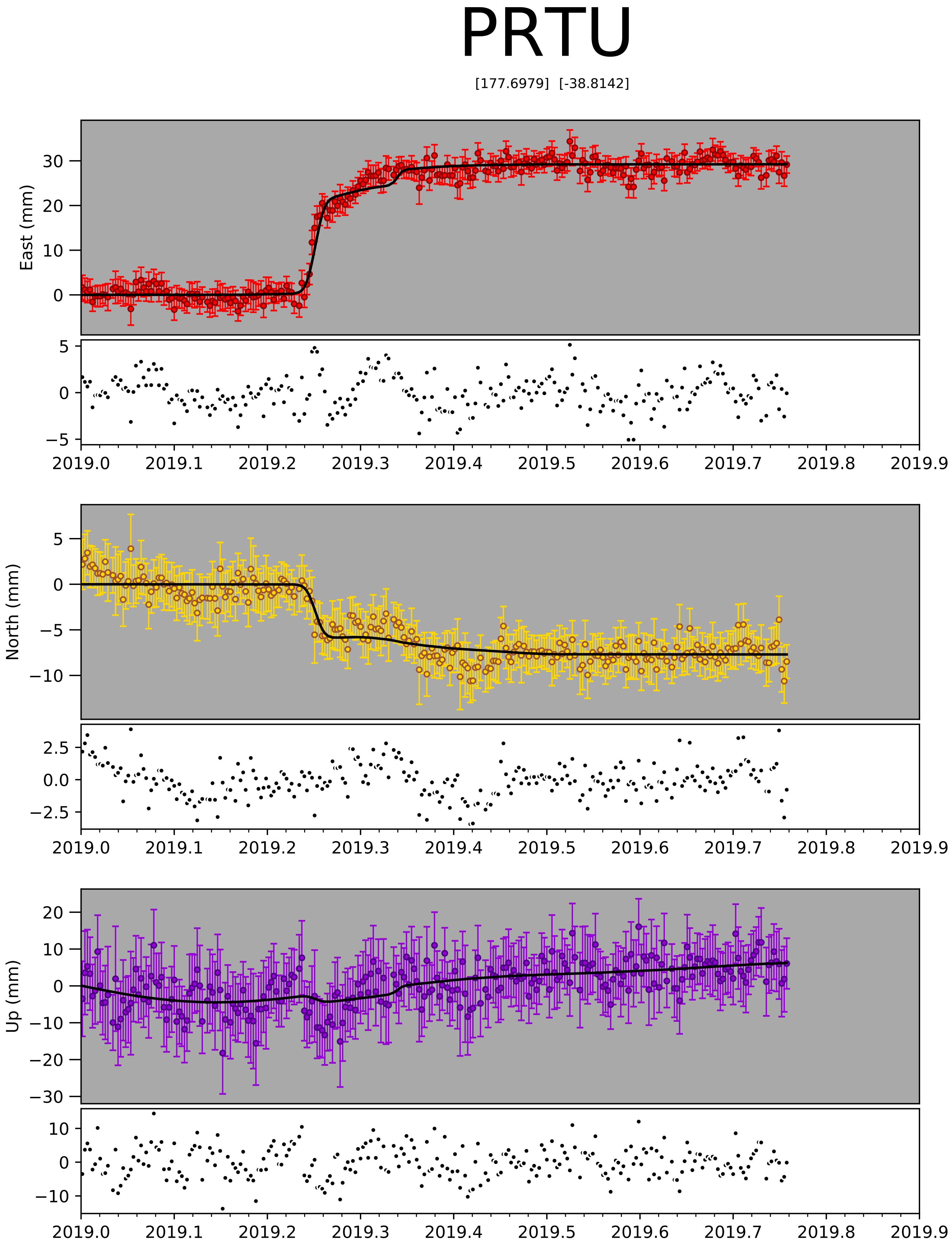
PRTU
[177.6979] [-38.8142]
East (mm)
North (mm)
Up (mm)
2019.0
2019.1
2019.2
2019.3
2019.4
2019.5
2019.6
2019.7
2019.8
2019.9

PTOI

[175.9993] [-40.6011]

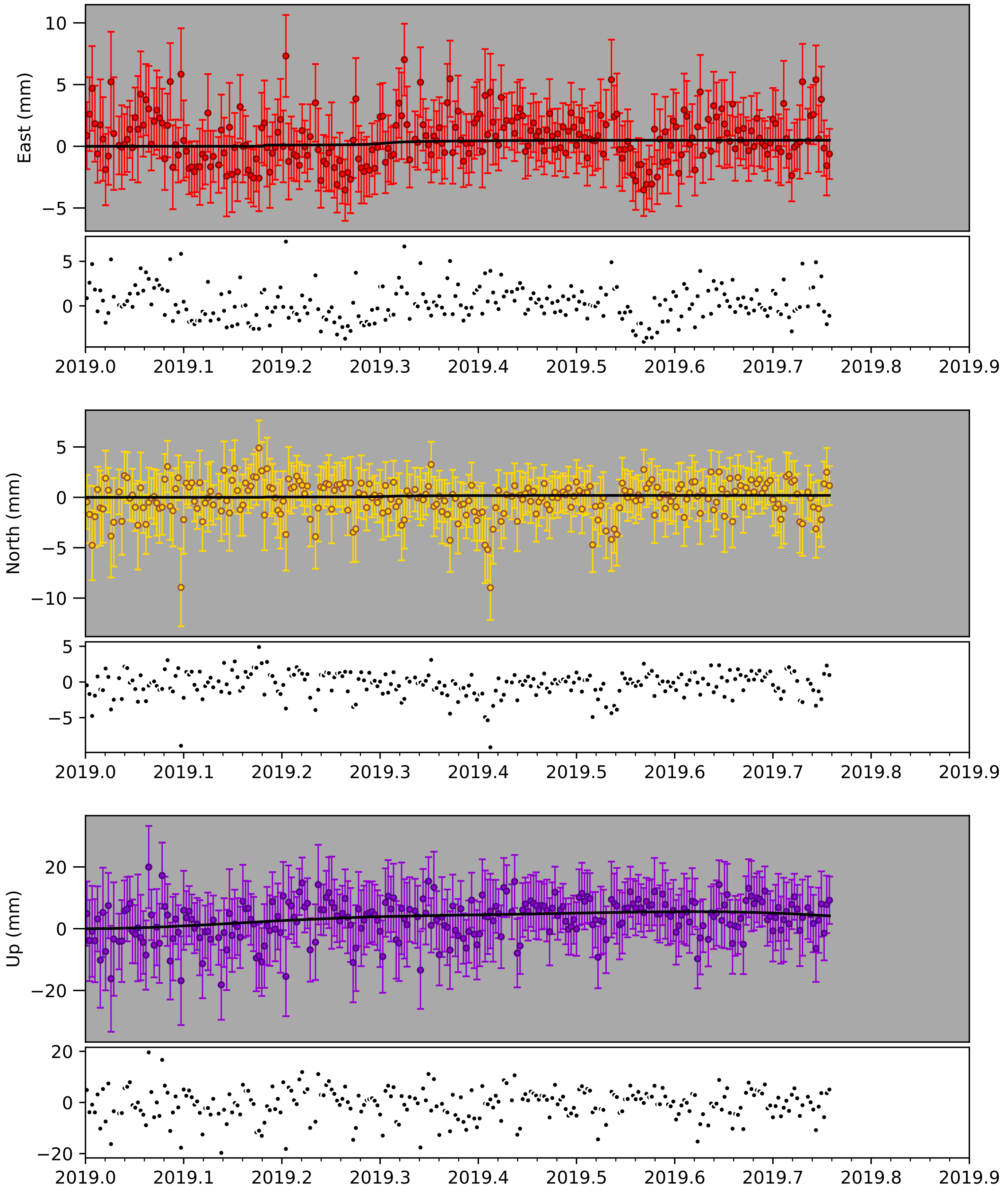

PUKE

[178.2574] [-38.0714]

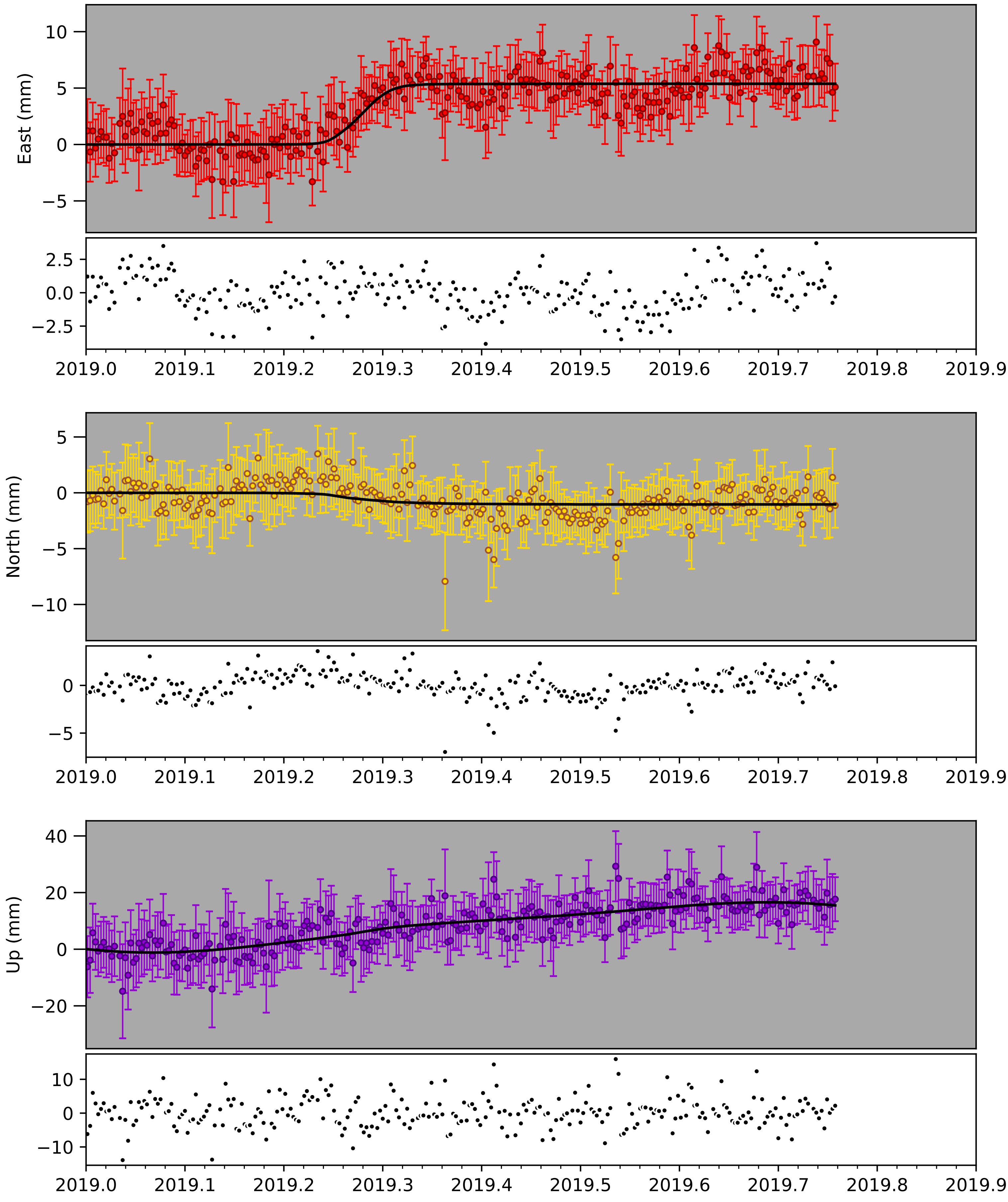

RAHI

[177.0861] [-38.9162]

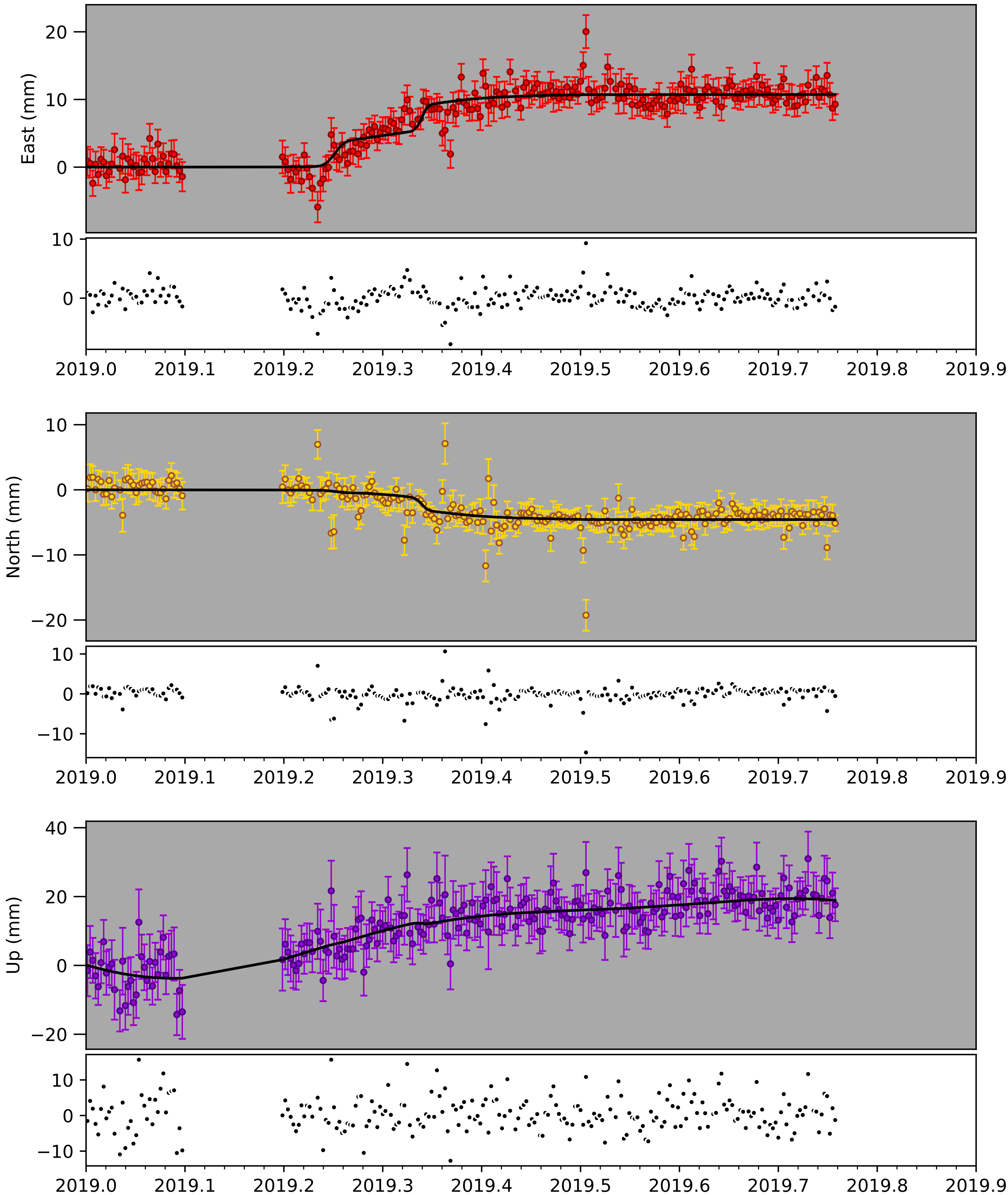

RAKW

[176.6212] [-39.7472]

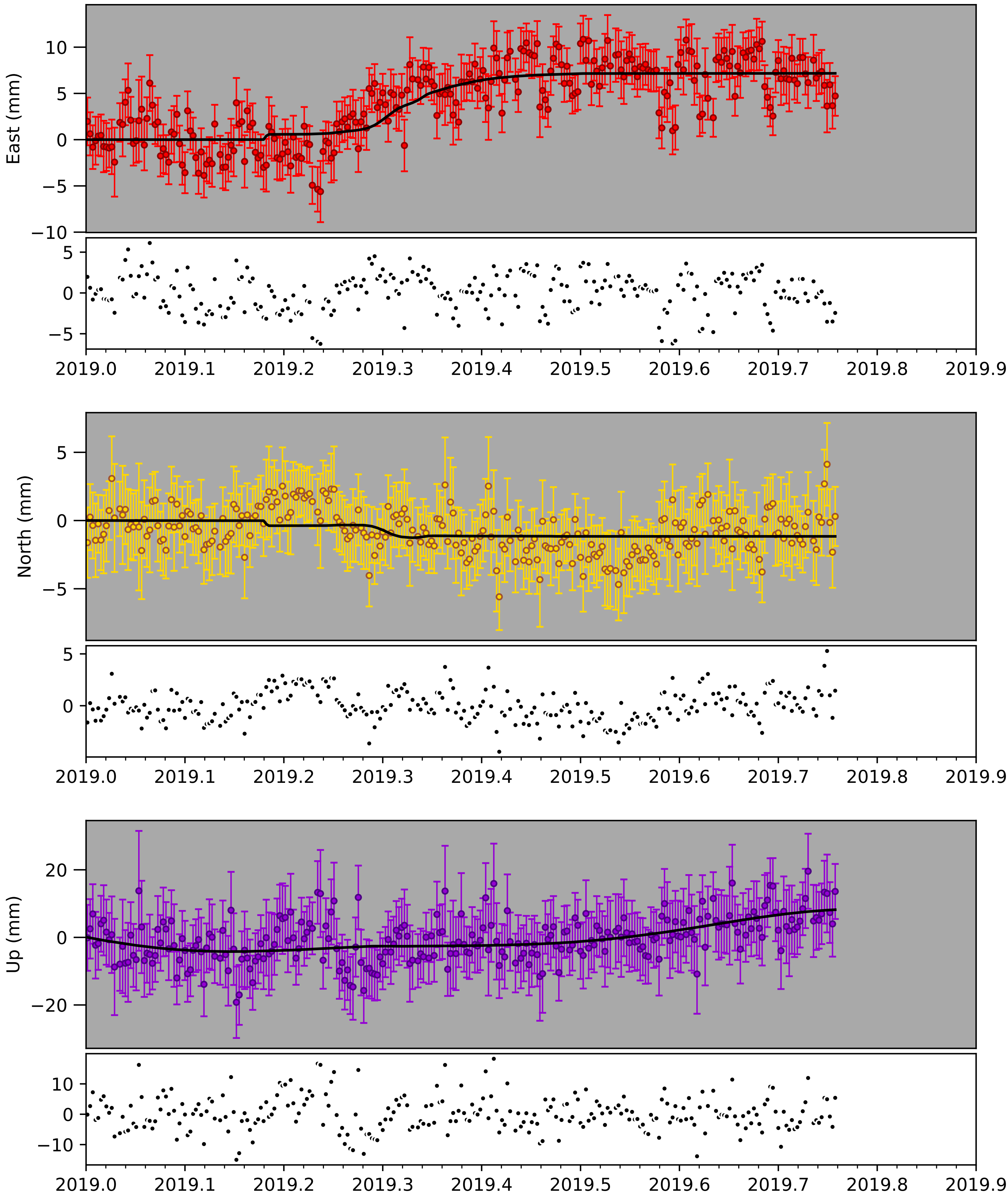

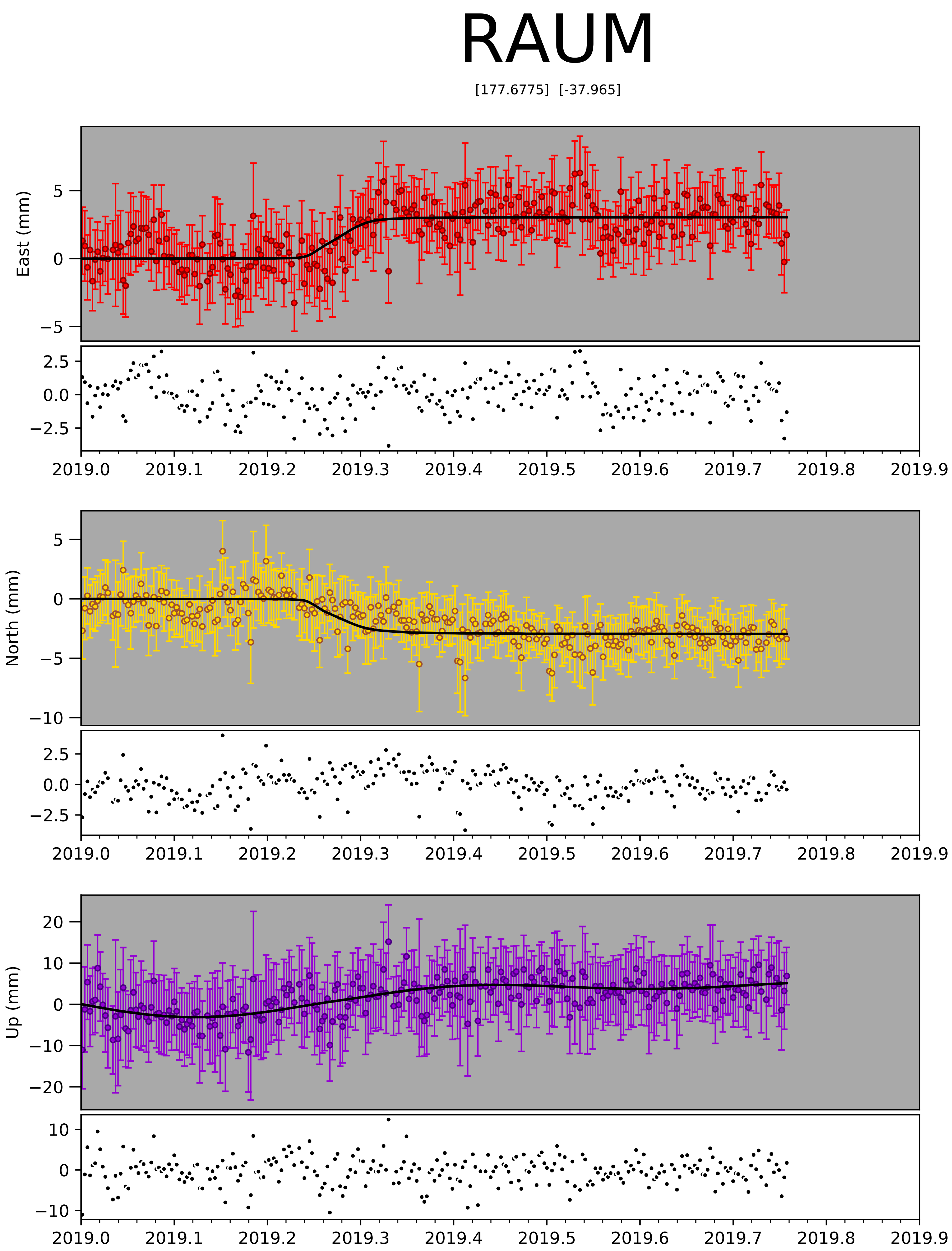
RAUM
[177.6775] [-37.965]
East (mm)
North (mm)
Up (mm)
2019.0
2019.1
2019.2
2019.3
2019.4
2019.5
2019.6
2019.7
2019.8
2019.9

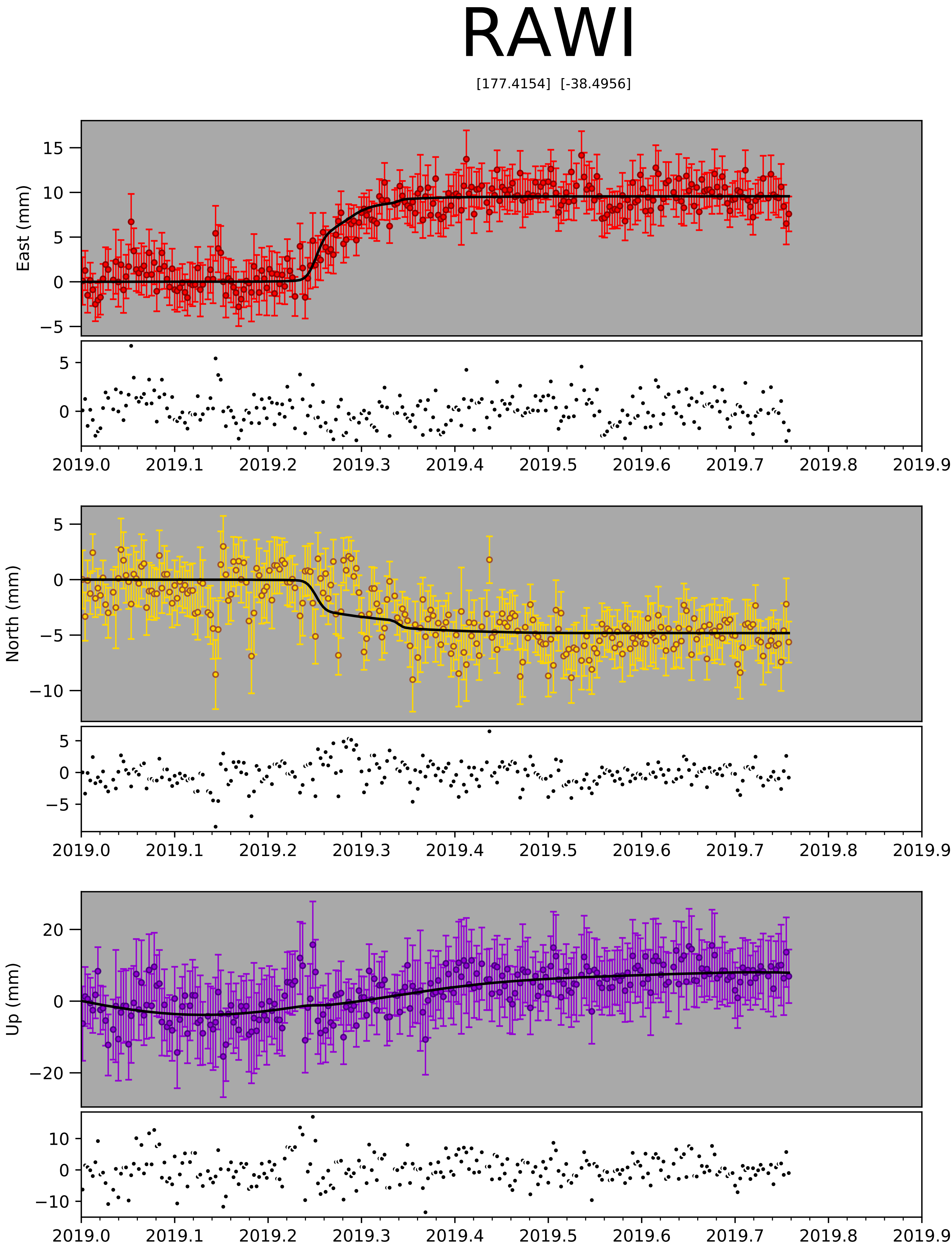

RAWI
[177.4154] [-38.4956]
East (mm)
North (mm)
Up (mm)
2019.0
2019.1
2019.2
2019.3
2019.4
2019.5
2019.6
2019.7
2019.8
2019.9

RGAW

[176.8962] [-38.0032]

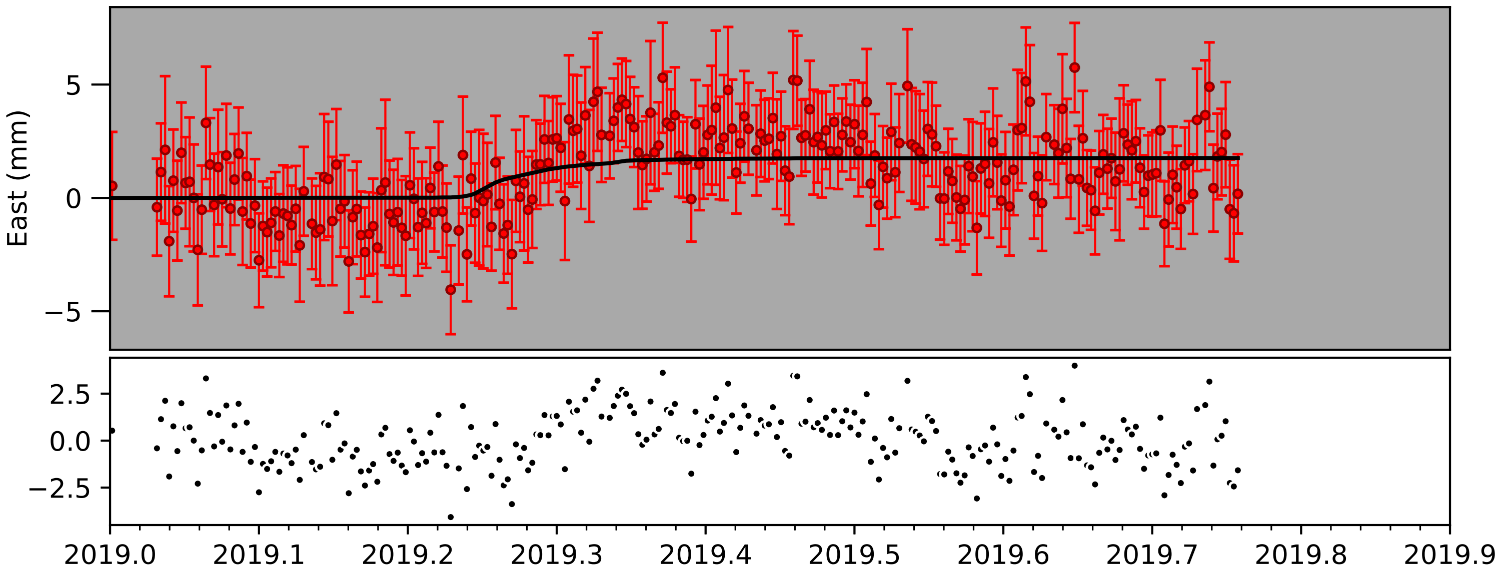

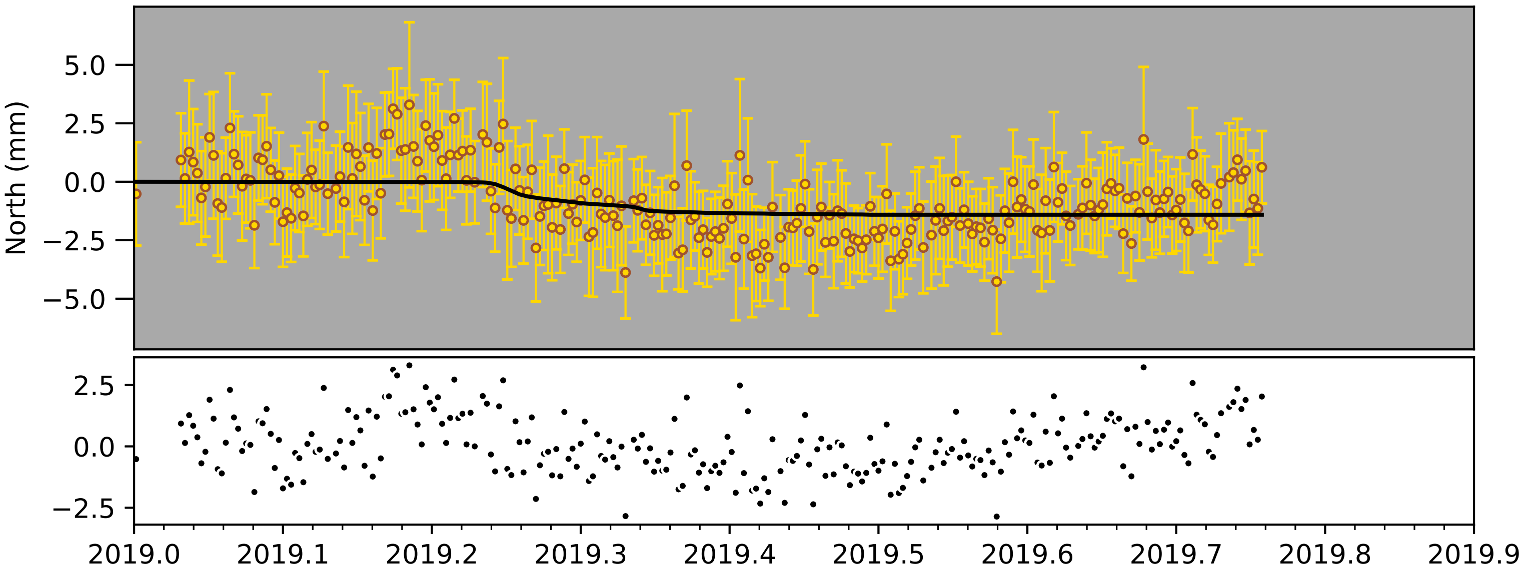

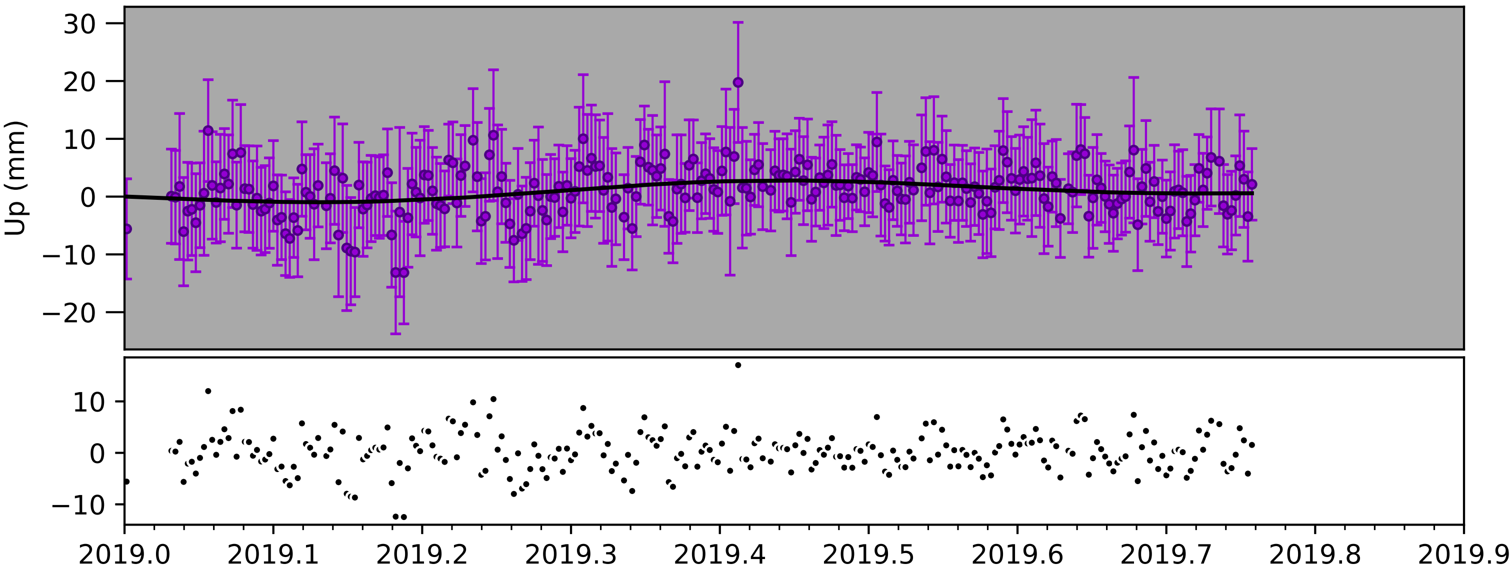

RGRR

[176.5146] [-38.3389]

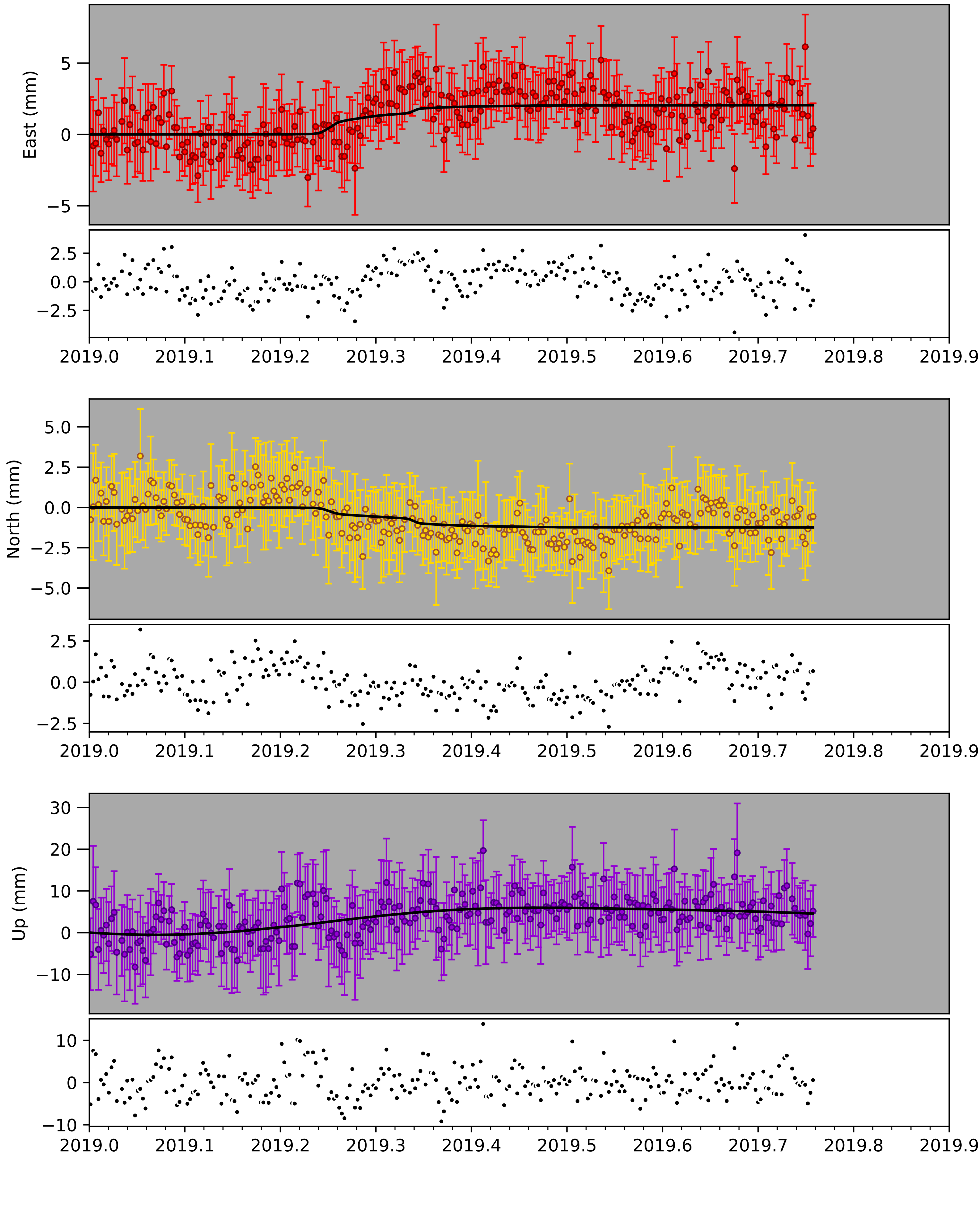

RIPA

[176.4925] [-39.1655]

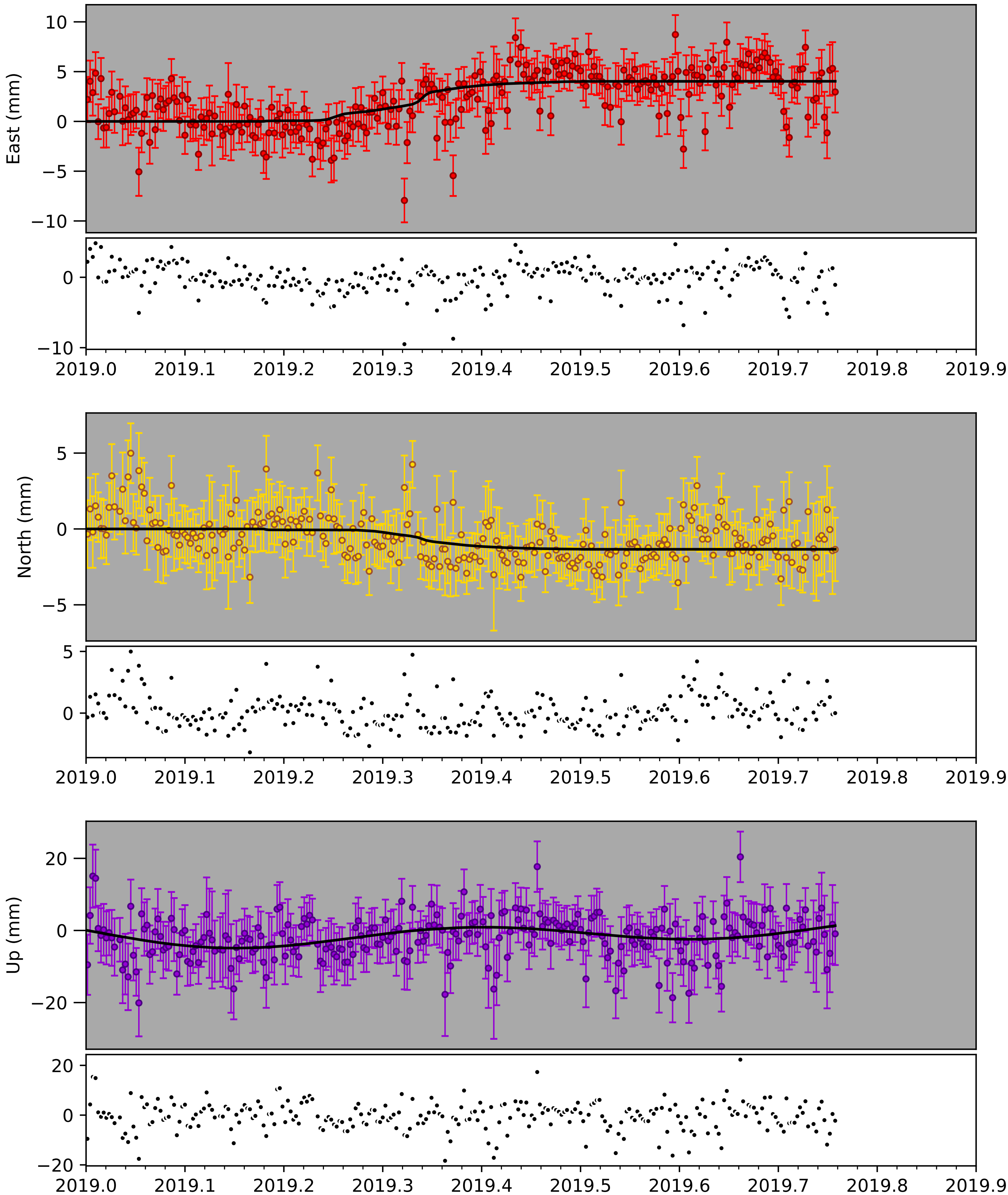

SNST

[177.3475] [-38.7796]

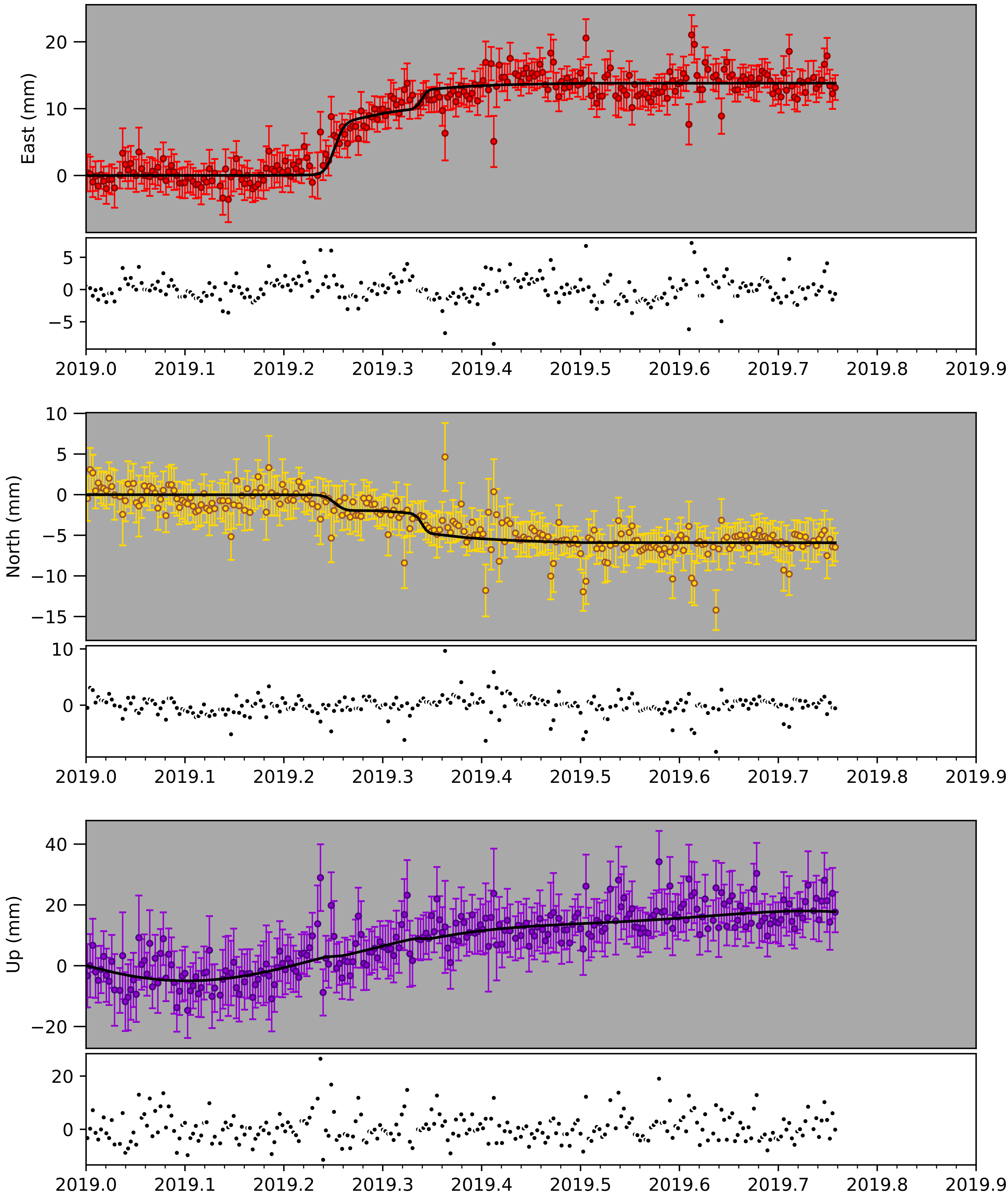

TAKP

[175.9629] [-40.0616]

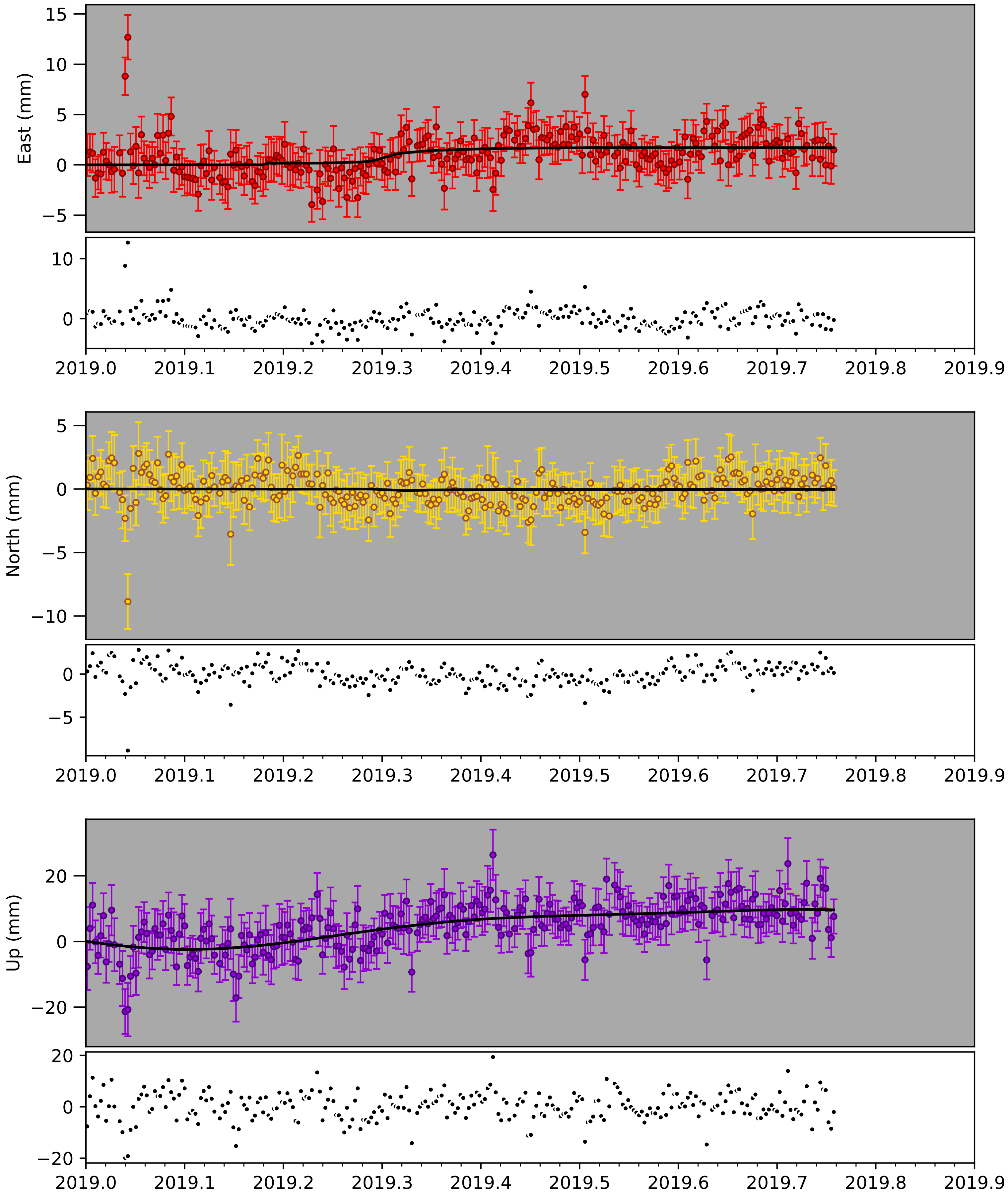

TAUP

[176.081] [-38.7427]

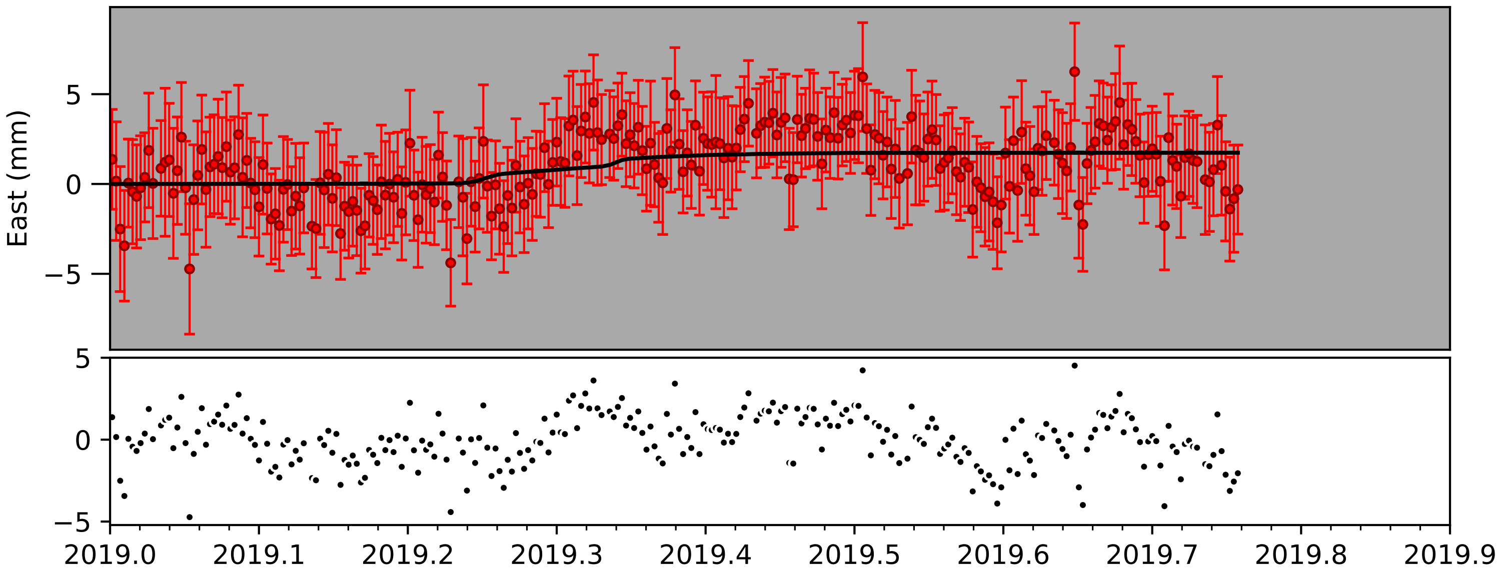

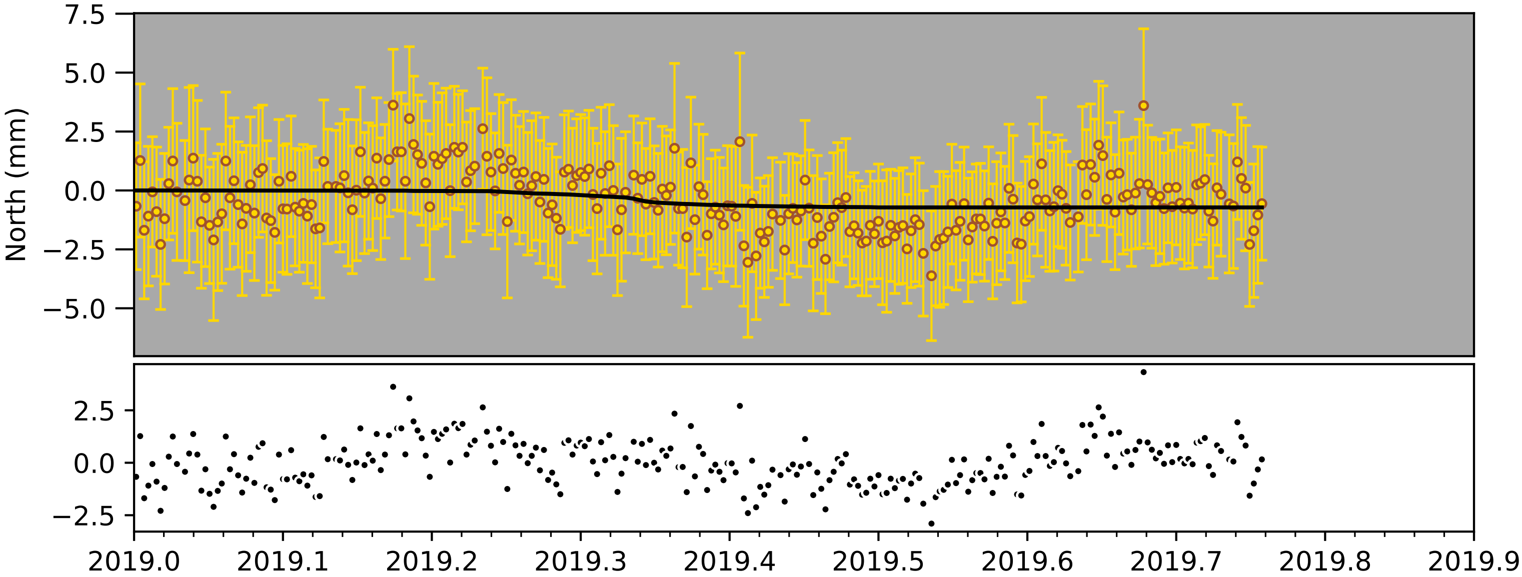

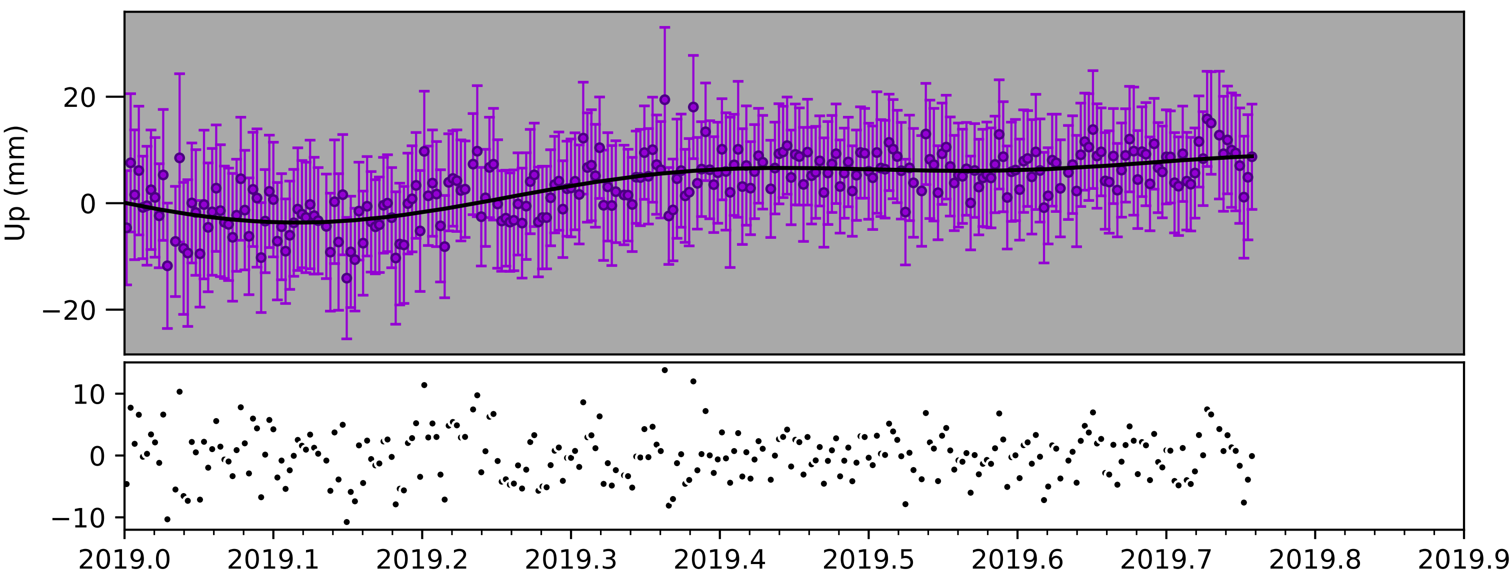

TAUW

[178.0059] [-38.1624]

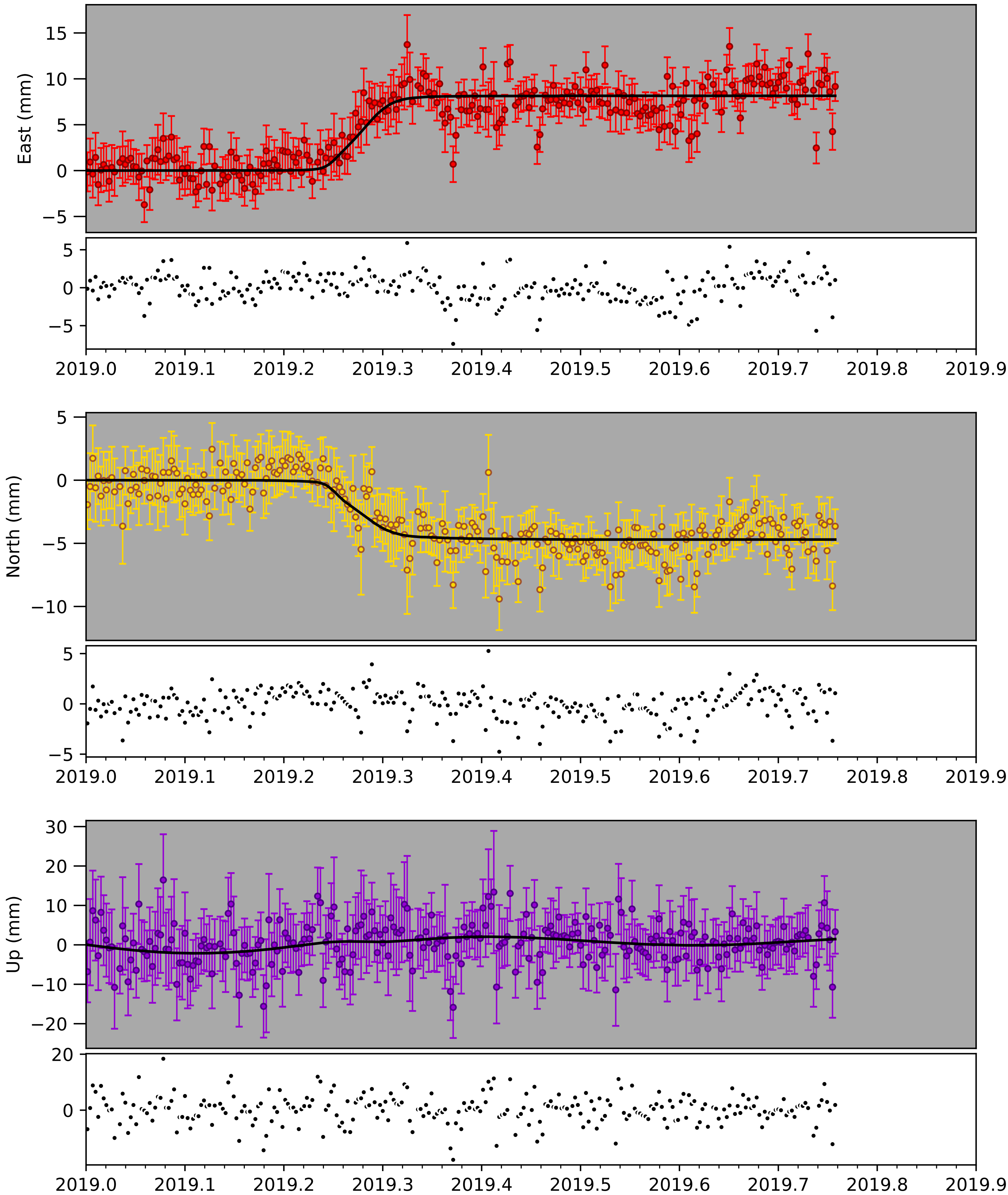

TEMA

[175.8905] [-41.1066]

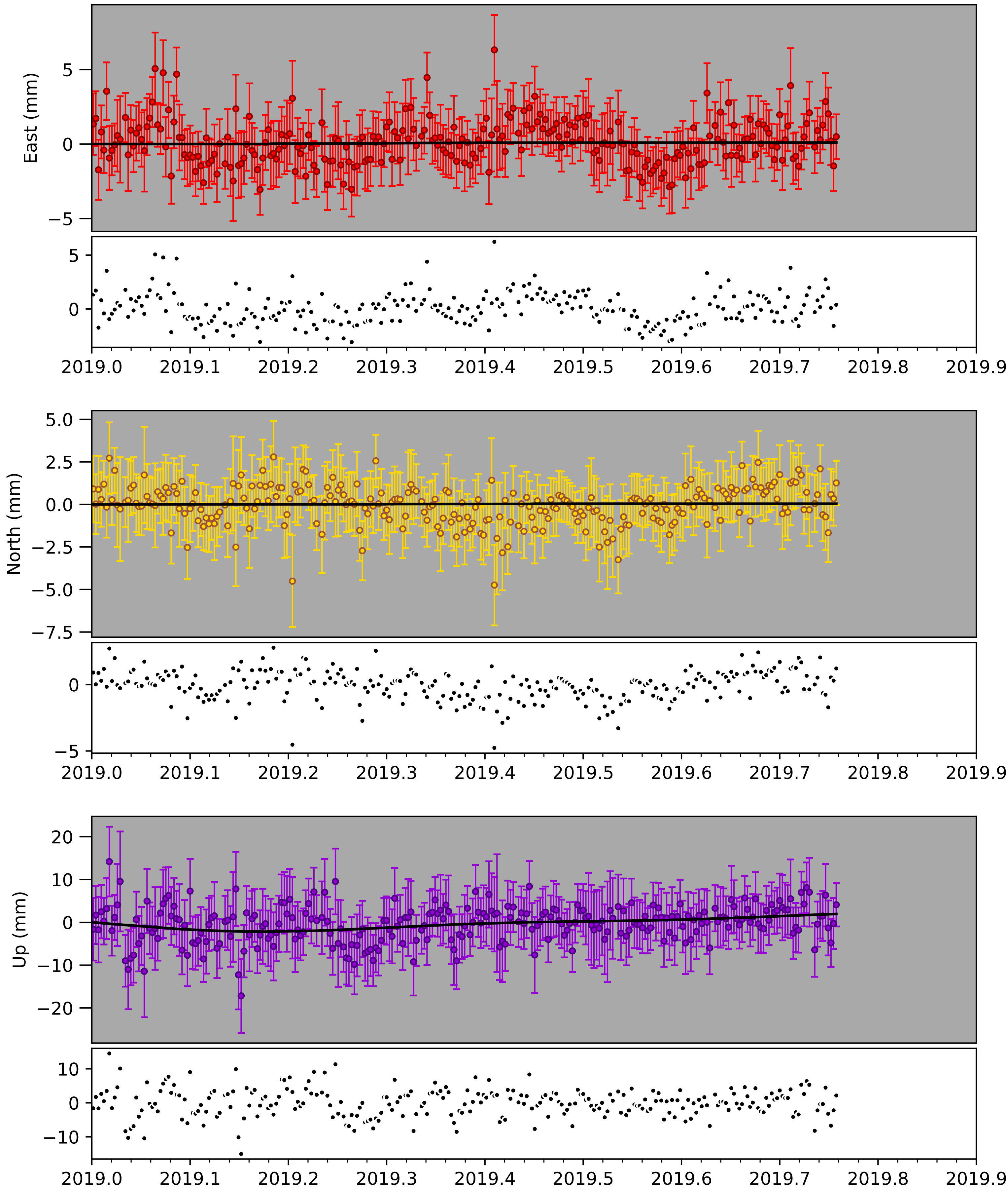

THAP

[175.7856] [-39.6825]

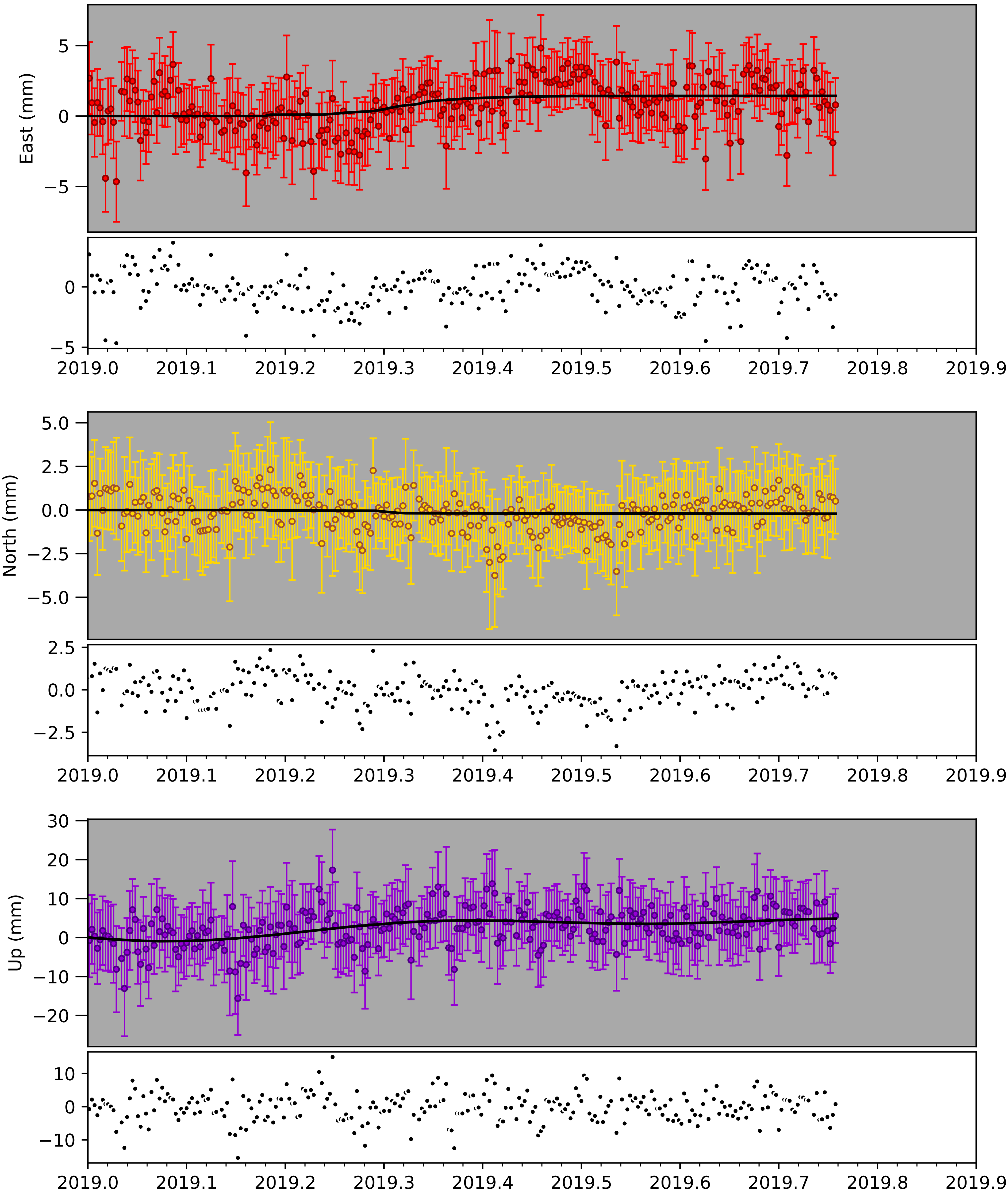

TKAR

[177.8114] [-38.4375]

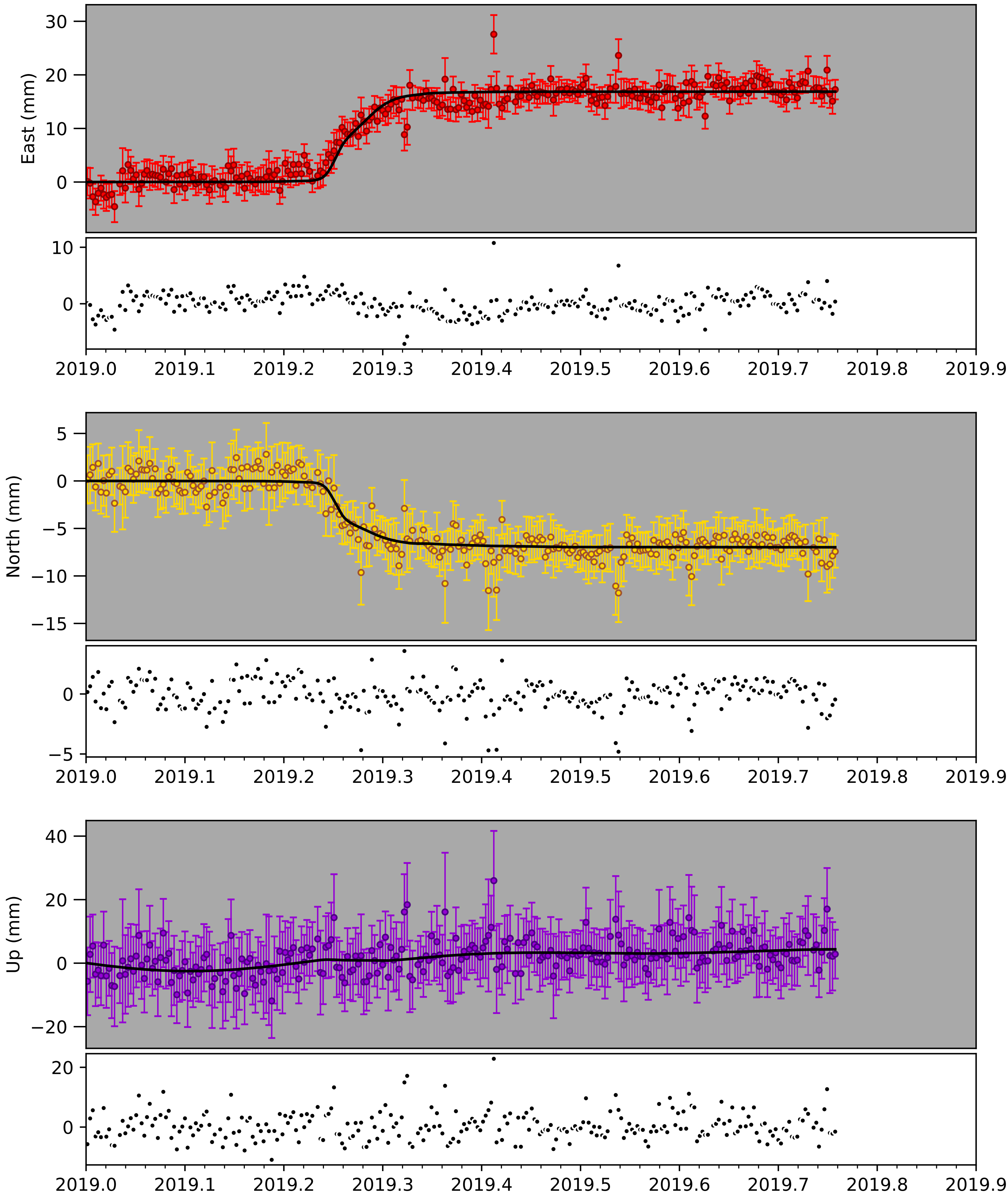

TURI

[176.3826] [-40.265]

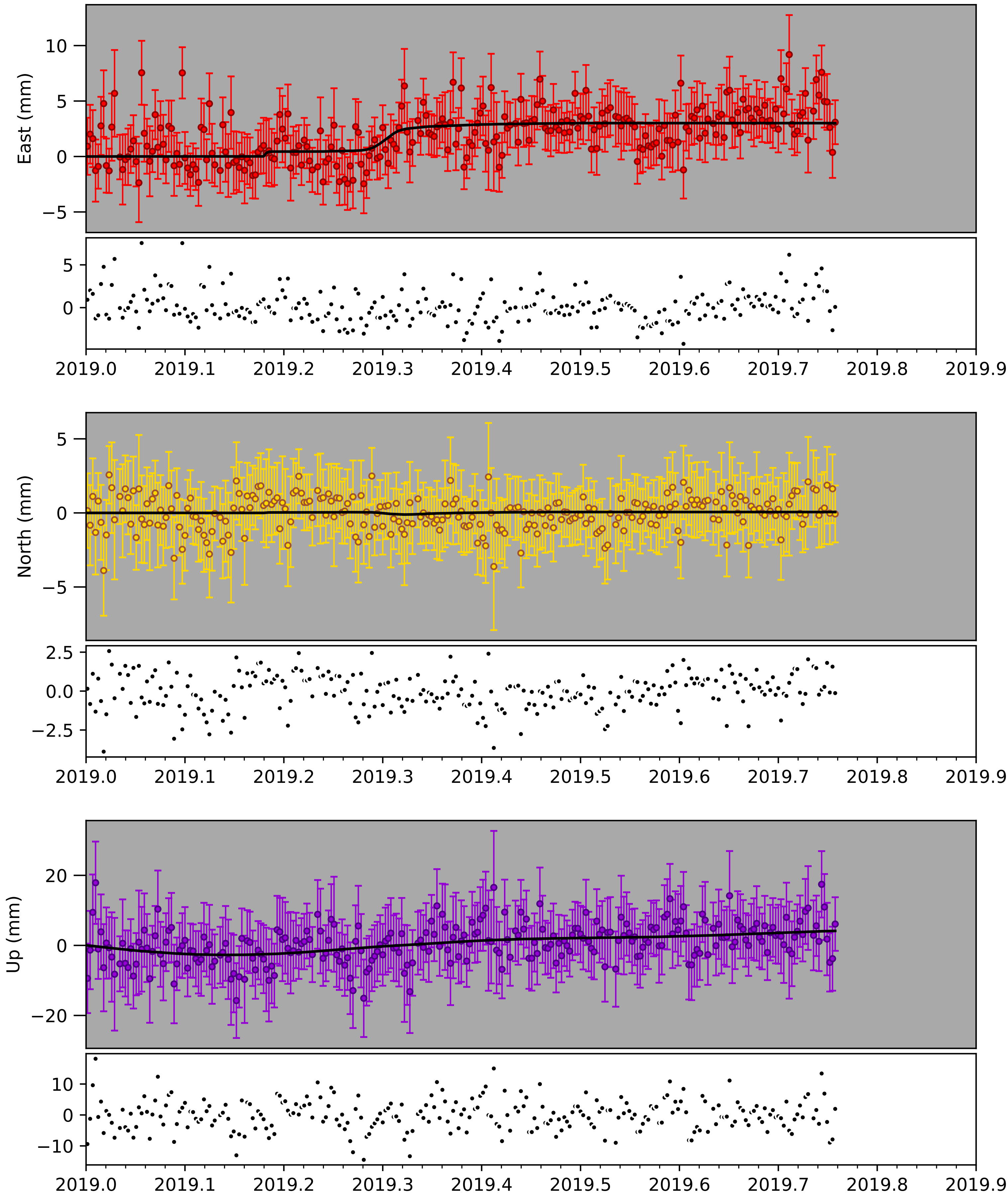

U008

[178.8961] [-38.859]

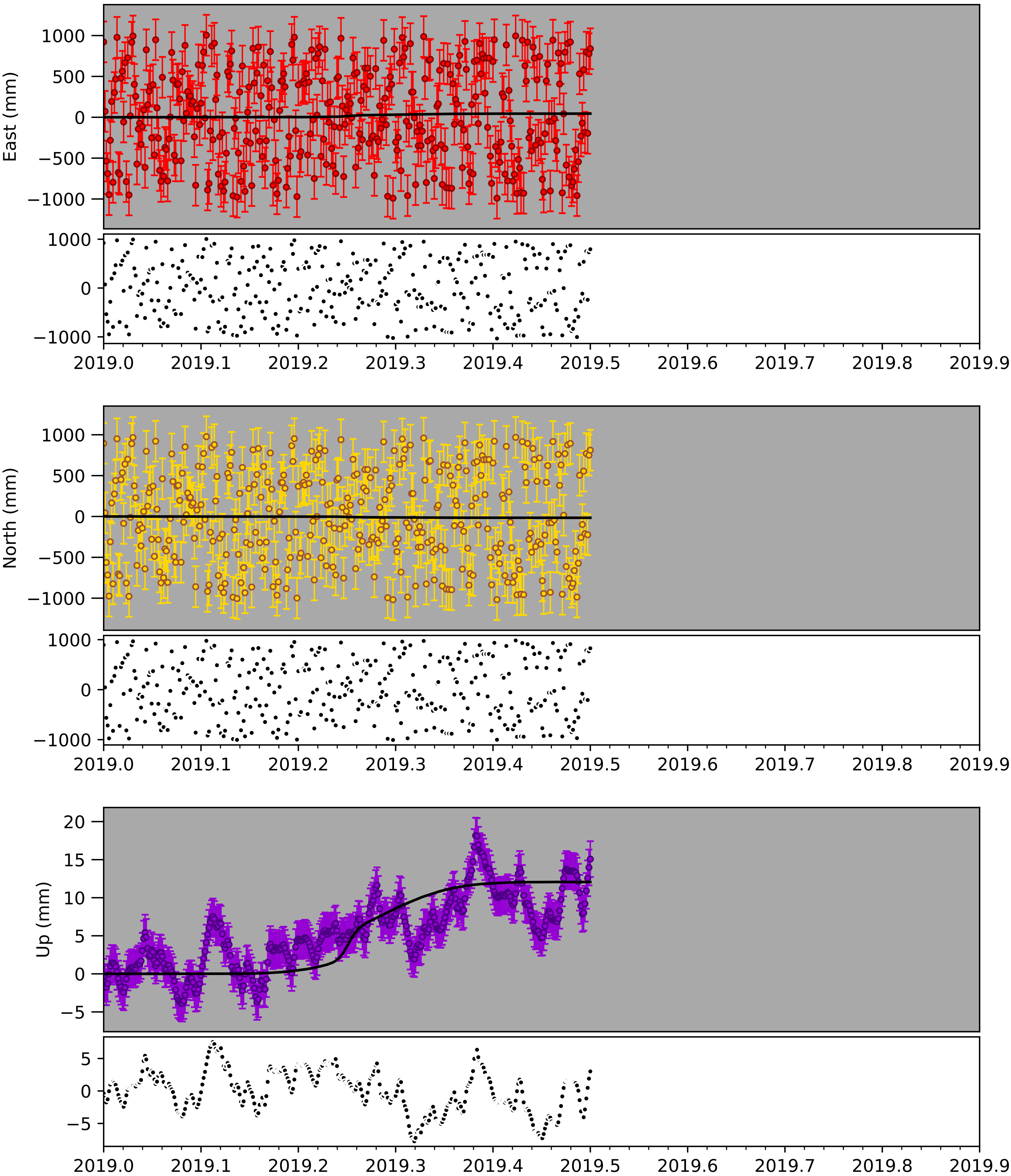

U009

[178.6145] [-38.7273]

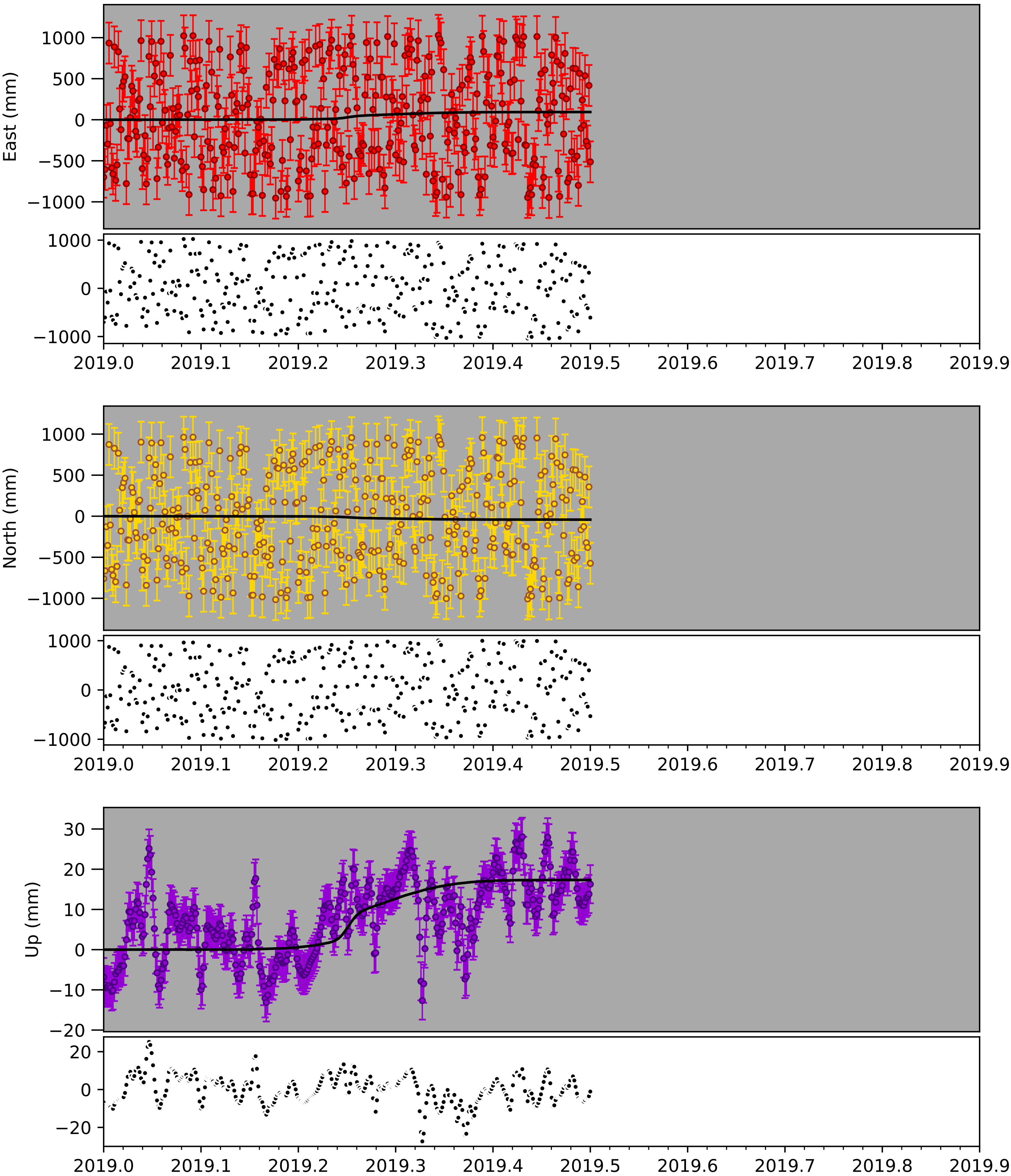

VGMO

[175.7543] [-39.4074]

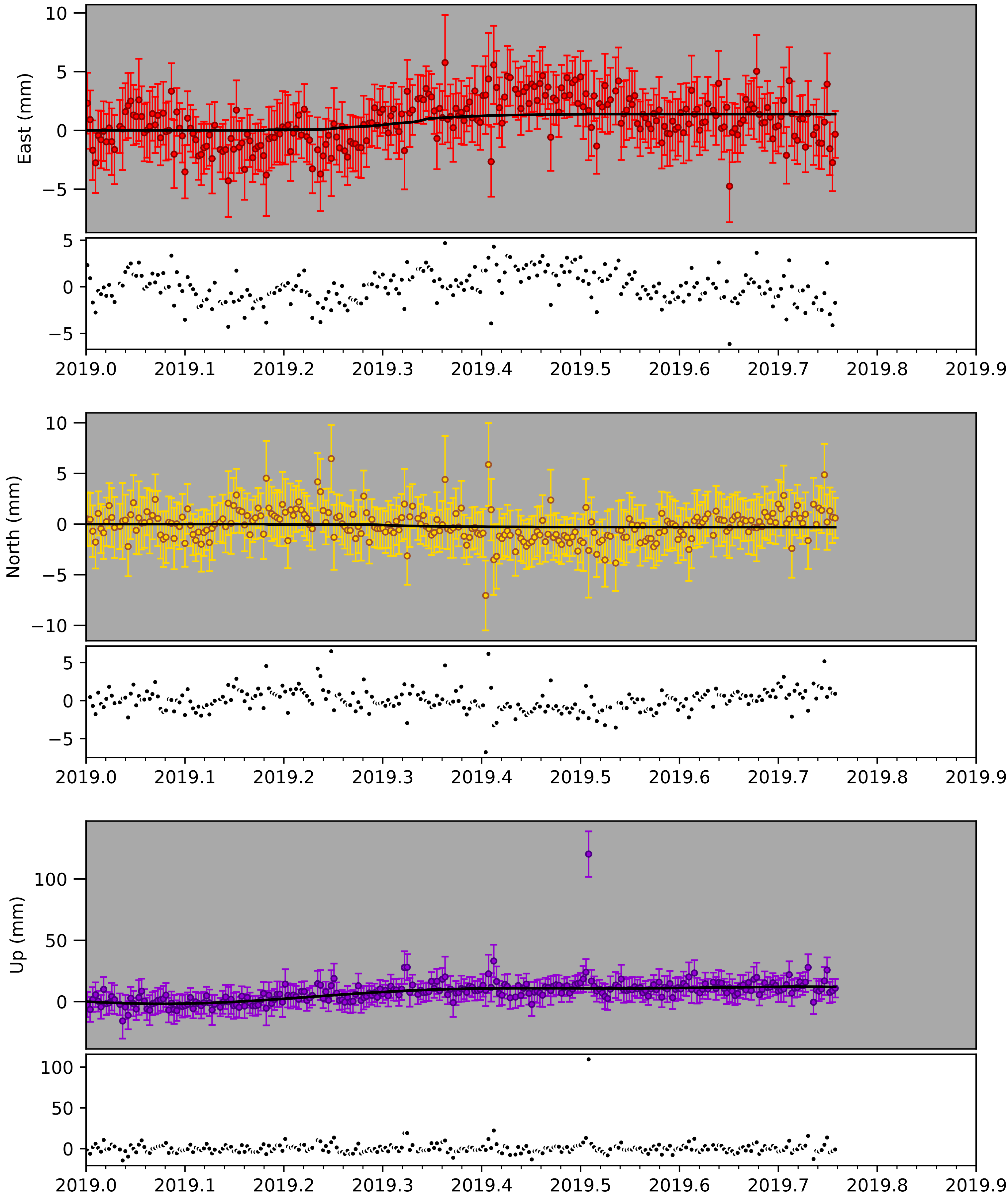

VGMT

[175.4705] [-39.3846]

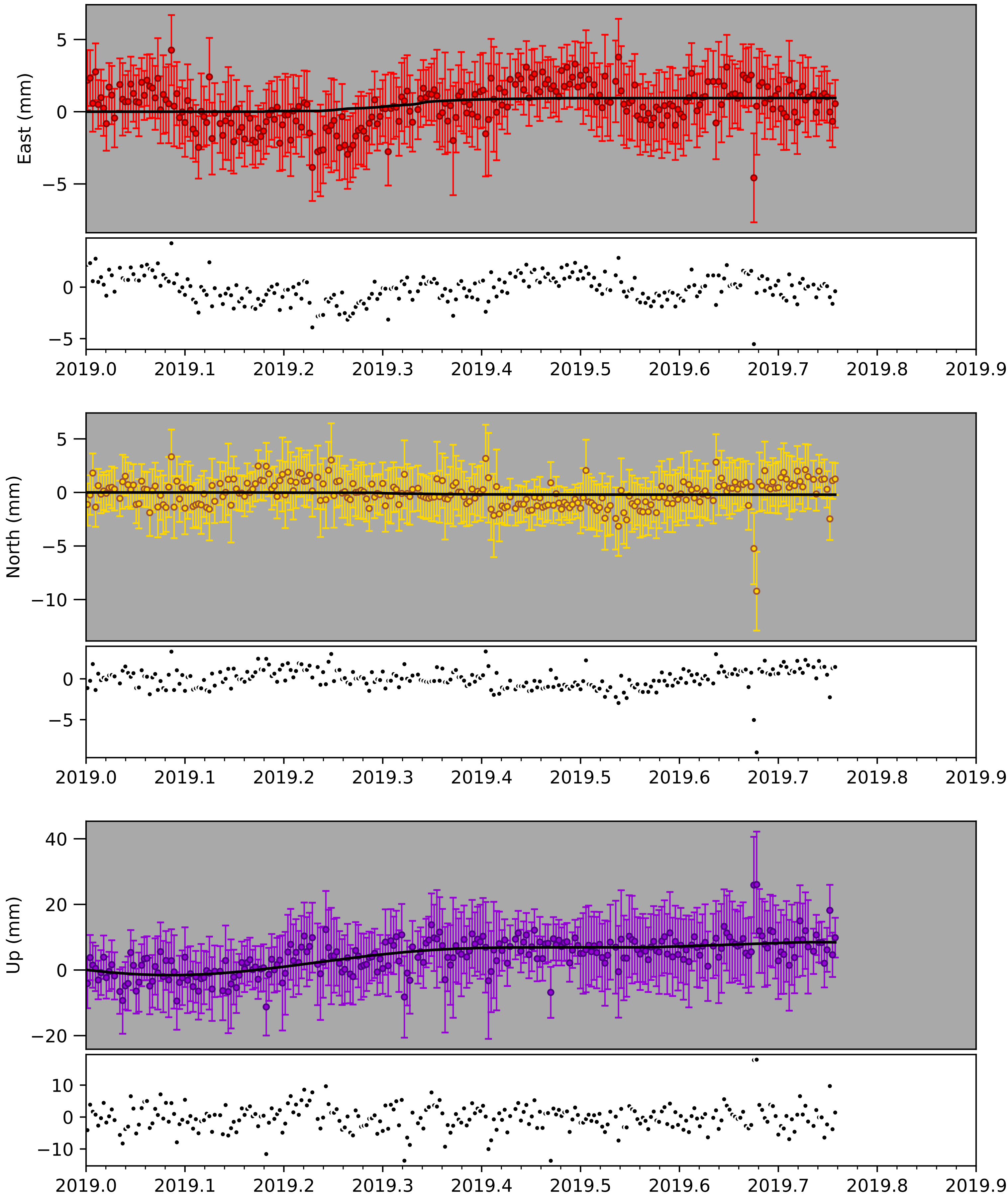

VGOB

[175.5422] [-39.1998]

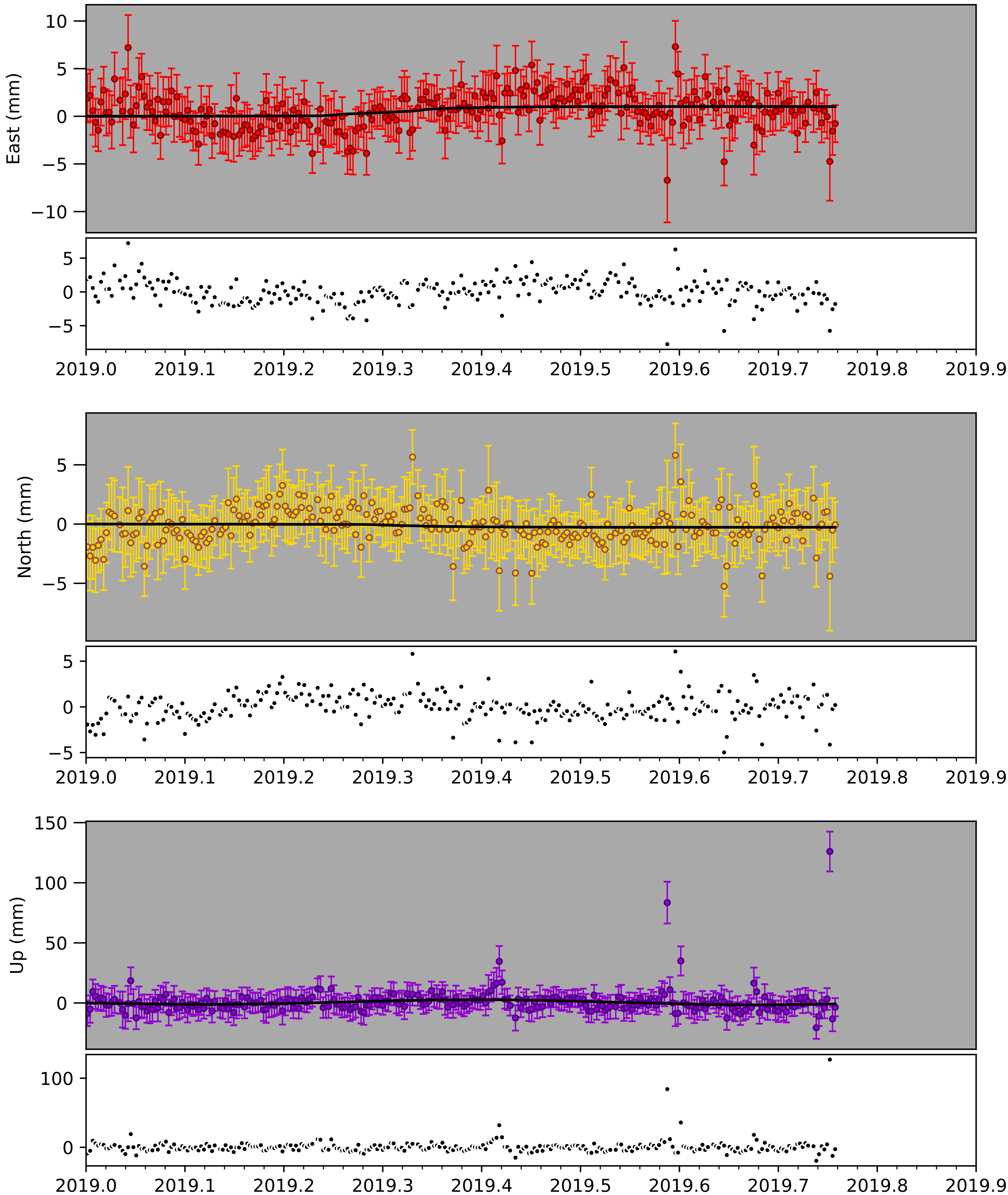

VGWN

[175.5979] [-39.3269]

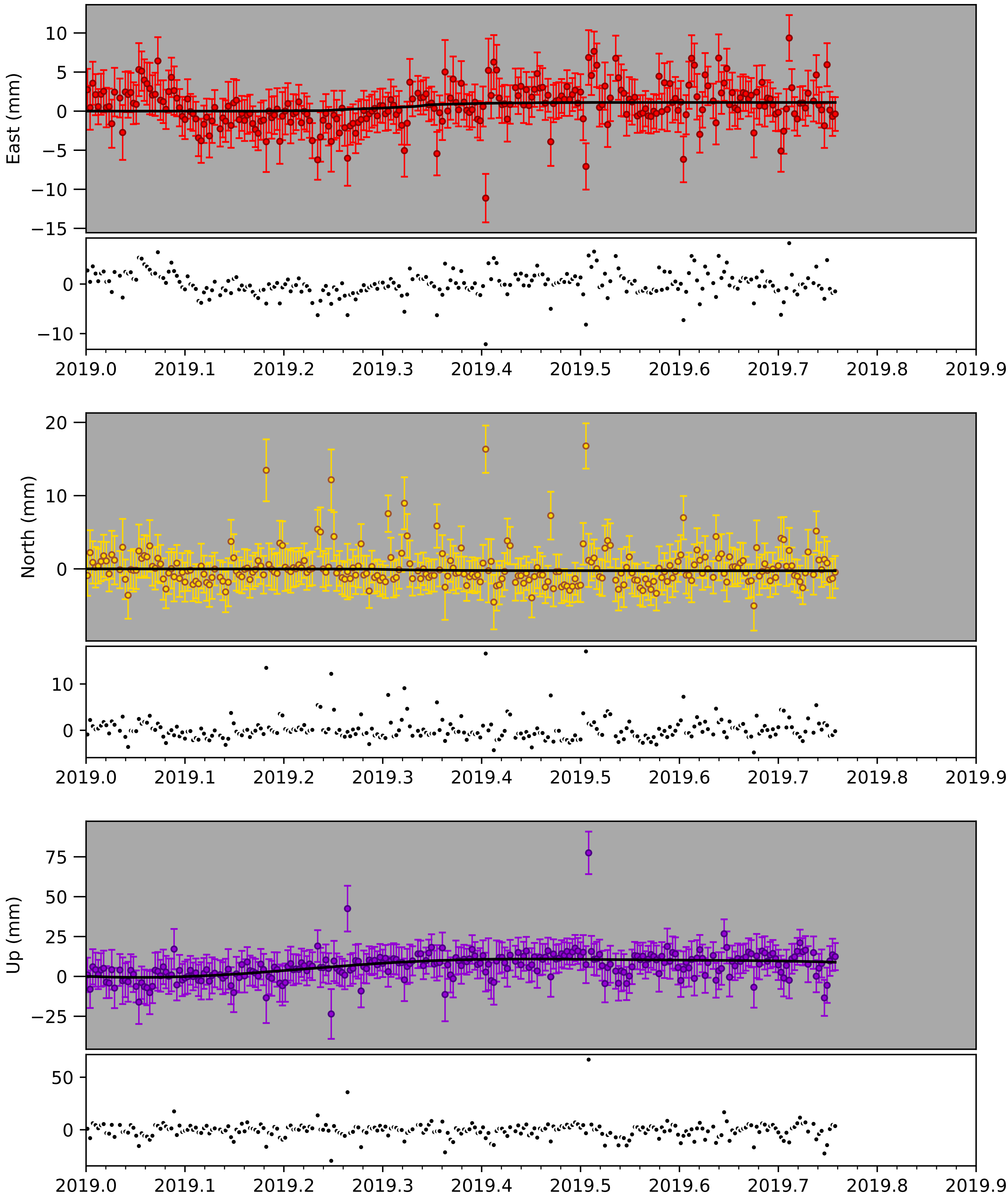

WAHU

[177.2344] [-39.0772]

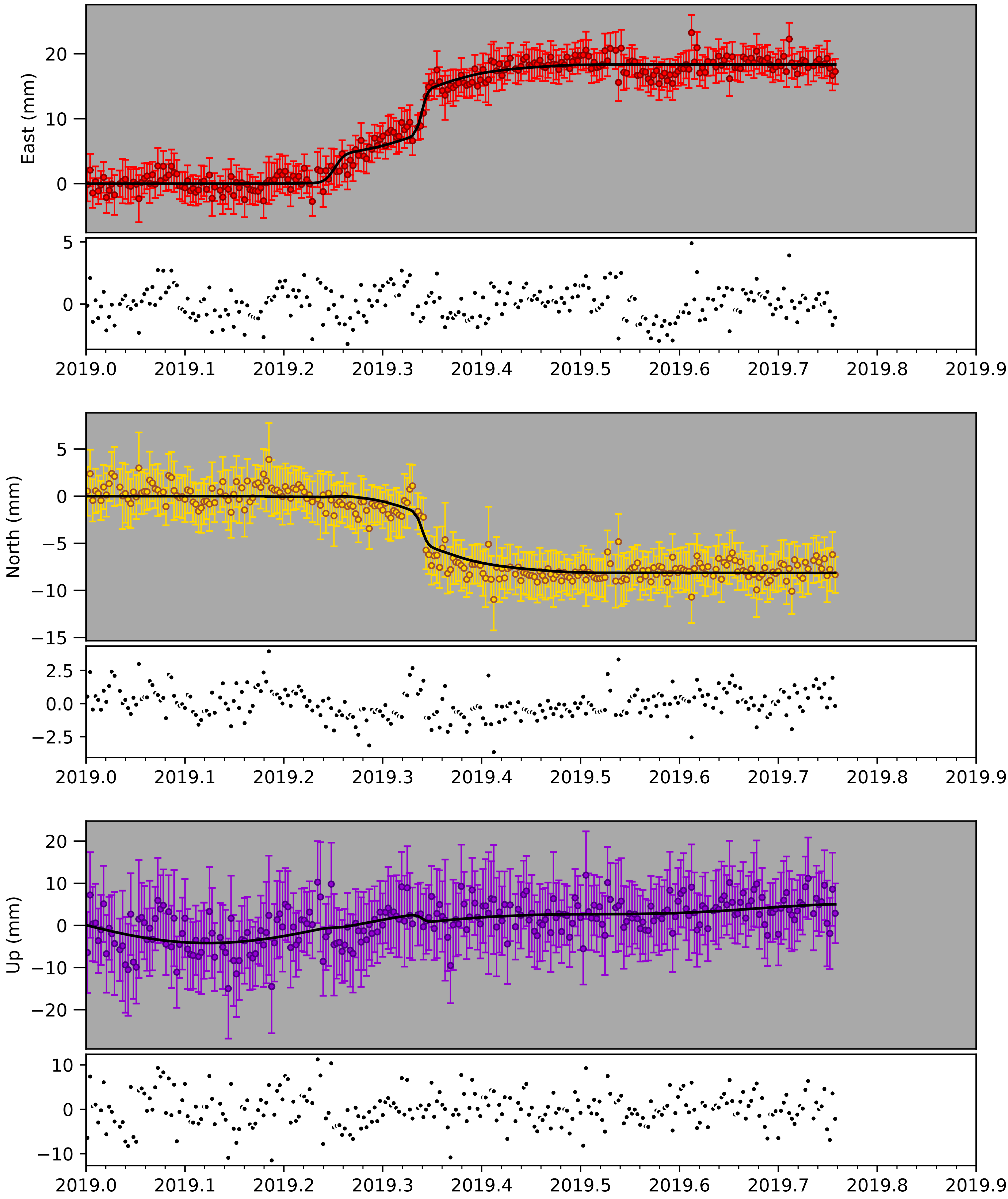

WHVR

[175.4517] [-39.7301]

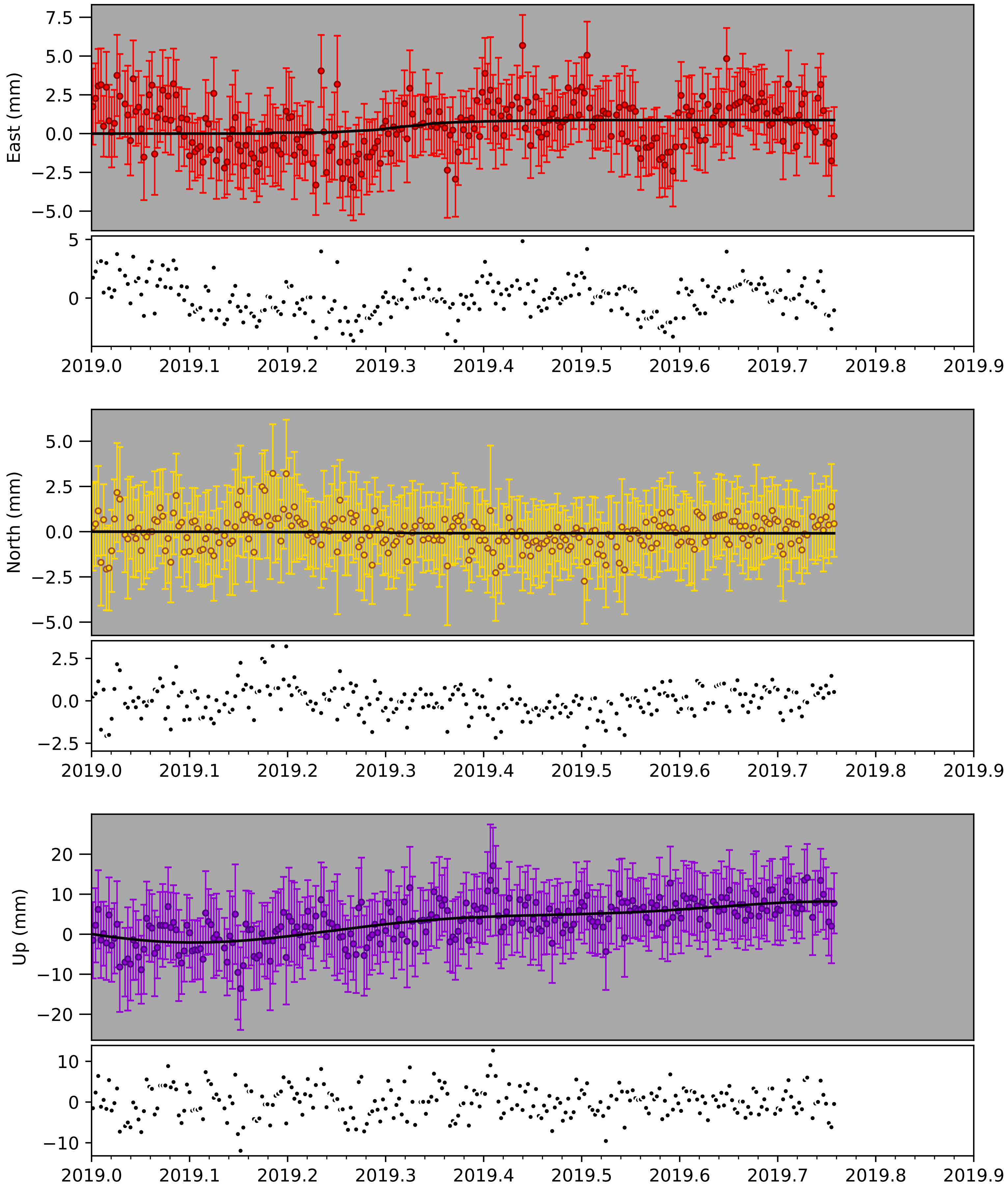

WMAT

[178.4087] [-37.825]

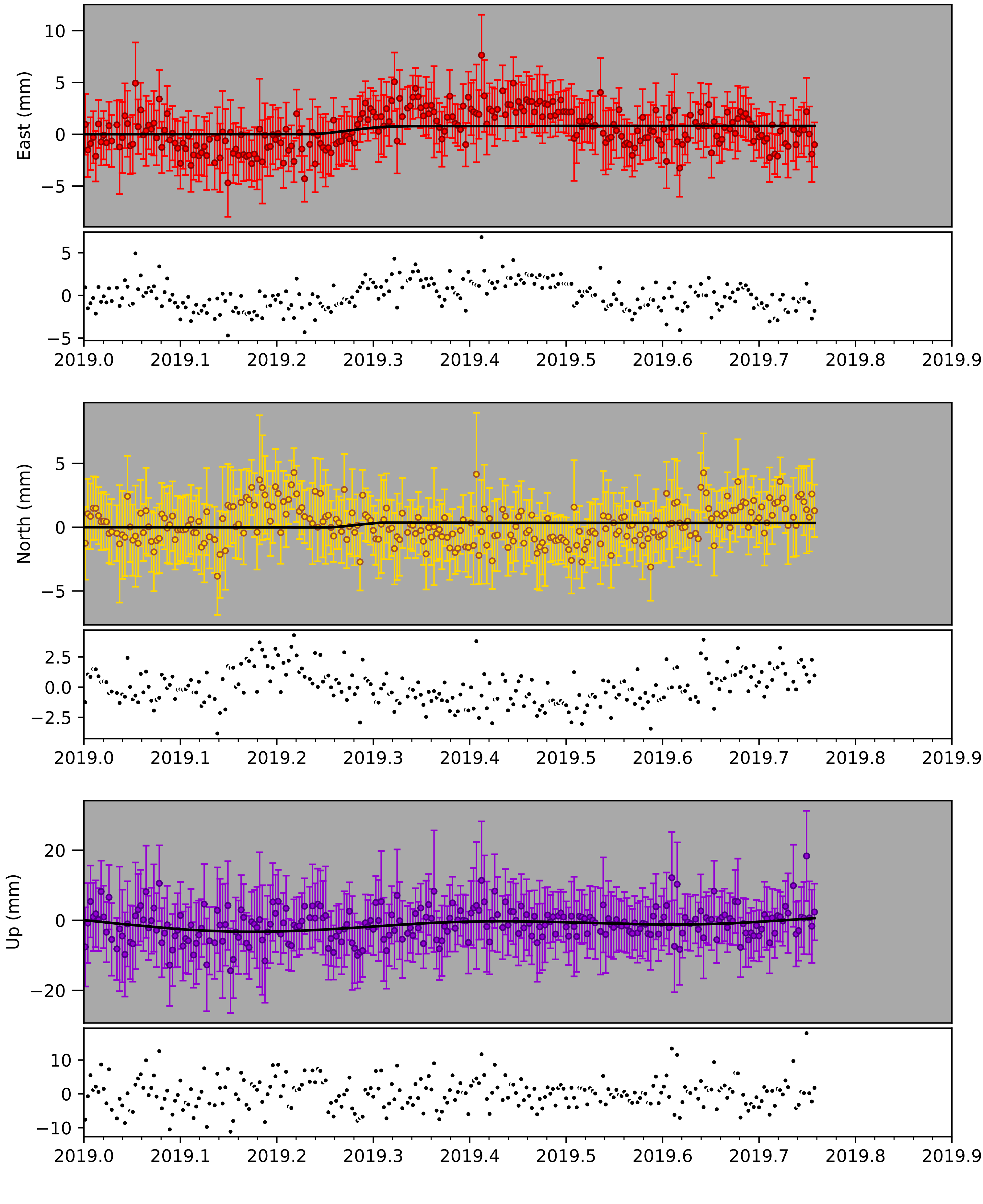

WPAW

[176.543]   [-39.8959]

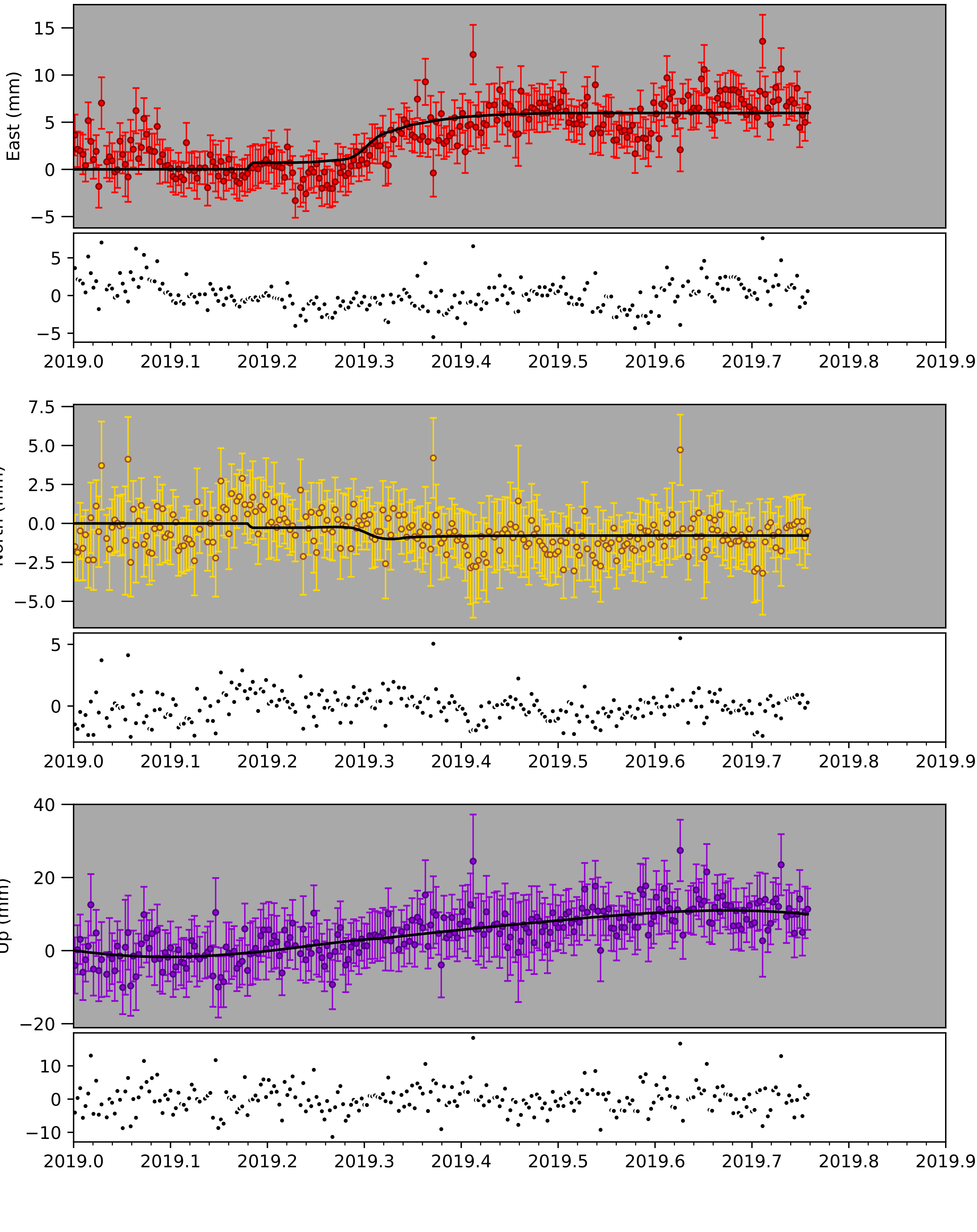

WPUK

[176.4406] [-40.0642]